Fusion and Solar Plasmas:

Synergistic Effects of Neutrons and Plasma on Materials in Fusion Reactors

&

Relaxation of Merging Magnetic Flux Ropes in Fusion and Solar Plasmas

A thesis submitted to The University of Manchester
for the degree of Doctor of Philosophy
in the Faculty of Science and Engineering

2017

Asad S. Hussain

School of Mechanical, Aerospace, and Civil Engineering

Contents

Abstract **15**

Decleration **16**

Copyright Statement **17**

Dedication **19**

Preface **20**

1 Introduction **23**

1.1 Review of Nuclear Fusion 26

1.1.1 Tokamak 28

1.1.1.1 Empirical scaling 30

1.1.1.2 First Wall, Limiters, Divertors 32

1.1.1.3 Reaction Thermodynamics 34

1.1.2 Coronal Heating and Avalanche Models 35

I Synergistic Effect of Neutrons and Plasma in Fusion Materials 38

2 Introduction and Literature Review 39

2.1 Basic Theory 49

2.1.1 Material Damage Theory 49

2.1.1.1 Point defects 50

2.1.1.2 Dislocations 52

2.1.1.3 Defect clustering 53

2.1.1.4 Thermodynamics 54

2.1.2 Sputtering 55

2.1.3 Plasma damage and ion transport 57

2.1.4 Neutronics 60

2.1.4.1 Neutron transport 60

2.1.4.2 Elastic and Inelastic Scattering 61

2.1.4.3 Cross-sections and Optical Model 62

2.1.5 Molecular Dynamics (MD) 67

2.1.5.1 Embedded Atom Model 68

2.1.5.2 Electronic Effects and Two-temperature Model (TTM) 69

3 Considering Surface Damage Due to High Energy Neutrons in Tungsten Using Monte Carlo Neutron Transport and Binary Collision Approximation 70

3.1 Introduction 70

3.2 Literature and Motivation 71

3.3 Methodology 73

3.4 Results and Discussions 75

3.5 Conclusion 80

4 Neutronics Analysis in a Spherical Shell 83

4.1 Introduction 83

4.2 Methodology 84

4.3 Results 86

4.4 Discussion 90

4.5 Conclusion 90

5 Statistical Description of Primary Events in Tungsten using Molecular Dynamics 92

5.1 Introduction 92

5.2 Methodology 94

5.2.1 Molecular Dynamic Setup 94

5.2.2 Statistical Analysis 96

5.3 Comparison of Potentials 98

5.3.1 Basic Defects 98

5.3.2 Displacements 99

5.4 Statistical Overview of Displacement Cascades 100

5.5 Conclusion 102

II Relaxation and Merger of Plasma Magnetic Flux Ropes 103

6 Introduction and Literature Review 104

6.1 Basic Plasma Theory 104

6.1.1 Kinetic description of plasma 104

6.1.2 Fluid description of plasma (MHD) 106

6.2 Magnetic Reconnection 110

6.2.1 Sweet Parker Reconnection and Current Sheet Parameters . . 111

6.2.2 Hyper-Resistivity 113

6.2.3 Constant Rate of Reconnection 113

6.2.4 Plasma Heating in Merging Plasmas: Experimental Results . . 114

6.3 Relaxation and Helicity Conservation 115

6.4 Hydrodynamic and Plasma Stability 117

7 A Relaxation Model of Coronal Heating in Multiple Interacting Flux Ropes **121**

7.1 Introduction 121

7.2 Theoretical approach and methodology 122

7.2.1 Initial field configuration 122

7.2.2 Energy 126

7.2.3 Axial flux 127

7.2.4 Helicity 127

7.2.5 Relaxed state 129

7.2.6 Relaxation calculation 130

7.2.7 Cases studied 134

7.2.8 Validation of field approximation 134

7.3 Results 135

7.3.1 Effect of the radius of final flux rope 135

7.3.2 Calculation of energy release and comparison with simulations 139

7.3.3 The dependence of energy release on initial fieldline twist . . . 142

7.4 Large multi-threaded flux ropes 144

7.5 Discussion & Conclusions 151

8 Magnetohydrodynamic Simulations of Twisted Magnetic Flux Ropes155

8.1 Introduction 155

8.2 Approach and Methodology 156

8.3 Maximum Separation 159

8.4 Twist in Stable Flux Rope 159

8.5 Reverse Twist 160

8.6 Relaxation Trigger 162

III Effect of Plasma Instabilities on Fusion Materials 169

9 Applying an Edge Localised Mode Relaxation Model for Damage in Fusion Relevant Tungsten 170

IV Concluding Statements 175

10 Summary of Work 176

11 Future Work 179

References 180

Appendix A: All Cascade Visualisations of Primary Neutron Events Using Molecular Dynamics 199

Word count - 28,202

List of Figures

1.1 Nuclear binding energy 27

1.2 Tokamak concept 29

1.3 Joint European Torus (JET) with plasma inset 29

1.4 JET layout 30

1.5 Scaling of plasma containment time using a power law (1.5) against experimental time (Yushmanov and Takizuka, 1990). 31

1.6 Diagram showing various plasma facing configurations 33

1.7 Energy spectrum of particles within a fusion environment (Matsuura and Nakao, 2009). 35

1.8 Plot of temperature as a function of depth of the solar atmosphere. . 36

2.1 Cross-section of (n,γ) reaction for W-184 (an isotope of Tungsten) . . 40

2.2 TEM image of fuzzy tungsten 45

2.3 Mechanism of Bremstrahlung radiation 47

2.4 Deuterium (D_2) and deuterium hydride (DH) desorption in pure tungsten following ion irradiation (Cu^{2+}) 48

2.5 Illustration of point defects. Self-interstials are a special case where the interstitial atom is the same as a overall material. 50

2.6 Burgers vector 52

2.7 Dislocations 53

2.8 Plot of tungsten sputter yield due to deuterium atoms as a function of the inciden ion impact energy 56

2.9 The various effects expected on materials within a fully functioning fusion reactor. 59

2.10 Depiction of neutron-nucleus scattering interaction. 62

2.11 Setup for measuring neutron cross section. 63

2.12 CERN nTOF facility 64

2.13 Cross-section of elastic collisions for tungsten-186. 65

3.1 Pre-processed data from SRIM for bulk tungsten damage 74

3.2 Setup for MCNP simulation. 75

3.3 Trajectory of neutrons within the slab geometry in Cartesian coordinates. 76

3.4 Damage prediction for full (non-surface simulation) 100 cm slab of tungsten 77

3.5 Surface (20 micron) damage illustration due to 14 MeV neutrons . . 77

3.6 Histogram of collisions occuring in the surface 78

3.7 Semi log cumulative tally of collision energy 79

3.8 Distribution of events within the slab geometry. 81

3.9 Distribution of neutron flux within the slab geometry as a function of depth. 82

4.1 Spherical shell setup for simulation of transport of 14 MeV neutrons 85

4.2 PKA profile for spherical shell, courtesy of M. Gilbert (CCFE) using a Spectra-PKA analysis. 86

4.3 Analysis per surface of PKAs 87

4.4 PKA flux spectrum for Spectra-PKA in a spherical shell simulation. 88

4.5 Comparison of PKAs at various surfaces of the spherical shell simulation. The row above are PKAs within tungsten, and the ones below within the steel-water moderator. 89

5.1 BCC lattice and subsequent consideration of symmetry for directions of primary knock ons. 93

5.2 Cascades generated as a result of molecular dynamics simulations of tungsten. 95

5.3 Depiction of how the basis for finding the statistical moments can affect the visualization of the cascade shape. Note how the cartesian vectors do not represent the system as well as the eigenvectors. . . . 97

5.4 Comparison of defects produced in simulations using the two EAM potentials. 99

6.1 Unit volume for plasma flow 106

6.2 Diagram of Magnetic Reconnection 112

7.1 Azimuthal field lines of flux ropes as initially setup (a) and then relaxing to form a single flux rope (b) in an $8 \times 4 \times 20$ simulation box. The final state depicted is specific to cases 2 and 4. 132

7.2 (a) Approximating polynomial and exact function for axial field $B_z(r)$, demonstrating the quality of fit, for $\lambda = 0.8$ (approximate, orange dashed, and exact, black), $\lambda = 1.4$ (approximate, pink dashed, and exact, blue), $\lambda = 1.8$ (approximate, dark blue dashed, and exact, green). Note that only three curves are visible since the exact and approximate curves are almost identical. (b) The difference between the exact and the approximation function for $\lambda = 1.8$. 136

7.3 Initial axial field B_z for two flux ropes, using the approximate polynomial, for case 4; the flux ropes centred at $(0, 0)$ and $(-2, 0)$. 137

7.4 Energy change for two flux ropes merging and relaxing against final rope radius, both with (green, $\lambda_1 = 1.4$ $\lambda_2 = 1.8$; orange, $\lambda_1 = \lambda_2 = 1.8$) and without (black, $\lambda_1 = 1.4$ $\lambda_2 = 1.8$; blue, $\lambda_1 = \lambda_2 = 1.8$) a simulation box. Positive values represent an increase in energy from the initial to final state. The vertical line represents conservation of volume. 138

7.5 Energy output for a single flux rope relaxing ($\lambda = 1.8$) against final rope radius (R_f) with (red) and without (black) a simulation box. . 140

7.6 Contours of energy change for two flux ropes merging and relaxing with various λ. The dotted line represents $\lambda_2 = \lambda_1$. 143

7.7 Energy output as a function of twist for two initially identical flux ropes $\lambda = \lambda_1 = \lambda_2$ 145

7.8 Variation of α vs. λ_2, where λ_1 is fixed at 1.8. 146

7.9 Simulation setup for 23 flux ropes merging. The Figure shows current density in the midplane $z = L/2$, taken from the early stage of the MHD simulations. The central rope is the unstable flux rope ($\lambda = 1.8$) while the rest are stable ($\lambda = 1.4$). Note that the central unstable flux rope shows signs of the initial kink instability, with a current sheet forming at the right-hand side of the loop. Originally published in Hood *et al.* (2016) 147

7.10 Energy release from merging of individual flux ropes showing the MHD simulation (red) and relaxation model (black). The arbitrary time step depicts the number of flux ropes that have been absorbed into the reconnection process. The MHD time has been normalised to scale to the Taylor model. This is needed since the Taylor model does not provide a time factor. 149

7.11 Variation of force-free parameter, α, for the avalanche model. 150

8.1 Energy (dimensionless) output from flux rope simulations. The lines show various simulations. In situations of two flux ropes, two λ(twist) parameters are given. In situations where the flux rope is reversed, a minus sign is used. Half distance and quarter distance refer to 0.5 units and 0.25 units of separation between the edge of the flux ropes (normalised to Alfven wavelength). but probably interesting 158

8.2 Simulation of two merging flux ropes: $\lambda_1 = 0.6$ and $\lambda_2 = 1.8$ 160

8.3 Simulations of two flux ropes with one single reversed rope (left). (a) depicts the initial setup, (b) depicts the merger that was observed, and (c) depicts the lack of merger after refining the mesh.The vectors show the tiwst of the flux ropes. 161

8.4 Relaxation alpha with number of flux ropes merged 162

8.5 Simulation of two merging flux ropes 0.25 units apart depicting a line out of current magnitude on the edge of the stable magnetic flux rope (marked with X). 164

8.6 Simulation of two merging flux ropes 0.5 units apart depicting a line out of current magnitude on the edge of the stable magnetic flux rope (marked with X). 165

8.7 $B_x$line out at $x = 0.3$ 167

8.8 Fourier transform of B_x at [0.3, 0, 0] across all time steps. 168

9.1 Plot of plasma pressure against position(Maggi *et al.*, 2014) 171

9.2 Molecular dynamics simulation setup for sputtering of continuous and damaged samples. 174

List of Tables

5.1 Fundamental defect energies for the two potentials and comparison to DFT calculations. 98

5.3 Tabulated statistics from simulations done for primary knock on cascades formed in tungsten using the D Mason potential. 101

7.1 Initial field conditions for the relaxation of two flux ropes. 134

7.2 Results of the Taylor model compared to the MHD model. 141

7.3 Results of the Taylor model compared to the MHD model for the 23 flux rope simulation. 148

Abstract

This thesis is submitted as requirement for the degree of Doctor of Philosophy. It comprises of essentially two parts.

The first deals with materials in a fusion reactor and examines how neutron damage affects material in a fusion reactor, with focus on how this is important for plasma damage. The methods used are neutron transport, primary event analysis and molecular dynamics. It found that the neutron damage by 14 MeV neutrons is restricted to back scatter events within the surface (first 20 microns). Molecular dynamics analysis showed that the issue of cascades is heavily dependent on direction of primary event and the energy of such. Statistical analysis was done to provide a standard approach for modelling of damage through neutrons.

The second deals with the relaxation of magnetic flux ropes with an emphasis on kink unstable flux ropes. A relaxation model was developed which shows good approximation to simulation results of merging magnetic flux ropes. Subsequently, work was done to establish the physical processes involved in relaxation. This was done by examining magnetohydrodynamic (MHD) simulations of two flux ropes, one unstable and one stable. It was found that there is is a clear distance at which merger does not occur any more. Furthermore, a critical current seems to be a requirement at the edge a stable flux rope.

Declaration

No portion of the work referred to in the thesis has been submitted in support of an application for another degree or qualification of this or any other university or other institute of learning.

Copyright Statement

http://documents.manchester.ac.uk/DocuInfo.aspx?DocID=2442 0), in any relevant Thesis restriction declarations deposited in the University Library, The University Library's regulations (see http://www.library.manchester.ac.uk/about/regulations/) and in The University's policy on Presentation of Theses

Dedication

To my parents and the rest of my family, who always believed in me,

To my friends, who were always there for me,

To my supervisors and academic advisors, for giving me the opportunity.

Preface

This is the preface, and as such, this is one section of this thesis that I am completely and totally owning. It will not contain any citations or any matter pertinent to the thesis. Therefore, before we move any further, I say to the examiner that this section does not have any technical information about my work; I would not be offended if you chose to skip it and move on to the introduction. Indeed you are probably the first to read this little essay.

I am not sure if it is correct to own a section in this manner, but I feel the need to be able say certain things. Perhaps to give an idea of what a journey it is doing a doctorate to the casual reader, to set the scene, or even just for purely cathartic reasons.

It hasn't been easy and yet I feel I could have done more. There were moments when I was lost and where I struggled to apply myself. My only wish with this thesis is that it in some way contributes to science. I love science, it has probably been my one true love. The ability it has to provide a narrative and then try to become the vessel of our understanding of the universe, of our place in the grand scheme of things. I feel we are no closer to a conclusive answer, but we're thinking in the right fashion to be able to objectively place what we observe. That is what science is and I admire that elegance.

As I said, it has not been easy. There have been ups and downs. There have been moments where I have been tempted to walk away from it all; whether it was due to the monumental feeling of the task at hand or my own feelings of intellectual inability. Somehow though, I still persisted and here it is, the final product. I could not have done this on my own. There are people who have helped me, and I can truly believe that they had no ulterior motives and have genuinely been there for me.

I start with my parents. My father has always believed in me and always pushed me to excel in whatever I set my heart to. It is his unwavering support that has allowed me to be able to be in a position to try whatever I choose to without fear of the repercussions of failure. That in itself is infinitely admirable and I wish that every person has someone like that. My mother has always demonstrated a caring I have never fully understood or felt that I deserved, but I am grateful for it and aspire to it. I have probably never been the best son, but I am proud and honoured to be their son, and I hope they know it. My brother and my sister have also demonstrated unprecedented support and they deserve a special mention too. I wish they live a happy life and do not make the mistakes I do.

My supervisors and academic advisors come next. On the top of the list are Prof. Paul Mummery and Prof. Philippa Browning. Both only saw when they first met was (hopefully) a keen child interested in learning more, and they did all they could to help me. They were there when I needed advice, guidance, and always encouraged me to be bold – they respected my input. And again I am very grateful. I am also grateful to Dr. Christopher Race for very useful guidance and conversations through my PhD. A special mention as well to Prof. Kieran Gibson for providing excellent supervision and guidance during the early phases of my PhD.

And then there are my friends. A fair number of whom I trusted and I will forever

be indebted to. Who probably do not know the value they have in my heart. I will not name them, that will be a long list and I'd be worried that I missed someone (because I may be ungrateful enough that I didn't truly value what people did for me). You know who you are, and you are just as much responsible for this because I do not know how I could have found the strength to be here if it wasn't for all of you.

Thank you and thank you again!

I now invite you to have a peek at what I have been doing for the past four years...

Chapter 1

Introduction

The following thesis is submitted as a requirement of the degree of Doctor of Philosophy (PhD) at the University of Manchester. It was done under the umbrella of the Fusion Centre for Doctoral Training (Fusion CDT) and was funded by Engineering and Physical Sciences Research Council (EPSRC grant code: EP/K504178/1). I (the author) would also like to recognise the service provided by the University of Manchester IT Services allowing the use of the CSF and RedQueen computing clusters and the N8 consortium for their services and allowing the use of the Polaris computing cluster.

The PhD itself commenced purely as the topic of the Synergistic Effects of Neutrons and Plasma on Materials in Fusion Reactors. However, part of the funding and CDT programme requirements dictated that a secondment into a fusion-relevant subject separate from the core topic had to be conducted for three months. It was then that work into relaxation of solar and Tokamak plasmas was commenced where the focus was to create an analysis using helicity conserved relaxation for merging magnetic flux ropes. The results yielded during this secondment were considered of benefit to academia, and I requested that I be allowed to pursue both topics over the remainder

of my PhD. All stakeholders within the project agreed and this thesis is the resulting product.

The thesis is written in the style where individual Chapters are written such that they could be adjusted and then published in an academic journal. It is divided into two core parts which deal with each of the individual topics. Parts III and IV wrap the thesis as a whole. The following is a summary of all the Chapters in this thesis.

Chapter 1 - Introduction

Part I *Synergistic Effect of Neutrons and Plasma in Fusion Materials*

Chapter 2 - Introduction and Literature Review: Review of relevant material theory, neutronics, molecular dynamics, and the fusion material problem.

Chapter 3 - Considering Surface Damage Due to High Energy Neutrons in Tungsten Using Monte Carlo Neutron Transport and Binary Collision Approximation - *Work in collaboration with Paul Mummery (Manchester), Christopher Race (Manchester), and Kieran Gibson (York)***:** Details of an investigation of 14 MeV neutrons in tungsten using simulation (MCNP and SRIM) within a slab based geometry. Personal contribution includes running the simulations, post-processing, and analysis of results.

Chapter 4 - Neutronics Analysis in a Spherical Shell - *Work in collaboration with Mark Gilbert (Culham Centre for Fusion Energy)***:** Details of an investigation of 14 MeV neutrons in tungsten surrounded by a moderator using simulation (MCNP) and subsequent analysis of primary events (SPECTRA-PKA) within a shell based geometry. Personal contribution includes adjustment

of spherical shell simulation to obtain relevant results (modification to include more surfaces for recording tallies and fluxes), passing fluxes through SPECTRA-PKA, subsequent analysis, and conclusions.

Chapter 5 - Statistical Description of Primary Events in Tungsten using Molecular Dynamics - *Work in collaboration with Christopher Race (Manchester) and Daniel Mason (Culham Centre for Fusion Energy)*: Molecular dynamics investigation (LAMMPS) of the statistical nature and behaviour of primary event cascades within tungsten. Personal contribution includes benchmarking, setting up, and running of simulations, and statistical analysis of results obtained.

Part II *Relaxation and Merger of Plasma Magnetic Flux Ropes*

Chapter 6 - Introduction and Literature Review: Introduction to plasma physics, plasma relaxation, and coronal heating.

Chapter 7 - A Relaxation Model of Coronal Heating in Multiple Interacting Flux Ropes - *Work in collaboration with Philippa Browning (Manchester) and Alan Hood (St. Andrews), published in Astronomy and Astrophysics in March 2017*: Detailing the development of an analytical model for the relaxation and merger of kink unstable and multiple flux ropes (the content has been modified slightly to fit into this thesis better). Personal contribution includes development and benchmarking of relaxation model from algebraic manipulation to computation.

Chapter 8 - Magnetohydrodynamic Simulations of Twisted Magnetic Flux Ropes - *Work in collaboration with Philippa Browning (Manchester) and Alan Hood (St. Andrews)*: Magnetohydrodynamic simulations (MHD) of multiple flux ropes to determine the specific conditions under which relaxation will

take place. Personal contribution includes modifiction of avalanche simulations to obtain results and post processing of these.

Part III ***Effect of Plasma Instabilities on Fusion Materials***

Chapter 9 - Applying an Edge Localised Mode Relaxation Model for Damage in Fusion Relevant Tungsten: A letter style Chapter laying the ground work for using relaxation to model Edge Localised Mode (ELMs) instabilities in Tokamaks and how these may result in enhanced material damage.

Part IV ***Concluding Statements***

Chapter 10 - Summary of Work

Chapter 11 - Future Work

1.1 Review of Nuclear Fusion

Fusion is a nuclear reaction that occurs by two nuclei merging to form another nucleus. As this occurs, the difference in binding energy results in a mass defect. This in turn, through Einstein's principle, results in a release of energy. This elementary process is described in textbooks such as Feynman *et al.* (1963).

When one looks at (Figure 1.1) how nuclear binding energy varies depending on the number of nucleons in a nucleus. On this graph, it is noted towards the left hand side of the curve; if two nuclei were to merge the overall energy would be in excess of the required binding energy and mass energy. This is the process that fusion energy relies on.

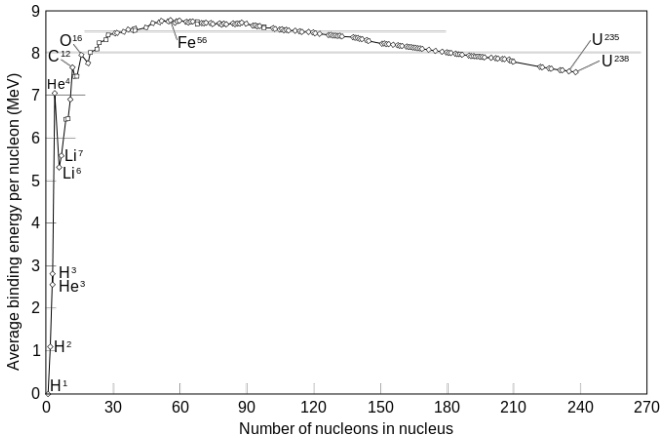

Figure 1.1: Nuclear binding energy
Source: Wikimedia Commons

Fusion energy is in fact the energy that powers the sun. Other fusion reactions of interest in the race towards achieving fusion energy currently use deuterium and tritium (isotopes of hydrogen) since this is considered the most efficient due to its high energy output and the high temperature of reaction (due to the Carnot cycle efficiency (Cengel and Boles, 2013). Significant fusion reactions are listed below:

$$ {}_1^1H + {}_1^1H \overset{0.42MeV}{\rightarrow} {}_1^2H + \beta^+ + v_e, \tag{1.1} $$

$$ {}_1^2H + {}_1^2H \overset{3.27MeV}{\rightarrow} {}_2^3He, \tag{1.2} $$

$$ {}_1^2H + {}_1^2H \overset{4.03MeV}{\rightarrow} {}_1^3H + {}_1^1H, \tag{1.3} $$

$$ {}_1^2H + {}_1^3H \overset{17.59MeV}{\rightarrow} {}_2^4He + n. \tag{1.4} $$

The hydrogen-hydrogen (Equation 1.1) reaction does not yield enough energy for an

earth based power plant to be viable. Of current primary interest towards commercial fusion is the deuterium-tritium (DT - Equation 1.4) reaction. From this point forth, we shall limit our attention to mostly this reaction.

Within a fusion reaction, the requirement is that the two nuclei be bought close enough to be capable of fusing (Kikuchi, 2010, 2011). With a nucleus being comprised of neutrons and protons, one needs to overcome the Columb barrier in order to be able to cause the reaction to occur. The particles are thus required to be heated in order to provide them with the necessary energy. This requires an unusually high energy ($0.48MeV = O(10^9)K$). However, by manipulating a process referred to as quantum tunnelling, we can achieve this reaction in $O(10^7)K$ which is still remarkably high! At this energy level, the D-T atoms ionise. This creates what is referred to as a plasma and in principle can be contained within magnetic fields.

Over the course of this thesis, two regions in which nuclear fusion takes place will be examined. Specifically, these are the tokamak and the solar corona.

1.1.1 Tokamak

The Tokamak is a cylindrical helical device that uses electro-magnets in order to contain plasma (Wesson, 1987). The Tokamak was invented in the Soviet Union in the late 1950s. At a time when work to contain plasma was underway, the Tokamak concept was found to have done so with remarkable results. The Tokamak can be visualised as a giant doughnut (formally a toroid). Two magnetic fields are formed: the poloidal and toroidal fields by virtue of outer coils and helical windings respectively. These are illustrated through Figures 1.2, 1.3 and 1.4.

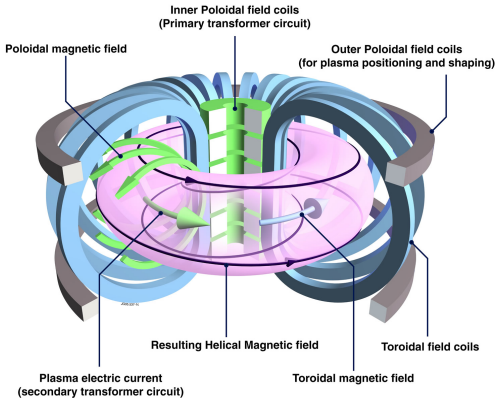

Figure 1.2: Tokamak concept
Source: EFDA

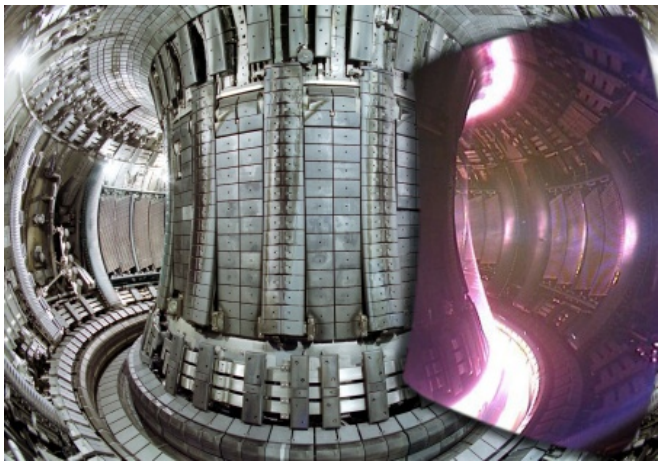

Figure 1.3: Joint European Torus (JET) with plasma inset
Source: EFDA/CCFE

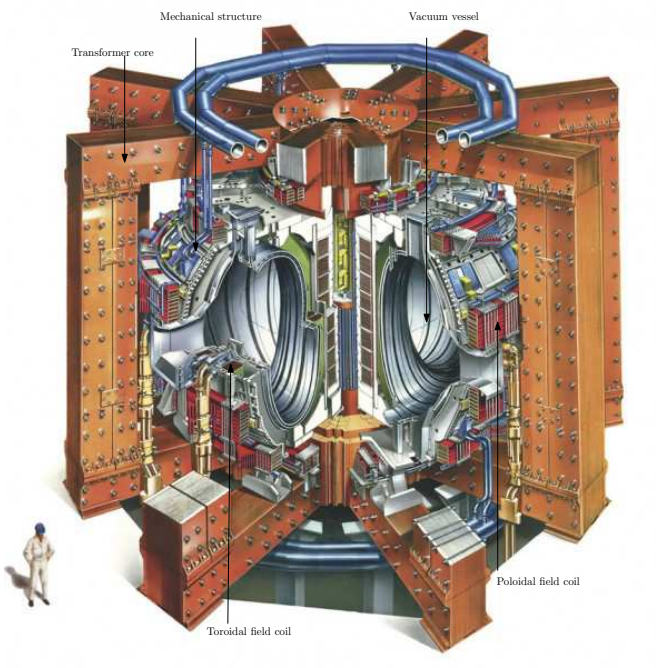

Figure 1.4: JET layout
Source: EFDA/CCFE

1.1.1.1 Empirical scaling

The initial Tokamak was found to be able to contain plasma for approximately 100 ms (Wesson, 1987). This was short due to the plasma cooling down far too quickly as a result of electron collisions, impurities and outward drifts. These problems are mitigated by increasing the size of the Tokamak as a result of reducing electron density, increasing the region in which the plasma can be contained, and reduce the chance for impurities to enter the core plasma. This led to the development of empirical scaling.

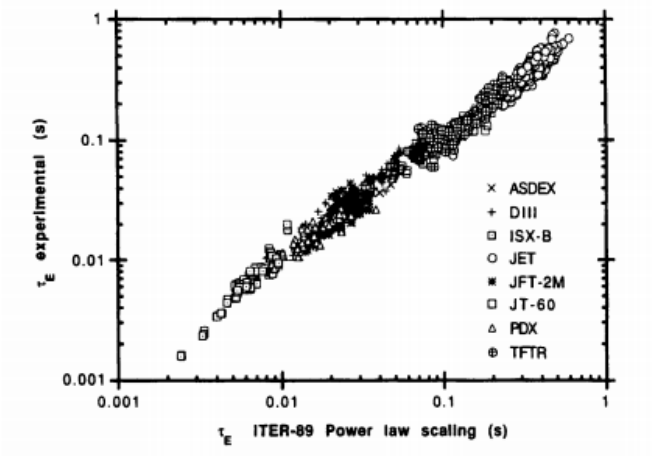

Figure 1.5: Scaling of plasma containment time using a power law (1.5) against experimental time (Yushmanov and Takizuka, 1990).

Figure 1.5 shows a plot of experimental confinement time for various Tokamaks against empirical scaled time based on the ITER-89 power scaling (Yushmanov and Takizuka, 1990) which states:

$$\tau = 48.10^3 . I^{0.85} B^{0.2} n^{-0.1} P^{-0.5} R^{1.5} \kappa^{0.5} \epsilon^{0.3} M^{0.5}, \tag{1.5}$$

Where I is the plasma current (MA), B is the toroidal magnetic field strength (T), n is the average density (10^{19} m^{-3}), P is the absorbed power (MW), R is the major radius of the Tokamak, κ is the elongation of the contained plasma, ϵ is the inverse aspect ratio (major to minor radius) of the Tokamak, and M is the hydrogen isotope mass.

As one can see, there is a high correlation to the major radius. On this basis, the current fusion road map is moving towards developing ITER and DEMO which are large radius devices.

1.1.1.2 First Wall, Limiters, Divertors

Particles tend to drift outwards from within the Tokamak vacuum vessel. Therefore one can see that eventually, the entire wall will be covered with plasma. To avoid this the Tokamak uses the concepts of limiters and divertors which arise from the principle that solid surfaces are sinks for plasma (plasma recombines into neutral ions) (Stangeby, 2000). The limiter cuts through a close fluxed surface and becomes a solid surface within it. A divertor on the other hand uses a current carrying conductor that bends the magnetic field and forms open field lines on the divertor surface. A cross section view of the various configurations is illustrated in Figure 1.6.

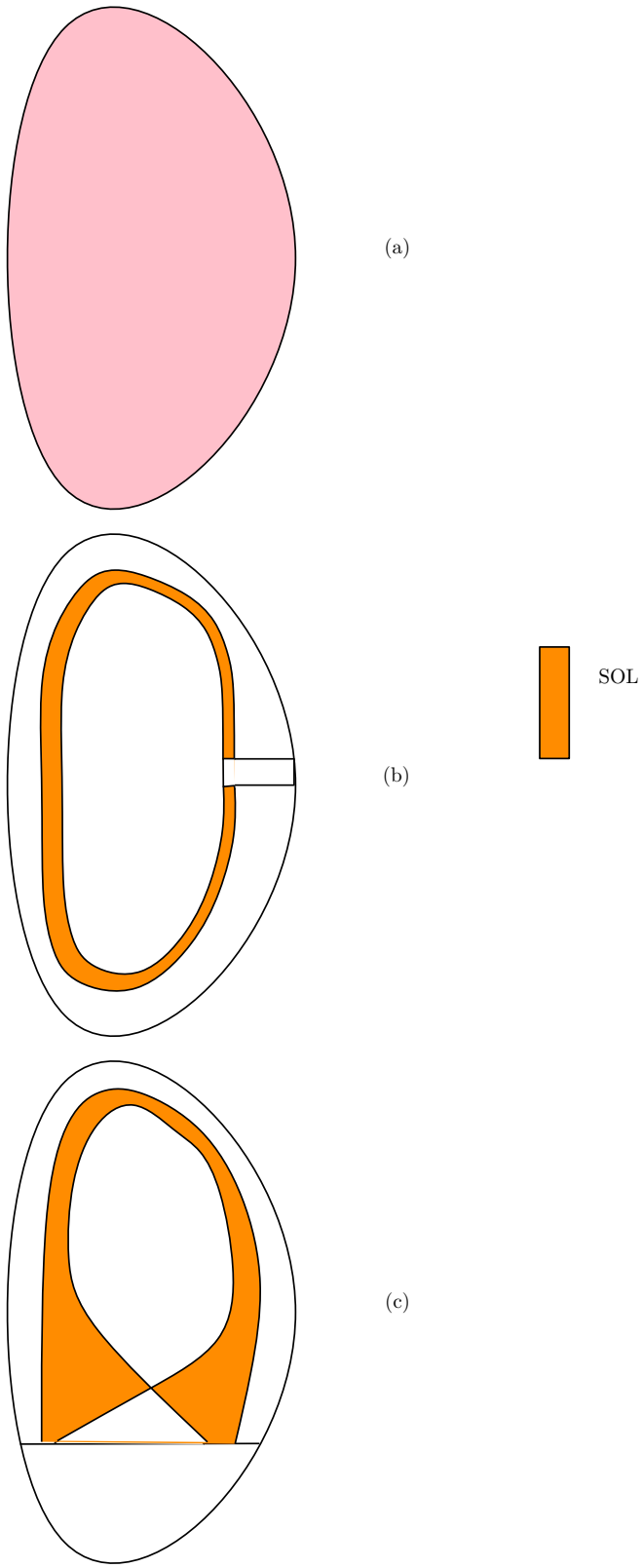

Figure 1.6: Diagram showing various plasma facing configurations
(a) No divertor/limiter (b) Limiter configuration (c) Divertor configuration
SOL is the Scrape Off Layer

Without a divertor or limiter, the heat load is uniform and thus difficult to extract from a power plant. Furthermore, a divertor or limiter configuration will allow for selective treatment of plasma facing components. Due to their versatility, divertors look likely to be the dominant concept (Maisonnier *et al.*, 2005).

The material is expected to primarily be that of tungsten. Tungsten is chosen due to its high melting point and low sputtering yeild Maisonnier *et al.* (2005); Cottrell *et al.* (2006) and will be the candidate material for any fusion reactor (Aymar, 2001). As such, most of this thesis will focus on tungsten. Tungsten, however, has the additional issue of brittleness when it is cool. It is hoped that this will be an issue that is mitigated in a steady state reactor, which will have a higher operating temperature.

1.1.1.3 Reaction Thermodynamics

The particle energy is released kinetically through the reaction particles. It is noted that the DT reaction normally emits a 14 MeV neutron and 3.5 MeV alpha particle. Since the reaction kinetics dictates that the energy must be distributed between these two particles, the spectrum normally is not very spread. This can be seen in light of work done (Matsuura and Nakao, 2009) which saw the variation of the spectrum while using a neutral beam to produce a DT plasma (Figure 1.7).

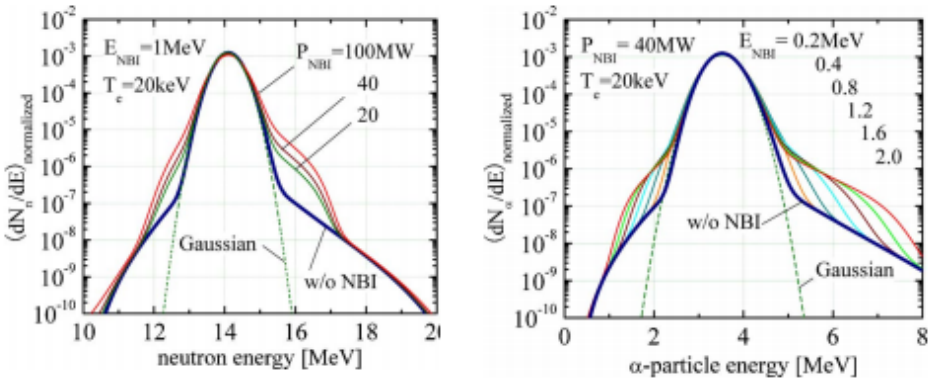

Figure 1.7: Energy spectrum of particles within a fusion environment (Matsuura and Nakao, 2009).

1.1.2 Coronal Heating and Avalanche Models

The coronal heating problem was realised during the analysis of emission released by the corona (Parnell *et al.*, 2012). It was found that the outer atmosphere (the corona) of the sun was emitting as a result of heavier ions which implied that it must be at a higher temperature than the photosphere. Measurements suggest that the corona measures at nearly a million Kelvin whereas the chromosphere is only of the order 1000 K (Klimchuk, 2015).

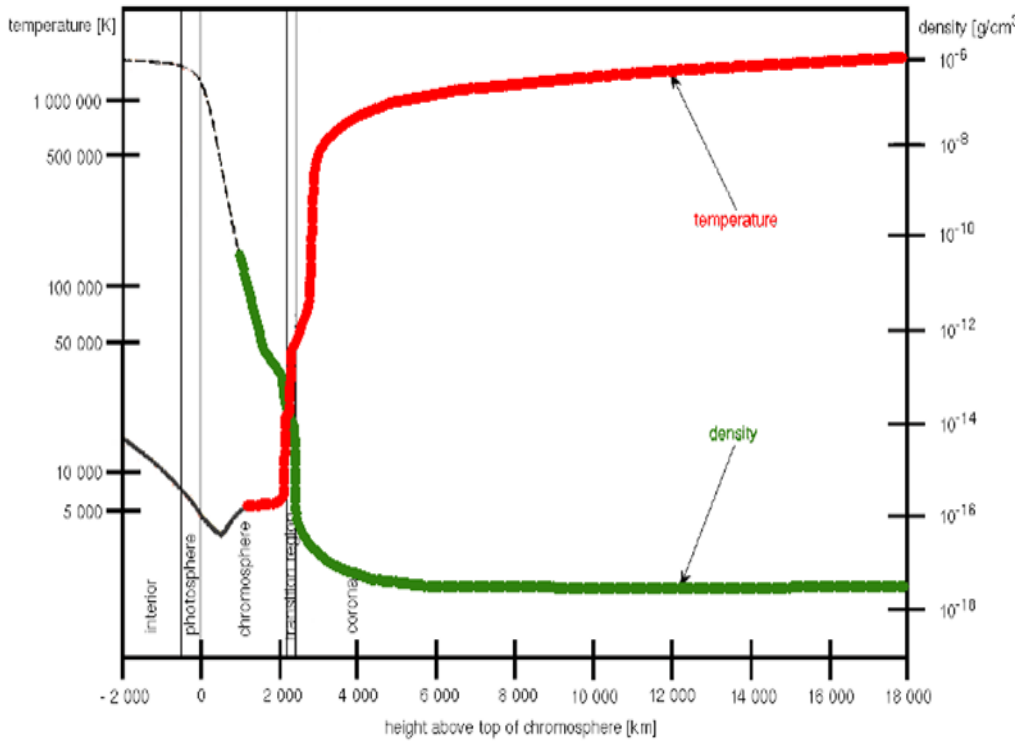

Figure 1.8: Plot of temperature as a function of depth of the solar atmosphere. Source: NASA

Classical heat transfer mechanisms do not explain the disparity as shown in Figure 1.8. As a result, work has subsequently been done to suggest mechanisms by which this could occur. Reviews (Parnell *et al.*, 2012; Asgari-Targhi *et al.*, 2013; De Moortel *et al.*, 2015) suggest there are two fundamental mechanisms by which this may happen. The first is the DC (direct current) mechanism which suggests that heating is a direct result of reconnection. The second is AC (alternating current) which is done through resonant Alfven wave transfer. The DC mechanism has the advantage that it readily explains self organisation of the coronal loops on the surface of the sun. However, there has been no clear proof of either method. This is primarily due to the fact that computational power is insufficient to simulate a significant portion of the solar surface.

Magnetic reconnection (DC) has been specifically investigated in the work of Long-

cope and Tarr (2015). A non-potential field is known to contain free magnetic energy. Examples of non-potential fields includes twisted and braided flux ropes. A flux rope is defined as a cylinderical self contained region of plasma. The geometry of these can be specific when theoretically required (such as cylinderical). Through this thesis, references to flux ropes will be cylinderical regions that can be treated in isolation. These fields can arise as a result of footpoint motion in the chromosphere. As a standard model, twisted ropes can result in the ideal kink instability and there is evidence of kink instability in the solar corona (Liu *et al.*, 2007; Liu and Liu, 2009; Srivastava and Dwivedi, 2010; Wang *et al.*, 2015). However, it is quite unlikely that a large number of flux ropes will be twisted at the same time. Therefore, the idea of an avalanche model was proposed (Lu and Hamilton, 1991; Charbonneau *et al.*, 2001) and shown in simulations. Merger of multiple ropes had already been suggested as a possible mechanism for coronal heating (Gold and Hoyle, 1960; Melrose, 1997; Kondrashov *et al.*, 1999).

Part I

Synergistic Effect of Neutrons and Plasma in Fusion Materials

Chapter 2

Introduction and Literature Review

A good understanding of the problem can be gained by looking at the paper (Wirth *et al.*, 2011). The problem presented with materials that will eventually be used in a fusion is that they will have to face extreme conditions that we do not have a lot of experience with. Furthermore, these conditions are not isolated. To simply break down the various phenomenon occurring:

- The deuterium-tritium plasma and subsequently fusion reaction is going to create:
  - 14.1 MeV average neutrons
  - 3.5 MeV alpha particles
  - Ion irradiation from the plasma on to the material surface
  - High heat loads on the material surface (for DEMO, this is expected to be 20 MW per sq. meter)
  - Formation of a potential (Debye sheath) on the edge of the surface

The problem is that these problems are not isolated. For instance, the interaction between plasma and material causes sputtering (ejection of atoms from the material surface) which in turn affects the plasma; the plasma is going to impose a heat load on the surface, the conduction of which will vary with neutron and ion damage; the material properties of the reactor will change with the reactor operation. There are a multitude of effects occurring at various time scales and length scales. Furthermore, as far as our current physical understanding goes of these effects, they are likely to affect one another. Through this literature review, it shall be noted that these do possibly affect one another.

Currently, the candidate material we have for a demonstration reactor is tungsten and therefore all work concerning plasma facing components and surface neutronics is done with this material in mind. To that effect, work done on investigation of transmutation in a fusion environment (Cottrell *et al.*, 2006) finds that due to the nature of the neutronics within a fusion reactor a large amount of transmutation is expected to occur. This is primarily due to a resonances of high capture cross sections for tungsten absorption. Figure 2.1 shows how the cross-section varies with incident neutron energy.

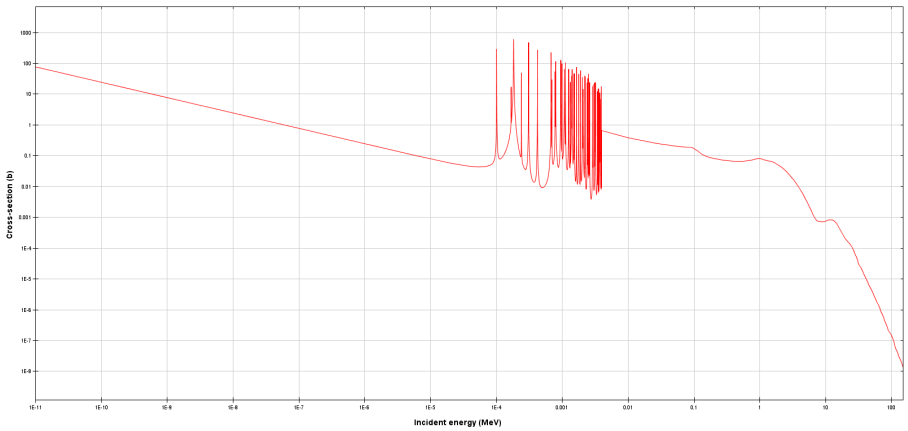

Figure 2.1: Cross-section of (n,γ) reaction for W-184 (an isotope of Tungsten)

The work is done primarily through FISPACT (an inventory code that calculates

the nuclides left in a geometry based on neutron flux data presented in Sublet *et al.* (2017)) analysis following a neutron analysis which understands the distribution of neutron energetics through the reactor. It is to here noted that even though the reaction in question (deuterium and tritium) produces 14.1 MeV neutrons, through collisions through the reactor will actually cause a distribution of neutrons of various energies. Neutron transport allows us to come up with a steady state distribution of this. The work found that significant amounts of rhenium and osmium would be present as a result of tungsten irradiation. To be specific: the plasma facing side is expected to be 95.3 atomic % tungsten, 3.0 atomic % rhenium and 1.7 atomic % osmium after 5 years of service in a conceptual fusion power plant (Maisonnier *et al.*, 2005).

The neutronics itself are currently only solvable through theory or simulation (with the latter being the dominant approach). This is due to the fact that currently there are no facilities that can generate 14 MeV neutrons. However, with years of fission experience and the problem of neutron moderation and damage being key concerns, there are well developed methods for modelling these. Sources (Gilbert *et al.*, 2012, 2013) have been working with these to come up with a reliable methodology for understanding the damage that can be expected in a steady state fusion reactor. The primary work here is on developing neutron fluxes within a DEMO reactor, how this is likely to develop as damage and the effects this causes such as transmutation damage and helium embrittlement.

Their work involved profiling the fluxes and then using these to prepare a model for the damage. This they did by constructing a full model based on the DEMO conceptual design (Maisonnier *et al.*, 2005) and then running it through the neutron transport code MCNP (Monte Carlo n-particle). Subsequently the fluxes were used with data tabulated using the NJOY nuclear data processor coupled with the

European EFF-1 library for neutron data to generate damage cross-sections. This yielded a damage profile for metals as a function of depth. However, this data is vastly sensitive to the library used as can be seen from the subsequent work done by Gilbert *et al.* (2013).

In a presentation the problem of the conditions for plasma facing components within ITER is discussed (De Temmerman, 2000). This is further emphasised in a paper by Roth *et al.* (2009). The key issues commented on were the conditions the plasma facing surfaces would be subject to, the factors impacting the lifetime of these, dust generation and tritium inventory.

Work done suggests that within ITER an expected flux of the order 10^{23} particles per second of deuterium and tritium can be expected during operation at the first wall with the order increasing to 10^{24} at the divertor surface. ITER is expected to operated at the 500 MW power output mark (Aymar, 2001).

Based on this understanding limiting factors for the plasma facing components primarily is that of erosion. Based on calculation using the B2-EIRENE (Schneider *et al.*, 2006) coupled code for fluid edge analysis and Monte Carlo neutral transport; an expected 48 grams of beryllium and 26 grams of tungsten at the divertor is expected to be eroded per shot which corresponds to 0.12 and 0.05 nanometers per second (8 and 0.12 during peak loads) respectively at the first wall. Within the divertor, the tungsten could be expected to erode 48 grams per shot (2 nm/s). Tungsten erosion is primarily expected to occur due to sputtering due to impurity atoms such as argon. These are expected to be introduced into the plasma as the allow for easier transition from L-mode of confinement to H-mode (Maggi *et al.*, 2014). The difference between L-mode and H-mode is the gas pressure at the edge of the Tokamaks, which is higher in the latter. This is done by introducing impurities (nuclides acting as catalysts to the fusion reaction) within the Tokamak chamber.

Due to the brittleness of tungsten and beryllium (which is expected to be enhanced due to neutron activity) it is expected that there will dust formation (Fortuna-Zaleśna *et al.*, 2017). This dust is going to be a major radioactive source and may also contain trapped tritium. For the purposes of analysis it is normally assumed that all erosion leads to dust formation as a conservative estimation.

Another concern is that of tritium retention. Tritium is a controlled substance. It is therefore expected that the amount that can be stored on site will be limited. Furthermore, any tritium that is retained within the structures is also likely to count towards this inventory with calculations being conservative. Work has been done to determine the extent of this (Barabash *et al.*, 2003; Kwast *et al.*, 1996). This work involved placing material samples within fast fission reactors to provide damage using neutrons greater than 1 MeV. When beryllium was irradiated up to an expected damage of 40 dpa, it was found that the tritium retention was increased by a factor of 10. Tritium is retained due to the formation of vacancies and of grain boundaries forming traps for transmuted tritium. Within tungsten, it was noted that the neutron energies were not high enough to cause activation within the material.

Another paper on plasma edge material interaction issues based on ITER (Federici *et al.*, 2003) talks primarily about the issue of Edge Localised Modes (ELMs). Type I ELMs are capable of discharging about 30% of core energy (ITER is expected to operate at 500 MW [Aymar, 2001] while DEMO could operate at 5 GW fusion power (Maisonnier *et al.*, 2005)). It is expected that ITER will operate within the ELMy H-mode criterion and therefore materials will need to be capable of handling these intense loads which could go up to 2 MJ/m^2. It is expected that during the ELM events, materials such as tungsten will melt and erode. Tungsten is expected to melt and then eventually be eroded at the divertor target. Conservative estimates suggest that extreme conditions possible within ITER can limit the divertor performance

with the criteria for divertor replacement (withstand 3000 normal DT plasma shots) unlikely to be attained. If however ELMs can be limited to within 1-1.5 MJ/m^2 this may not be an issue. It should be noted however that ELM criteria are currently in their infancy with a large portion of the physics still to be investigated. Measures for what the energy dissipated are currently based on empirical evidence.

Another condition of plasma damage that is currently being investigated as a likely problem within fusion environments is that of fuzz formation. The mechanism for this is described as helium atoms clustering and forming voids. This is shown in Figure 2.2 and is described in literature (Kajita *et al.*, 2009; Doerner *et al.*, 2011). The exact physics of the process is currently uncertain. Temperature variation seems to show an increase in fuzz formation (on the basis of the fuzz layer thickness) and so does an increase in flux but this reaches an equilibrium when coupled with erosion mechanisms through sputtering and erosion.

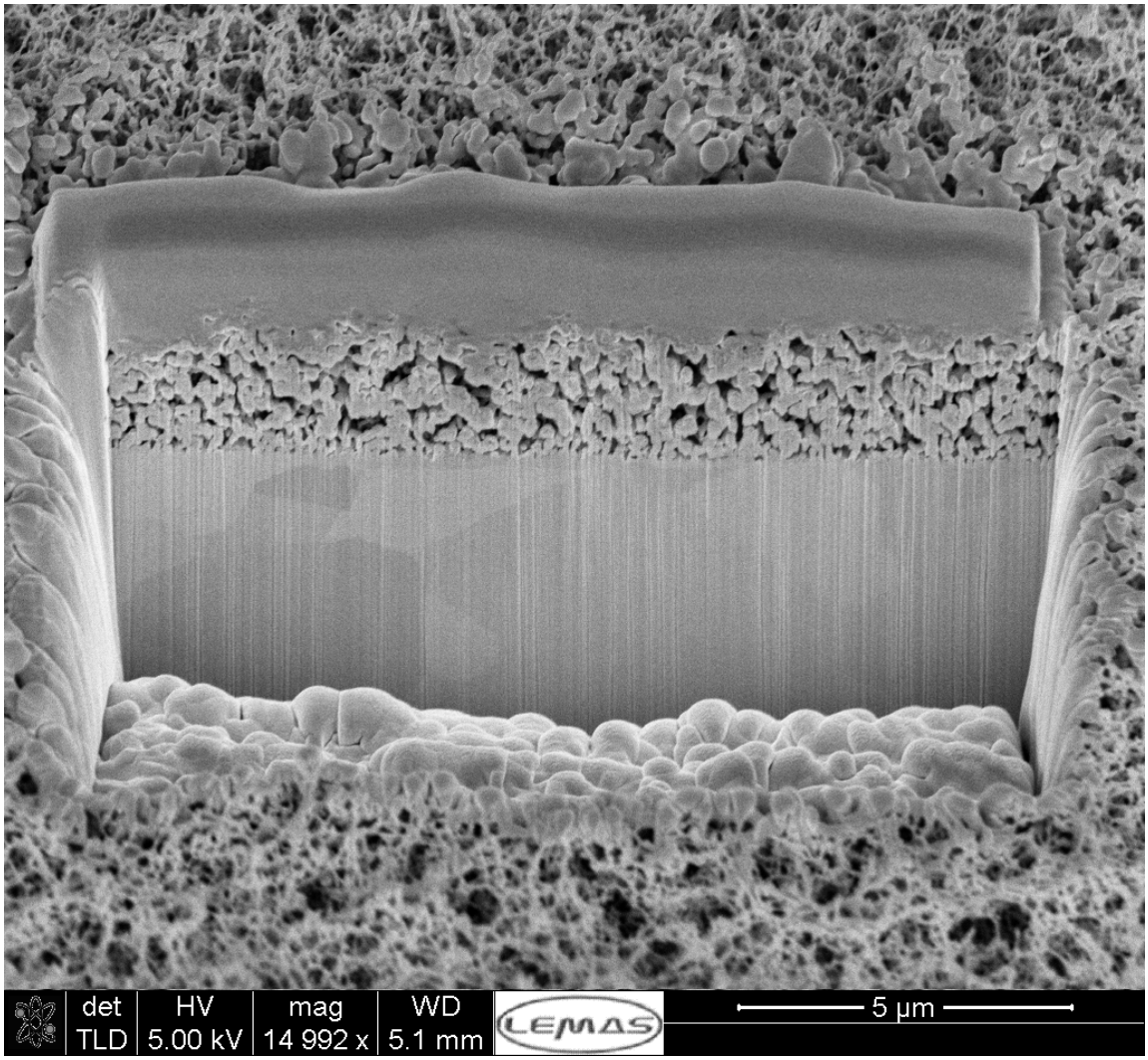

Figure 2.2: TEM image of fuzzy tungsten
Source: Courtesy of Aneeqa Khan through work done at DIFFER and LENFF.

The matter of plasma and neutron synergistically interacting has not received a lot of attention in the past because of the fact that this is only recently expected to be a problem with deuterium tritium capable devices such as ITER and DEMO. One aspect that requires possible direct examination is that of sputtering since the theoretical mechanism is based on cascade damage resulting in atoms being given enough energy to be displaced and then overcome the surface energy. Dated work on this has been found in papers such as (Harling *et al.*, 1975, 1976; Keller, 1968). The discussions here are on occasion slightly counter intuitive. All papers

categorically state that theoretical values for sputtering ratios are quite small (of the order 10^{-5} atoms sputtered per incident neutron) for neutrons of a fusion energy level ($\approx$14 MeV). However, there have been experiments that suggest otherwise obtaining sputtering ratios higher than expected. On the other end of the spectrum in Keller (1968), the authors did not find any sputtering in their experiment, however noted that they had previously obtained a sputter ratio of 0.5. Examination of this paper (Keller, 1966) shows the presence of thermal neutrons as well which could potentially be the responsible factor here. Keller (1968) talks about how sputtering is dependent upon mean free paths and how higher mean free paths indicate less likeliness of sputtering. Furthermore, sputtered particles were actually observed to have been in the from of micron sized chunks (Harling *et al.*, 1975). The overall trend however seemed to have settled towards lower orders of sputtering which is theoretically to be expected. This raises multiple questions. Firstly on the nature of neutron damage at the surface, secondly the exact nature of neutron interaction (which is largely based on experimental cross sections) and finally on sputtering mechanisms. A more recent paper (Ye *et al.*, 2000) seems to have resolved this using a Japanese fusion neutron source (which has since been shut down) stating that sputtering is indeed as low as theory predicts. The methodology however is slightly cumbersome and does not report sputtering values in a typical fashion.

The fundamental problem of materials used in a fusion environment is not simply of their lifetime within the condition but also of how they affect the plasma. Erosion and sputtering are expected to be very significant as well as affecting the plasma environment. One of the mechanisms by which this happens is Bremsstrahlung radiation (Figure 2.3) where electrons lose their energy interacting preferentially with high Z (atomic number) atoms. This is examined as a mechanism for heat loss in the paper Post *et al.* (2004) where the aim however was to use these mechanisms to reduce heat loads at plasma facing surfaces.

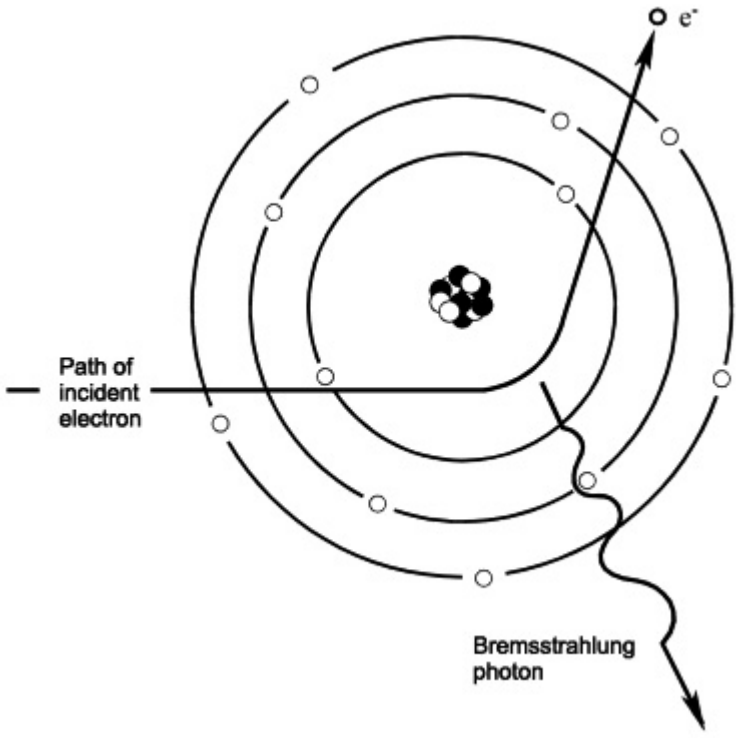

Figure 2.3: Mechanism of Bremstrahlung radiation

The paper Watanabe *et al.* (2011) is a key example of synergistic effects of plasma and neutron irradiation using ion irradiation as a proxy for both of these. A sample of tungsten was first irradiated by 2.4 MeV Cu^{2+} ions up to 1 dpa and then irradiated by deuterium ions. The results were analysed through TEM and then through annealment desorption. This analysis showed that the deuterium underwent higher absorption at the increased damage due to vacancies and other forms of damage acting as traps for the deuterium. Figure 2.4 illustrates this result.

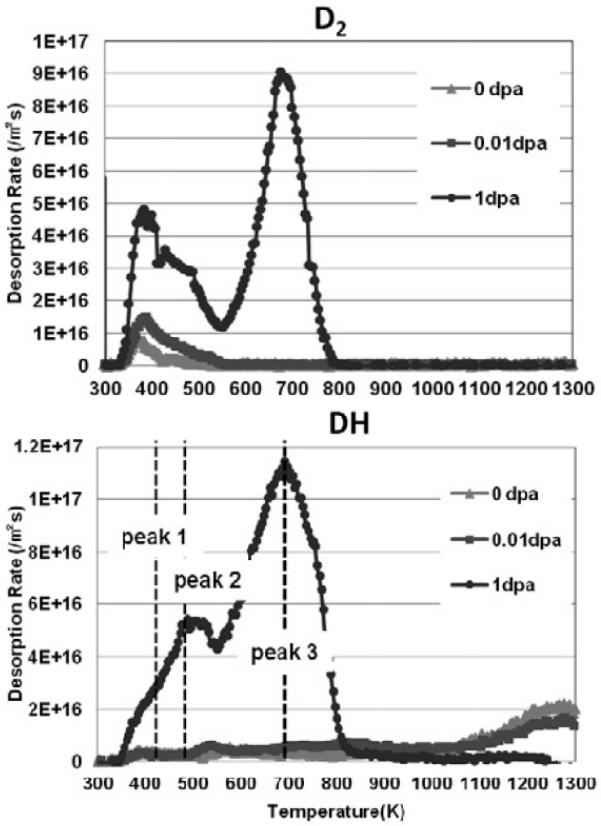

Figure 2.4: Deuterium (D_2) and deuterium hydride (DH) desorption in pure tungsten following ion irradiation (Cu^{2+})

An important consequence of this experiment is that it raises questions for tritium retention within plasma facing components since tritium is a controlled substance and is likely to have limited on site volume presence. Therefore, not only will well developed models allow for understanding possible routes to mitigation of this problem, it will also allow for better understanding of how much tritium is retained. Conservative models would hamper reactor operation by limiting further inventories of limited fuel.

Throughout this thesis therefore, a significant aim will be to investigate the behaviour of neutrons. The 14 MeV neutrons have a mean free path in the centimetre scale and therefore it is a question of what sort of impact they will have on the

direct surface (explained in Chapter 3). Therefore, it will be the purpose of this part to understand how neutrons create primary events and what effect this will have on the surface since the surface is the region of the first wall (on the micro meter scale) that would be likely to directly interact with plasma. To this end, three direct investigations are done:

1. Neutronics of 14 MeV neutrons in a slab geometry,
2. neutronics of 14 MeV neutrons in a shell geometry, and
3. molecular dynamics investigation of primary events in tungsten.

2.1 Basic Theory

2.1.1 Material Damage Theory

This section will be focused on developing an understanding of key phenomenon that occur in materials at an atomistic level. It is this that will define how the material is likely to behave and the consequence of continued particle impact. The basis for this approach is referred to as crystallography which states that materials are in a specific crystal structure. These theories can be found comprehensively stated in books such as Hammond (2002); Kittel (2010); Borchardt-Ott (2012). Over the course of this Chapter, when defects are discussed; the primary source for these will be the textbooks Hirth and Lothe (1949); Kelly and Knowles (2012). Where other sources are used these shall be stated.

2.1.1.1 Point defects

We commence with a discussion of point defects. Point defects are classified as either vacancies or interstitials. Consider a perfect crystal arrangement. A vacancy is defined as an empty site within this regular lattice. An interstitial is a site where there is either an extra atom in a position not part of the regular lattice or an atom that is different to atom in the crystal structure (i.e. a different element). These are illustrated in Figure 2.5.

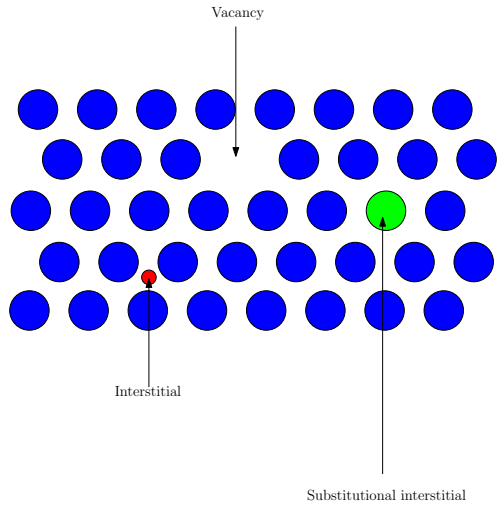

Figure 2.5: Illustration of point defects. Self-interstials are a special case where the interstitial atom is the same as a overall material.

Point defects are a common phenomenon that occur in crystal theory due to damage by particle irradiation due to "collision cascades". In this scenario where we do not consider substitutional interstitials, one can see how interstitials and vacancies are required mostly to go hand in hand (referred to as Frenkel Pairs). Collisions create primary knock on atoms which when they leave their original site form a vacancy. Where they come to rest, they are likely to form interstitials unless they simply replace a lattice site. In the latter case this would also eliminate a vacancy. Therefore, in the absence of additional particles and loss of particles through processes such as sputtering the number of interstitials and vacancies are equal. Ziegler *et al.* (2010)

provides a brief physical model of how collision cascades occurs. Take E_d to be the displacement energy of an atom at its perfect lattice site. When a collision occurs, based on momentum and energy conservation calculations one can determine the energies of the two particles under consideration ($E_1$and E_2 where $E_1$is the post collision energy of the incoming particle and E_2 is the post collision energy of the lattice atom). If E_2 is greater than E_d then a displacement will occur. If E_1 is greater than E_d a vacancy will be formed otherwise the incoming particle will replace the site and $E_1$is released as a photon. If both $E_1$and E_2 are less than E_d then an interstitial will be formed. This model is referred to as the Kinchin Pease model (Kinchin and Pease, 1955).

Displacement energy is something that can be calculated and is often done during electronic structure (ab initio) or molecular dynamics calculations. Using the principles of the conservation of energy and a perfect lattice, these can be evaluated. The theory has been adopted from Dudarev (2013).

The formation energy of a vacancy is given by:

$$E_f(vacancy) = E_{N-1} - (\frac{N-1}{N})E_N, \tag{2.1}$$

Where E_N is the energy of a perfect equilibrium crystallic lattice of N atoms and E_{N-1} is the energy of the same crystal with a single vacancy (therefore $N-1$ atoms) after the lattice has been allowed to relax.

The formation energy of a self interstitial atom is given by:

$$E_f(self\,interstitial) = E_{N+1} - (\frac{N+1}{N})E_N. \tag{2.2}$$

2.1.1.2 Dislocations

Point defects typically are hard to image directly with the current state of technology. What are however easily observable are dislocations. Dislocations are defined as faults occurring in the lattice structure. Here we shall consider the screw dislocation and the edge dislocation. Dislocations are commonly defined using the concept of Burgers vector which is illustrated in Figure 2.6. The Figure shows a simple cubic structure. A circuit is drawn around the imperfection which is then superimposed onto a perfect lattice. In order to close the circuit on the perfect lattice a vector is required which is the Burgers vector.

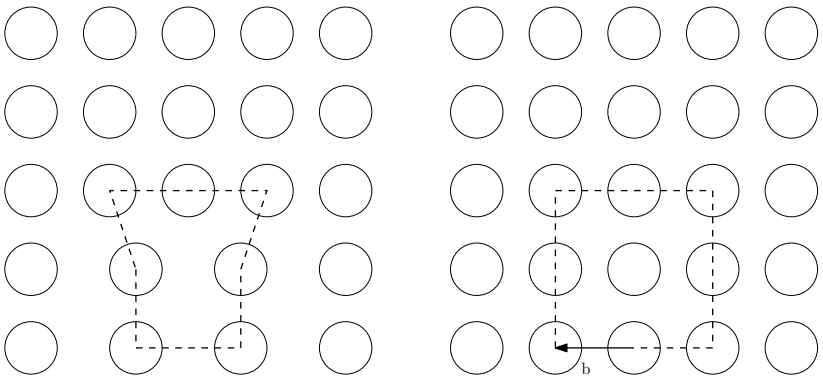

Figure 2.6: Burgers vector

An edge dislocation is defined as one whose Burgers vector lies normal to the dislocation length. A screw dislocation has its Burgers vector in parallel with the dislocation length. These are illustrated in Figure 2.7 where EE' is an edge dislocation and SS' is a screw dislocation within a simple cubic structure.

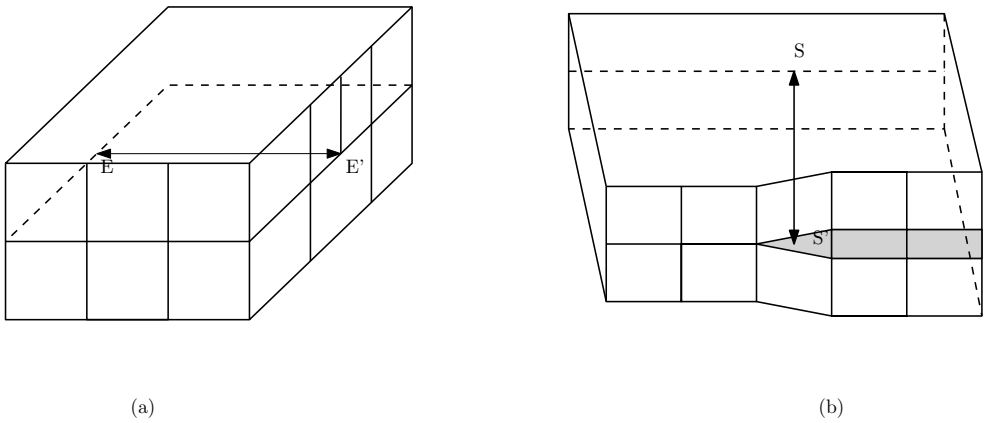

Figure 2.7: Dislocations
(a) Edge dislocation (b) Screw dislocation

Edge dislocations occur in nature. Materials are not entirely perfect crystals and as such these result in dislocations as well as other defects such as stacking faults (where the crystal is out of alignment). However, it is believed that these are what are responsible for the variable properties of materials. A potential mechanism for forming dislocations is the agglomeration of point defects which allows the system to achieve a lower energy state.

2.1.1.3 Defect clustering

Defects (in particular point defects) are not stationary. They move about within the material and are typically eliminated at either the surface or a grain boundary. These typically result in changing material properties and other effects such as helium embrittlement through helium interstitials formed as a result of transmutation migrating to the grain boundary. Effects such as these are typically modelled using methods such as kinetic Monte Carlo. Methods for doing this can be found in papers such as Kotomin and Kuzovkov (1992); Kotomin and Zaiser (1993); Kotomin *et al.* (1994).

2.1.1.4 Thermodynamics

Typically, due to the many bodied nature of a solid; it is quite cumbersome and difficult to actually be able to describe what is observed at the continuum scale. One treatment, however, involves using thermodynamic principles to quantify the behaviour. For instance, the free energy of the system can be determined by the number of point defects in the system,

$$G = H - TS, \tag{2.3}$$

Where G is the Gibbs free energy, H is the enthalpy which is a function of the internal energy, T is the temperature and S is the entropy of the system. Through statistical mechanics it is understood that the entropy is a function of the number of various formations the lattice can take,

$$S = k_B ln(W), \tag{2.4}$$

$$W = {}^{N}C_n = \frac{N!}{(N-n)!n!}, \tag{2.5}$$

Where k_B is the Boltzmann constant, W is the number of different configurations of N lattice sites with n point defects.

These methods allow determination of methods such as the number of point defects in a system through understand the enthalpy of formation.

The Kinchin Pease method (Section 2.1.1.1) is another example of energy considerations to quantify defect production.

2.1.2 Sputtering

Sputtering is defined as the ejection of atoms from the target surface by ion impact. An ion that has a high enough threshold energy to breach the surface energy of the target and then provides energy to the atom to escape the surface (Ziegler *et al.*, 2010; Stangeby, 2000). However, it is not as simple as demonstrated in Figure 2.8, which shows that this is not a linear function (which would be expected if the phenomenon was fully addressed by the explaination). The data are obtained through by work done by Eckstein *et al.*, 1980; Biersack and Eckstein, 1984; Eckstein and Biersack, 1985; Eckstein, 2005.

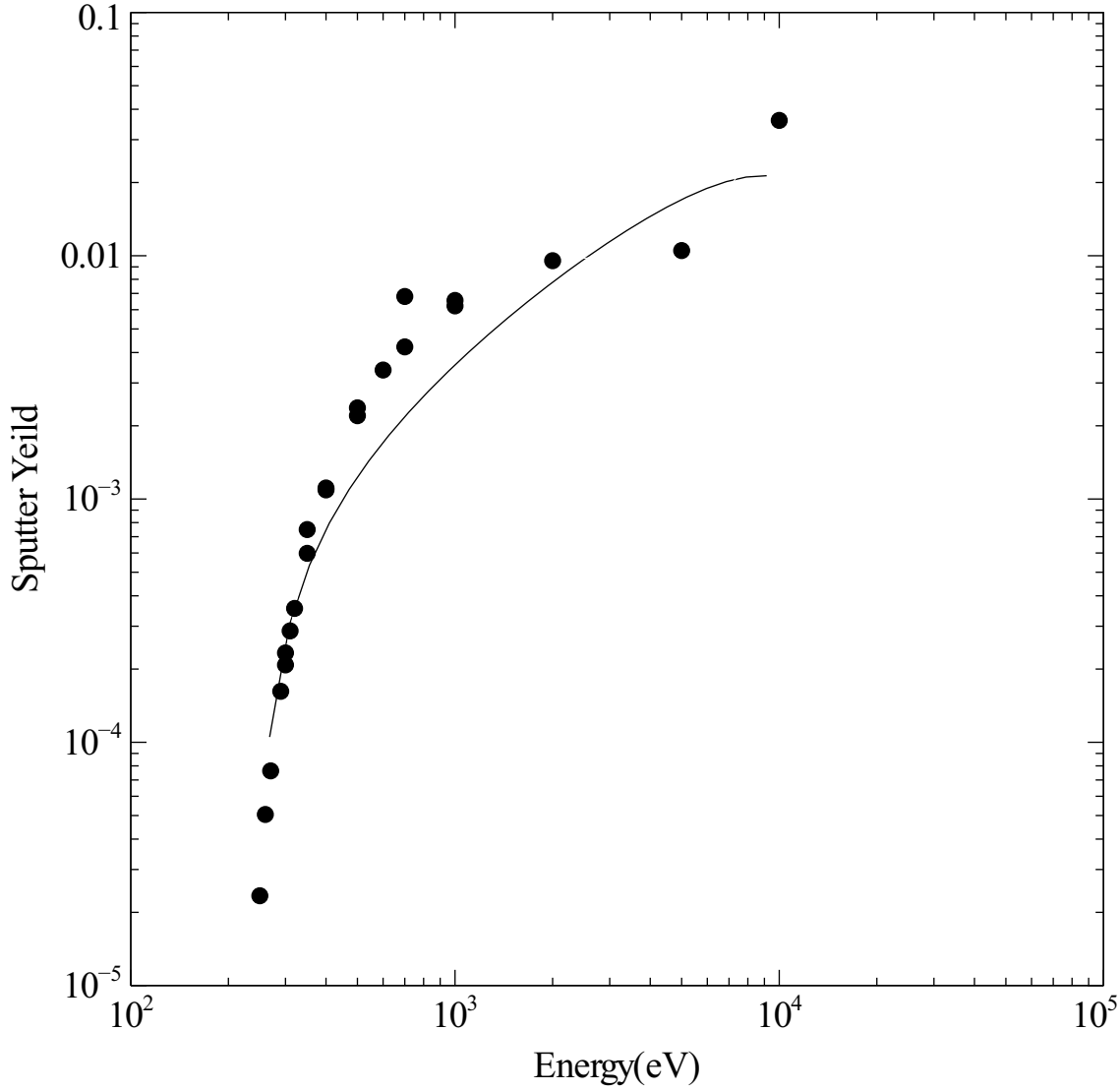

Figure 2.8: Plot of tungsten sputter yield due to deuterium atoms as a function of the inciden ion impact energy

Sputter yields due to deuterium ion impacts, the yield atoms ejected per ion impact.

Work is currently being done in determining the physical processes involved, however functional models are sufficiently developed (Sigmund, 1987). The linear sputter yield Equation states:

$$Y = \Lambda E_D, \tag{2.6}$$

Where Y is the sputter yield, Λ is the material constant as a function of the surface potential, interaction cross section, mass and number density, and E_D is the energy deposited per unit length. This has sufficient parameters to allow for an accurate enough description of light energetic ions.

Sputtering is a problem as this becomes a source of heavy atoms into the plasma (Stangeby, 2000). These take heat away from the core through Bremsstrahlung radiative heat loss causing heat loss in the plasma (Post *et al.*, 2004) and eventual plasma collapse. Losing heat in the core through various physical processes is currently the limiting factor for sustained fusion.

2.1.3 Plasma damage and ion transport

Aside from sputtering, one of the other primary effects of plasma damage is to implant ions into the first wall. As such, these require ion transport treatment through materials. This can be done using either binary collision simulation, molecular dynamic simulations or experimental procedures. Here we provide a brief view of how ions behave in material. For a more extensive treatment, the reader should refer to texts such as Ziegler *et al.* (2010).

Ion damage theory examines the effects of an incoming atom with the basis largely in the standard atom model and electrostatic forces. Consider charged ions going through an array of nuclei and electrons. These all interact through electrostatic forces and here we shall consider an ion and a target in isolation. The kinetic energy of the ion is given by:

$$E_k = \frac{1}{2} m_1 v_1^2, \tag{2.7}$$

Where E_k is the kinetic energy, m_1 is the mass of the ion, v_1 is the velocity of the ion. The potential energy is given as:

$$E_p = k_c \mid \frac{q_1 q_2}{r} \mid, \tag{2.8}$$

Where E_p is the potential energy, k_c is the Coulomb constant, q_1 is the charge on the incoming particle, q_2 is the charge on the target and r is the separation between the two. The distance of closest approach therefore is found when all the kinetic energy approaches zero and is converted to potential energy. Therefore, one may simply equate the potential and kinetic energy.

$$\frac{1}{2} m_1 v_1^2 = k_c \mid \frac{q_1 q_2}{r} \mid, \tag{2.9}$$

$$r = \mid \frac{2 k_c q_1 q_2}{m_1 v_1^2} \mid . \tag{2.10}$$

One can observe that r approaches zero as v approaches infinity. One can therefore compute how the particles get scattered by considering forces operating at very small time steps (the essence of molecular dynamics) or using a Monte Carlo approach where an event takes place at some stochastically determined point. One can now draw several straightforward conclusions. Firstly, direct nuclear scattering is less frequent than electrostatic scattering. In fact, Ziegler (1999) states that work done shown this to be very low. This can be understood in stark contrast with how neutrons travel further than ions and therefore have a completely different damage profile. Secondly, since electrons are far more numerous than nuclei, most of the energy lost is in fact to electrons. It does not matter that the electron is not as massive since distance of closest approach is independent of target mass. It should

be noted however that this a simple treatment. It does not take into account (for instance) electrons surrounding a nucleus. Lattices are held together with atoms having a potential energy due to this bonding. If enough energy is provided to overcome this, the atom is displaced. This is the basis on which ion damage works.

Figure 2.2 shows the formation of fuzzy tungsten which occurs when plasma ions (in this case He ions) enter the material surface and then coalesce to form porous regions. The mechanism for this is provided in Kajita *et al.*, 2009 with models for how this is expected to grow in Doerner *et al.*, 2011. Based on the theory of plasmas, the primary damage it seems will be from ion impacts and thus can be fully resolved using these theories. The manner in which they will differ is going to be based on their length and time scales. This can be seen in the illustration obtained from Wirth *et al.*, 2011 in Figure 2.9.

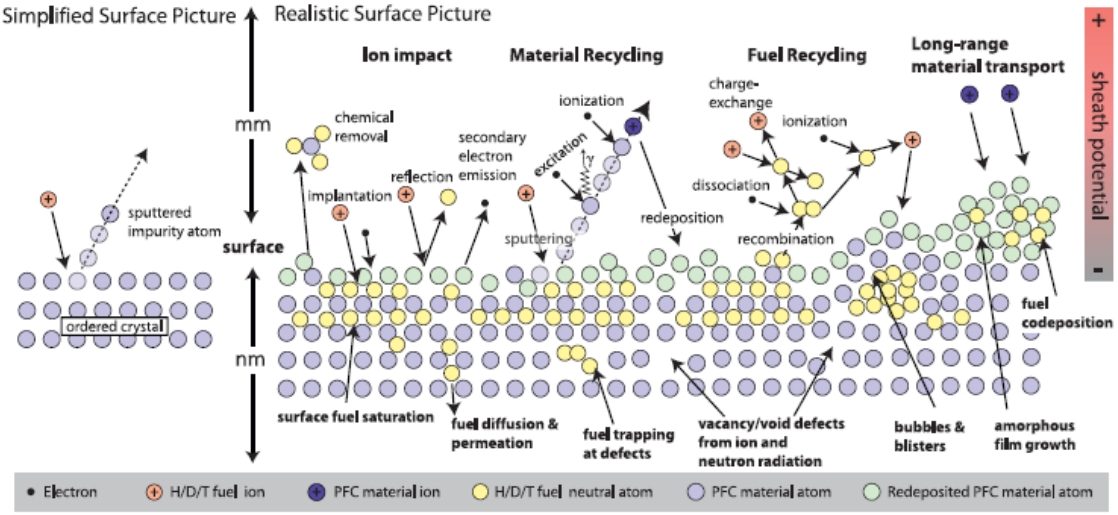

Figure 2.9: The various effects expected on materials within a fully functioning fusion reactor.

Source: Wirth *et al.* (2011)

2.1.4 Neutronics

Another dominant phenomenon within a fusion environment is that of neutrons. Neutrons and neutronics are therefore are essential towards a proper understanding of the problem at hand.

2.1.4.1 Neutron transport

Neutron transport is defined by a single equation which is standard. This equation is referred to as the neutron transport equation and is defined as follows.

$$\frac{\partial N}{\partial t} + v\Omega\nabla N + \sigma v N = \int_{\Omega}\int_{E} f\sigma' v' N' dE' d\Omega' + Q, \tag{2.11}$$

Where N represents neutron density as a function of position r, angle of travel Ω, energy E, and time t. σ is the nuclear cross section which is a function of angle of impact and energy. v is the neutron velocity. f is a probability factor for scattered neutrons. Q is a source term (such as fission or fusion neutrons). The dashes represent where other energy groups that scatter into the energy level under consideration are used.

The neutron transport equation (and other relevant theories) can be found in numerous textbooks such as Reilly *et al.* (1991); Lewis and Miller Jr. (1993); Lewis (2010)). It can be easily derived by considering a neutron balance. Considering neutrons within an energy range, angular and spatial region (in the case of the neutron transport equation, all of these discretisations are infinitesimally small); neutrons can only exit by either travelling out or by undergoing a scattering reaction. They can also enter the group by either being scattered in or through a source. These phenomenon are covered in the equation.

2.1.4.2 Elastic and Inelastic Scattering

The scope of neutronics within this report shall be concerned with scattering primarily because fission is essentially non existent within shielding materials by requirement.

When a neutron collides with a nucleus either an elastic or inelastic scattering will occur. Elastic scattering is when the neutron and nucleus combined conserve momentum and energy while inelastic scattering occurs when the collision excites the nucleus which is is later emitted as gamma radiation. These are illustrated in Figure 2.10.

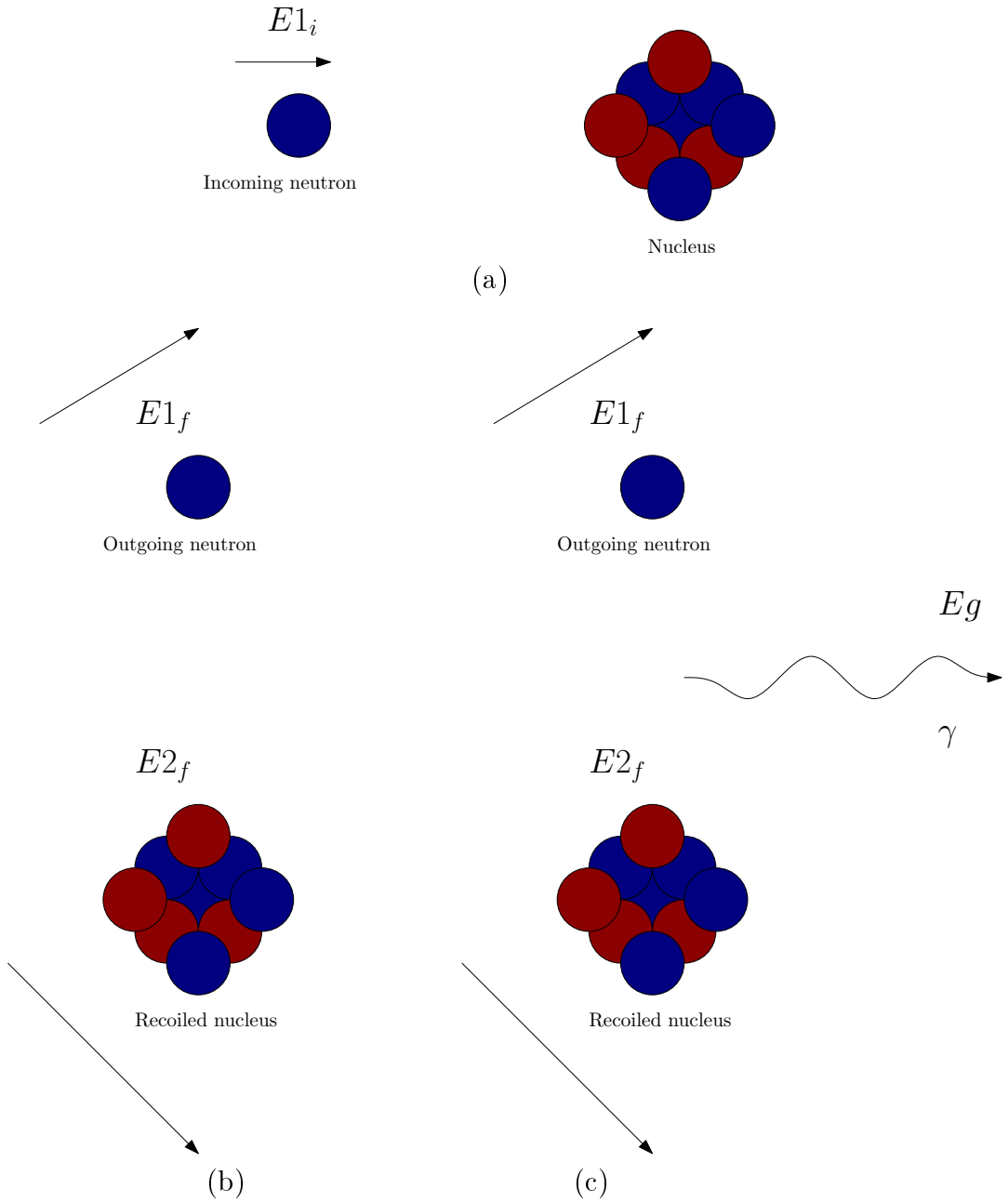

Figure 2.10: Depiction of neutron-nucleus scattering interaction.
(a) Before collision (b) Elastic Scattering (c) Inelastic scattering

2.1.4.3 Cross-sections and Optical Model

The cross section is a critical parameter in determining nuclear behaviour as can be seen from Equation 2.11. The cross section (σ) is defined as:

$$N_r = \phi\sigma, \tag{2.12}$$

Where N_r is the number of reactions occurred and ϕ is the incoming neutron flux. Typically cross section determination is done experimentally. An approach for this is to expose a material to neutron beam and measure the flux emitting from the sample using time of flight methods at facilities such as the CERN nTOF facility. This approach can be seen in papers such as Belloni *et al.*, 2013. Figures 2.11 and 2.12 show an imagined setup and a time of flight facility to do this.

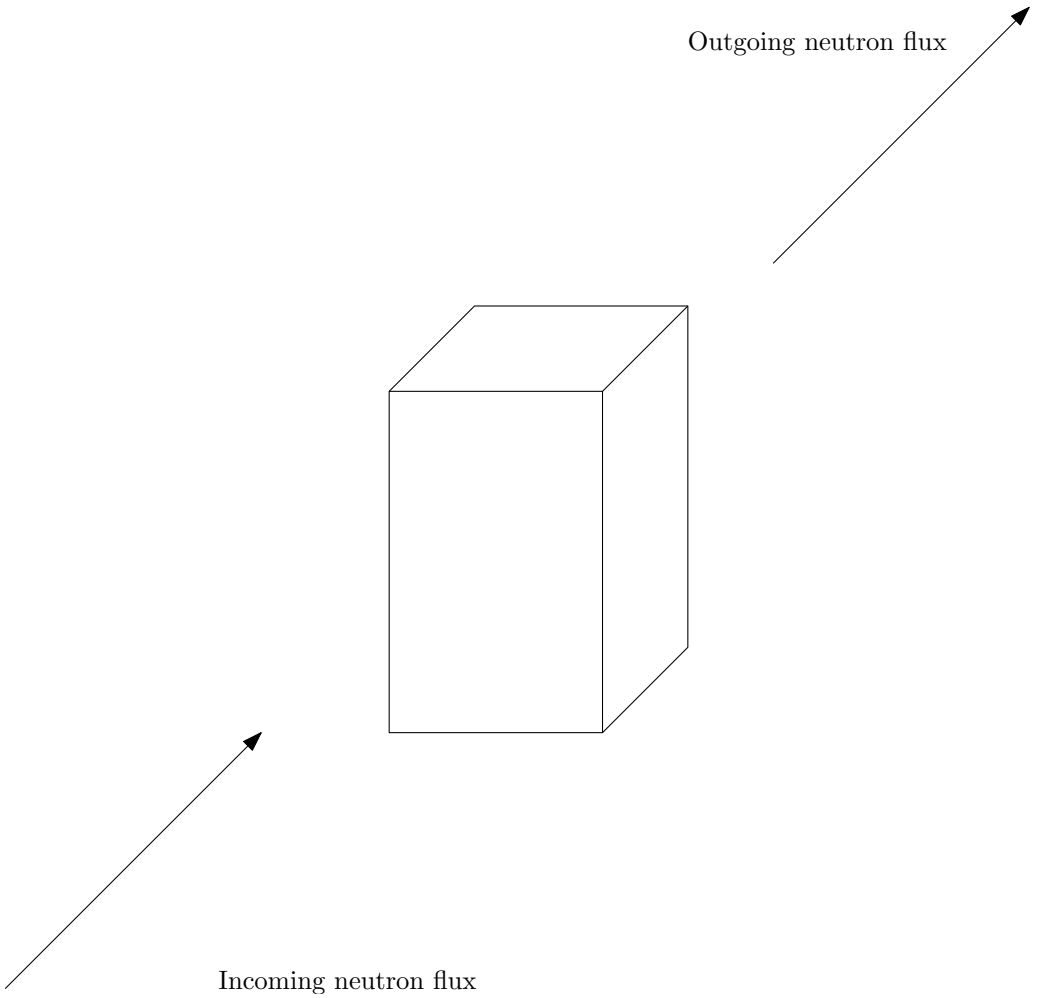

Figure 2.11: Setup for measuring neutron cross section.

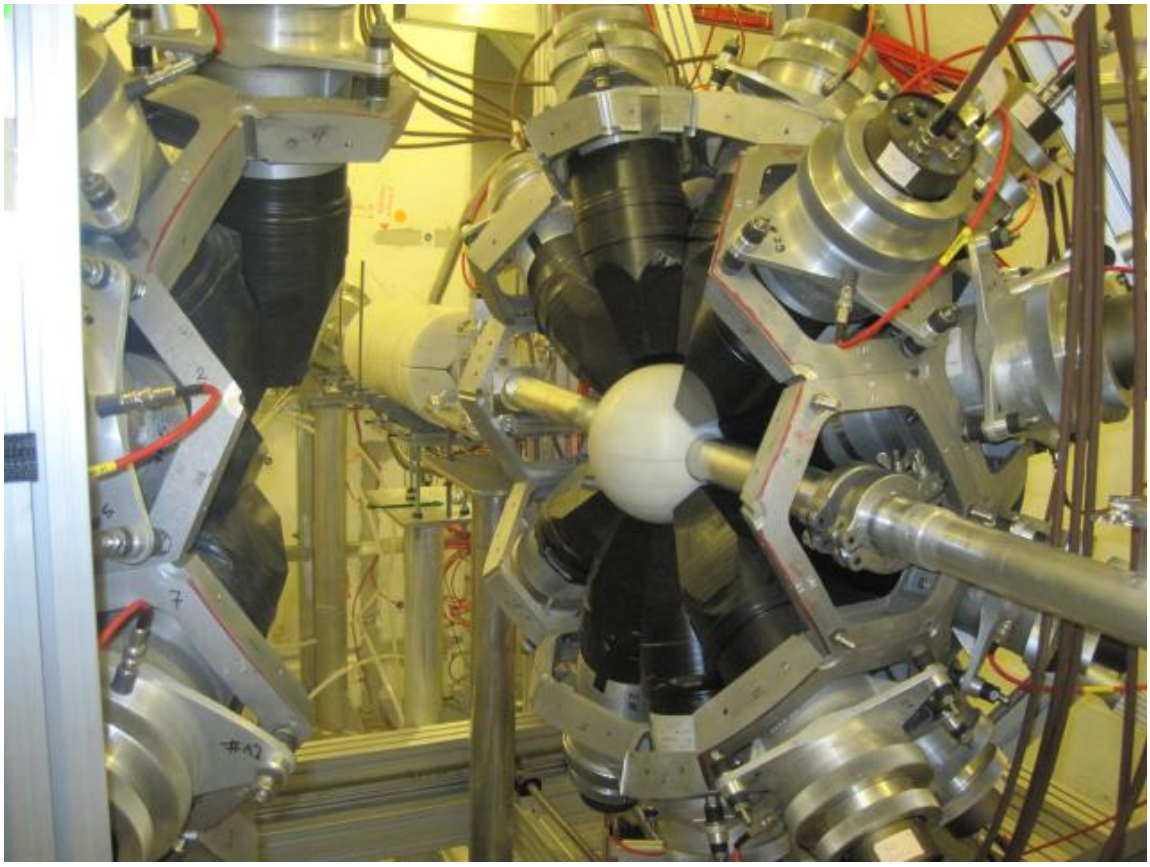

Figure 2.12: CERN nTOF facility
Source: cern.ch

This data is tabulated amongst various national databases which are compiled into an overall comprehensive library which is referred to as JANIS managed by the Nuclear Energy Association (NEA). An example of a cross section is provided in Figure 2.13.

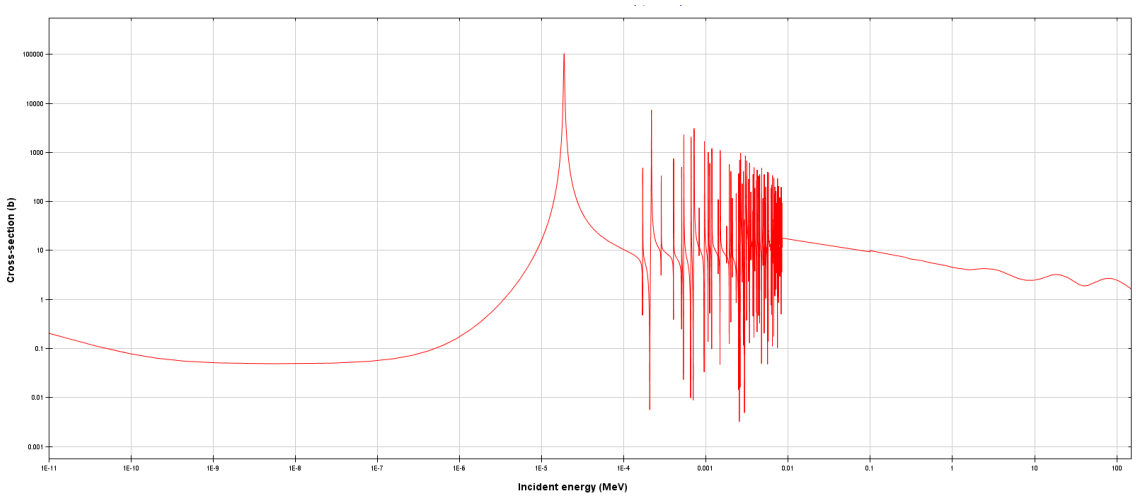

Figure 2.13: Cross-section of elastic collisions for tungsten-186.
Source: JANIS database

Experimentation does involve looking at bulk behaviour to infer nuclear properties. Furthermore it does not answer the intrinsic behaviour of how neutrons behave within material since if it was simple collisions occurring then one would assume that the probability for a collision is the same regardless of the incident neutron energy. This may be important in an attempt to determine mechanisms of plasma and neutronics interaction. There have been some successes in determining a theoretical approach towards cross section evaluation through quantum mechanics treatment. This overall approach is referred to as the optical model (in reference to treating neutrons as an optical wave). We shall present a basic idea of how this works without an in depth derivation or solution since this has not been examined thoroughly within the scope of the project. It is here to present an idea of the complexed physics involved. The presentation is based on postulates presented in Hodgson (1971); Schwabl (1992). We commence by restating the definition of the cross section in line with a scattering cross section analysis.

$$\frac{\partial\sigma}{\partial\Omega} = \frac{dN(\Omega)}{\phi}\frac{1}{\partial\Omega}, \tag{2.13}$$

Where $dN(\Omega)$ is the number of neutrons scattered into a solid angle Ω. The flux can be stated as:

$$\phi = \int_{-\infty}^{\infty} j.dt, \tag{2.14}$$

$$j = \frac{\hbar}{2mi}(\psi_0 * \nabla\psi_0 - \psi_0\nabla\psi_0), \tag{2.15}$$

Where j is the current density, $\hbar$ is Planck's constant and ψ_0 is the wave function (* indicates conjugate). Equation 2.15 is obtained from quantum mechanics derivations. The wave function follows Schroedinger's equation which states:

$$H\psi_K = E\psi_K, \tag{2.16}$$

$$H = E_K + E_P = (-\frac{\hbar^2}{2m}\nabla^2 + V), \tag{2.17}$$

Where H is the Hamiltonian of the system, E is the energy eigenvalue, E_K is the kinetic energy and E_P is the potential energy. The ψ_0 which is the wave function at time 0, is the superposition of the solutions to the Schroedinger Equation (Equation 2.16).

$$\psi_0(x, t_0) = \int A_k\psi_k.\frac{d^3k}{(2\pi)^3}. \tag{2.18}$$

This lays out the initial basis for the quantum mechanical treatment of cross sections. Solutions require further treatment of the potential function which can be found within references Hodgson (1971); Schwabl (1992).

2.1.5 Molecular Dynamics (MD)

Molecular dynamics (MD) is an approximation that deals with atomistic behaviour. It uses an inter atomic potential to approximate behaviour between atoms. This allows for simulations of larger systems (up to a few million atoms versus electronic structure that can only deal with a few hundred at best). The interatomic potential can be developed through either universal potential functions (for example ZBL developed during work for SRIM (Ziegler *et al.*, 2010)) or through electronic structure calculations using fitting methods such as the embedded atom model (EAM) (Nordlund *et al.*, 1997; Daw *et al.*, 1993).

The methodology for molecular dynamics will be based on information provided in the manual for MD code LAMMPS (Plimpton, 1995).

Molecular dynamics typically treats atoms as Newtonian particles acting under classical physics. Inter atomic potentials provide the energy between two atoms as a function of their distance.

$$E_{ij} = f(r), \tag{2.19}$$

Where E_{ij} is the energy between atom i and j as a function of the separation r. The rate of change of momentum is defined as the force.

$$\frac{d(mv)}{dt} = m\frac{dv}{dt} = F, \tag{2.20}$$

Where m is the mass, v velocity, t time and F force. The velocity of an atom can be determined through kinetic energy and thermodynamic equivalents.

$$E = \frac{1}{2}mv^2 = \frac{1}{2}k_B T. \tag{2.21}$$

These highlight the fundamentals of molecular dynamic simulations. However, actual Equationtions are a lot more elegant with thermodynamic treatments a core part of the problem to develop equilibrium models by equating thermal and potential energy that binds atoms together in order to determine the state (solid, liquid or gas).

2.1.5.1 Embedded Atom Model

The Embedded Atom Model (EAM) (Daw *et al.*, 1993) takes the idea of a potential a step further. A pair-potential has the problem that it fails to account for energies of various multi-body configurations. Therefore the embedded atom model develops the potential by fitting various multi-body configurations (such as interstitials, divacancies, etc.) and ensuring that a pair-potential represents these. The Equationtion for the EAM is given by:

$$E_i = F_\alpha(\sum_{i \neq j} \rho_\beta(r_{ij})) + \frac{1}{2}\sum_{i \neq j} \phi_{\alpha\beta}(r_{ij}), \tag{2.22}$$

where r_{ij} is the distance between two atoms, F is an embedding function, ρ the electronic density, ϕ is the pair potential function, with α and β representating the kind of molecular species (or the specific atom). Algorithms such as Ercolessi and Adams (1994) can be used to fit the potential.

2.1.5.2 Electronic Effects and Two-temperature Model (TTM)

Within higher energy projectiles, electronic effects result in significant drag on it thus reducing the actual nuclear damage caused (Sigmund and Schinner, 2002). Within molecular dynamics, this is treated by the two-temperature model (Duffy and Rutherford, 2007; Khakshouri and Duffy, 2009; Zarkadoula *et al.*, 2014a,b). The two temperature model treats electronic effects by considering the electronic system as a heat sink. By considering a finite element analysis, the projectile loses energy to electronic system which is converted into heat therein. This is found to be a good approximation to the electronic effects as demonstrated in Race *et al.* (2010a,b, 2013). The fundamental equation for the two temperature model is given by:

$$C_e \rho_e \frac{\partial T_e}{\partial t} = \nabla(\kappa_e \nabla T_e) - g_p(T_e - T_a) + g_s T'_a, \tag{2.23}$$

where C_e is the specific heat, ρ_e is electronic density, κ_e is the electronic thermal conductivity, and T is the temperature (T' refers to the initial temperature of the system). a and e refer to the atomic and electronic subsystems. The coupling parameters are g_p (electron ion interaction) and g_s (electronic stopping coupling parameter).

Chapter 3

Considering Surface Damage Due to High Energy Neutrons in Tungsten Using Monte Carlo Neutron Transport and Binary Collision Approximation

3.1 Introduction

This Chapter is presented as a result of work done while investigating the synergestic effects of plasma damage and neutron irradiation. As such, it was noted, that most conclusions to the afore stated phenomenon were based on using ion damage experiments as a proxy. It was therefore deemed necessary to investigate what neutron damage would likely be. Computational modelling methods were used to determine the nature of surface damage in comparison to bulk damage within tungsten, the

candidate material for fusion reactors. In particular, we use Monte Carlo neutron transport and binary collision approximation codes. A simulation setup to record collisions within a slab of tungsten and then isolate the collisions within the surface to determine the varying nature of damage was performed.

3.2 Literature and Motivation

As the world pushes towards developing viable fusion energy, questions are raised over being able to withstand and maintain the extreme environment within a reactor. In particular, material challenges are a severe hindrance. These are highlighted elsewhere (Wirth *et al.*, 2011). To simply list some of the problems that materials are likely to face in a functioning fusion reactor are: 14.1 MeV average energy neutrons; the production of 3.5 MeV alpha particles; ion damage from plasma formed when forcing a deuterium-tritium (DT) fusion reaction; high heat loads on material surface (within DEMO this is expected to be 20 MW per sq. meter (Maisonnier *et al.*, 2005)); the formation of a potential (Debye sheath) on the surface. While these conditions are extremely challenging individually, there is also further concern that these effects may influence each other. This is a problem since the design life of the divertor monoblocks in a commercial fusion reactor is aimed to be at 5 years. In particular the "synergestic effects" of plasma and neutron damage are of primary concern. The possible synergistic effects are illustrated in Wirth *et al.* (2011). A fundamental problem with fusion neutron damage is that currently it is hard to generate this experimentally in a manner that is representative of a reactor. This is because, 14 MeV neutron sources are rare and less likely to be developed due to the difficulty in operating and the timescales involved in realistic irradiation due to low fluxes. Therefore, the damage is mimicked using ion damage experiments (or in some situations fast fission reactors). Work which examines these problems are,

for example, Barabash *et al.* (2003); Kwast *et al.* (1996); Watanabe *et al.* (2011); Tyburska *et al.* (2009). All these point to a multitude of problems such as difference in heat transport properties which will likely affect plasma interaction within the material at, for example, the limiters and divertors. Furthermore, a key problem identified as a direct result of these experiments is that of tritium retention. All work points to enhanced tritium retention, possibly due to the fact that the voids formed by the neutron damage are likely to become traps for tritium. However, there is a problem with these simulated experiments. They do not take into account the penetration of neutrons. 14 MeV neutrons have a mean free path of approximately 3 cm within tungsten. This was calculated using the cross section obtained from library values. In this case, the cross section for W-182 for 14 MeV neutrons from the JEFF-3.2 library is 5.31 barns. The concept of a mean free path, λ, is explored in standard textbooks of nuclear physics and/or engineering (Duderstadt and Hamilton, 1976; Was, 2007). Probability for collisions takes the form of $P(collision) = 1 - e^{-\lambda x}$ where x is the distance from the surface. On substitution, it is clear that neutrons are unlikely to cause a lot of collisions near surface, which is the scale over which plasma damage occurs. Therefore, damage that interacts must be those caused by neutrons back scattered after an event within the depth of the target. This concept is further explored by neutron sputtering experiments. Sputtering is an event characterised by cascades which eventually result in an atom being given enough energy to be displaced in a specific direction and then escape to the surface (Sigmund, 1987). One can therefore see that if the range over which the energy deposited of a particle is large, sputtering is less likely. Studies have shown very little sputtering due to fast neutrons (approximately two orders of magnitude less than the equivalent energy ion) (Harling *et al.*, 1975, 1976; Ye *et al.*, 2000) . Therefore, there is motivation to examine exactly what the state of the surface will be through neutron damage.

3.3 Methodology

To calculate damage using neutrons, computational methods are used. Here, two codes are interfaced: namely MCNP4C and SRIM (Ziegler *et al.*, 2010). MCNP (Goorley *et al.*, 2012) is an n-particle Monte Carlo code used to simulate the transport of neutrons. SRIM is a binary collision code that is used to evaluate damage in materials (SRIM is the abbreviated form of Stopping and Range of Ions in Matter). A similar method is described elsewhere in Khorsandi *et al.* (2006). Firstly, the damage source is simulated in MCNP. A point source of 14 MeV neutrons is used and targeted towards a 100 cm deep tungsten slab (a point source is suitable since the analysis is collapsed later into 1D and is a simpler simulation). All collisions are then recorded and stored (within MCNP, this is approach is referred to as the *ptrac* card). These contain the energy a neutron has prior to a collision. This needs to be analysed to determine the energy of a primary knock on atom using the hard sphere approximation (Ziegler *et al.*, 2010). This provides us with a Equation for the recoiling atom as:

$$E_T r = \frac{4E_0 M_1 M_2}{(M_1 + M_2)^2} sin^2\theta, \tag{3.1}$$

where $E_T r$ is the transmitted energy, E_0 is the incident energy of the neutron, M_1 is the mass of the neutron, M_2 is the mass of the target atom, and θ is the recoil direction. The problem is simplified by assuming isotropic scattering:

$$E_T r = \frac{1}{2}.\frac{4E_0 M_1 M_2}{(M_1 + M_2)^2}. \tag{3.2}$$

The calculated transmitted energy is used as input into SRIM. SRIM forms an "invisible ion" to simulate the effects of a primary knock on atom (PKA) giving the output as Displacements/Angstrom-Ion which are converted to Displacements/Angstrom-Collision (Figure 3.1). The area under the curve thus represents the total number

of displacements per neutron collision.

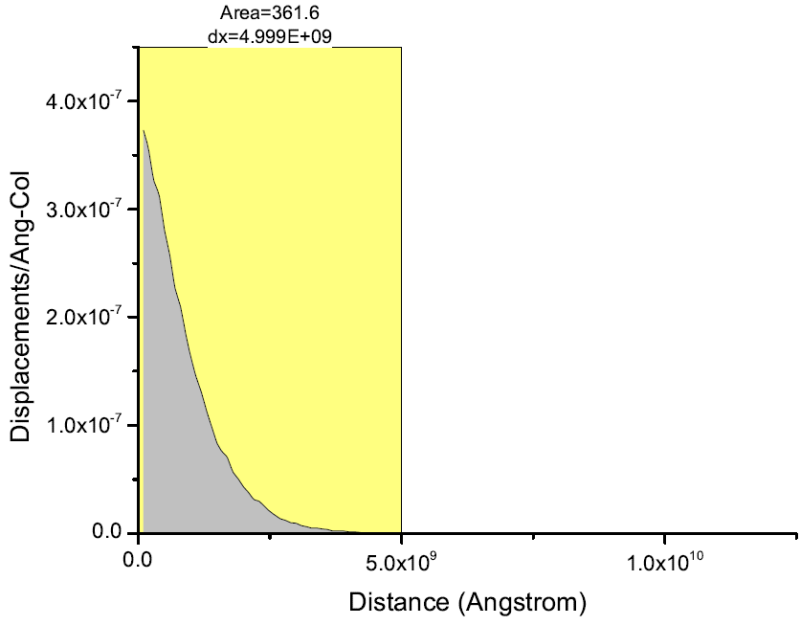

Figure 3.1: Pre-processed data from SRIM for bulk tungsten damage

A DEMO conceptual design (Maisonnier *et al.*, 2005) suggests that DEMO would be expected to operate at 5 GW. This is equivalent to $3.12 \times 10^{22}\, MeV\, s^{-1}$. Each DT fusion reaction outputs 17.6 MeV and is responsible for one neutron. This provides the neutron fluence as $1.77 \times 10^{21} s^{-1}$. The poloidal cross section of the Tokamak is approximated as a semicircle of radius 6 m. Considering that the major radius would be 9.55m, the total surface area is assumed as $1.851 \times 10^{7}\, cm^2$. This allows one to derive a neutron flux of $9.56 \times 10^{13} cm^{-2}\, s^{-1}$. One can now determine the damage in standard displacement per atom (DPA) terms. Since through SRIM the displacement due to each collision is obtained, this is normalised for the atoms present in the volume considered. A major assumption here is the number of collisions due to each neutron as each neutron generates multiple events. This parameter is estimated using the collision data obtained by averaging over the number histories within the simulation. This information is then used to scale the per collision displacements to per neutron collision in terms of DPA per second. This is further multiplied by a

time factor ($3.15 \times 10^7\ s\,per\,yr$) to provide the annual DPA. This provides an average value which can be used to scale the damage values to represent the variation with depth.

3.4 Results and Discussions

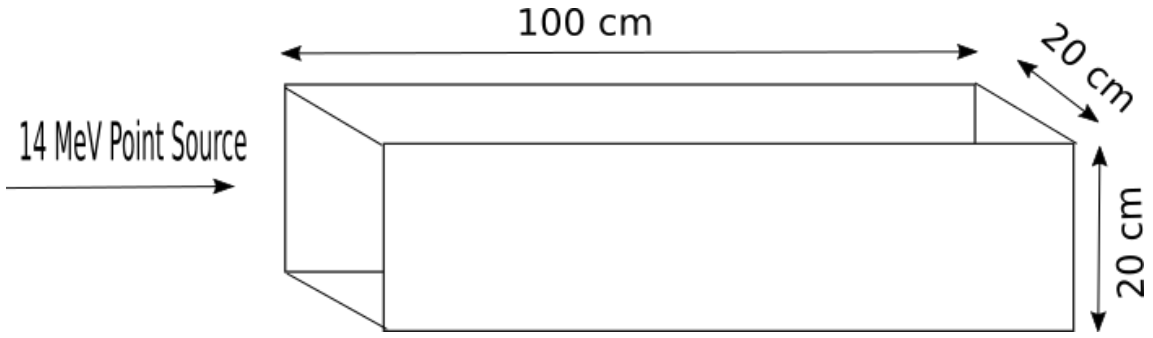

Figure 3.2: Setup for MCNP simulation.

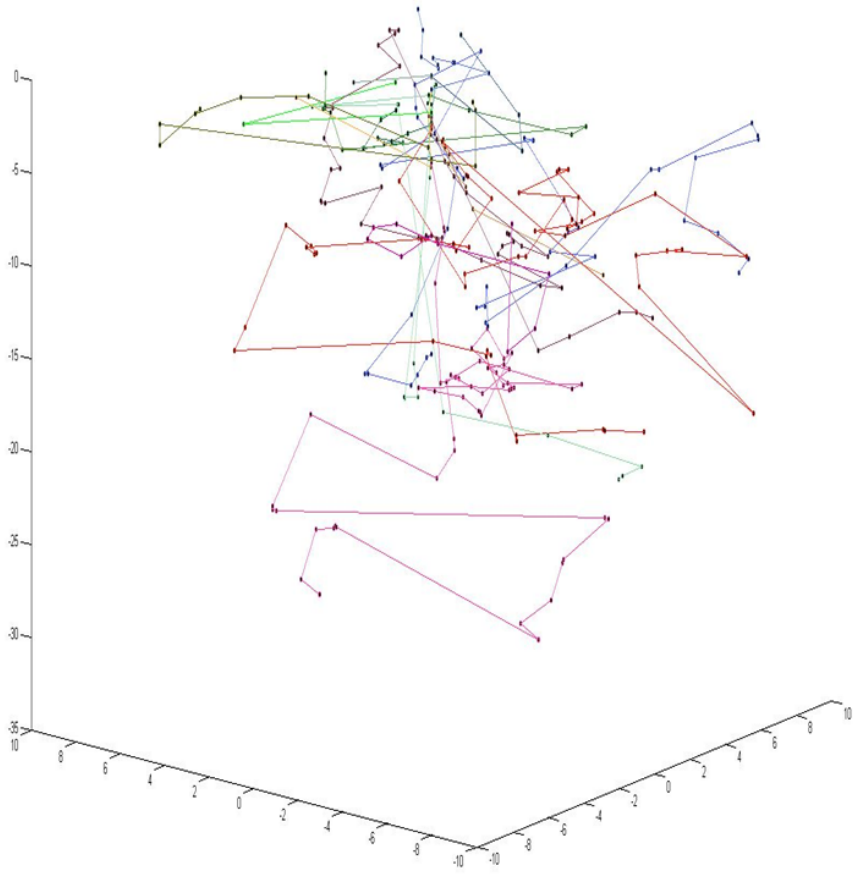

Figure 3.3: Trajectory of neutrons within the slab geometry in Cartesian coordinates.

A 100 cm slab of tungsten was subject to a source of 14 MeV neutrons using 10^5 particles. The setup is illustrated in Figure 3.2 and the flow of neutrons visualised in Figure 3.3. This number was used because it was the largest practical simulation that could be run. This was then processed to provide the damage (Figure 3.4). Within the bulk the collisions per neutron were found to be approximately 24. It should be noted that the bulk collisions would appear to be lower than expected. This is possibly due to the fact no reflective or peridoic boundary conditions were used in the simulation, which results in neutrons escaping the region.

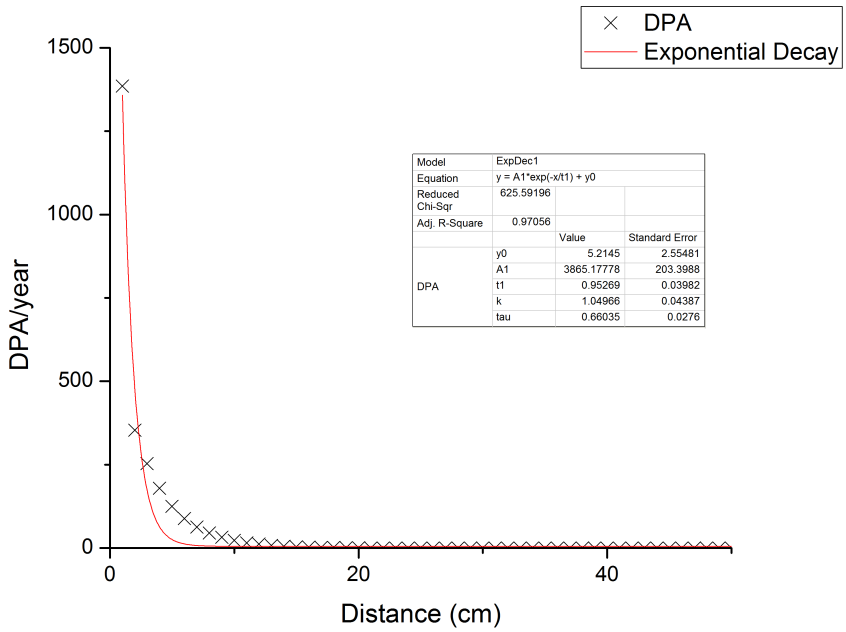

Figure 3.4: Damage prediction for full (non-surface simulation) 100 cm slab of tungsten

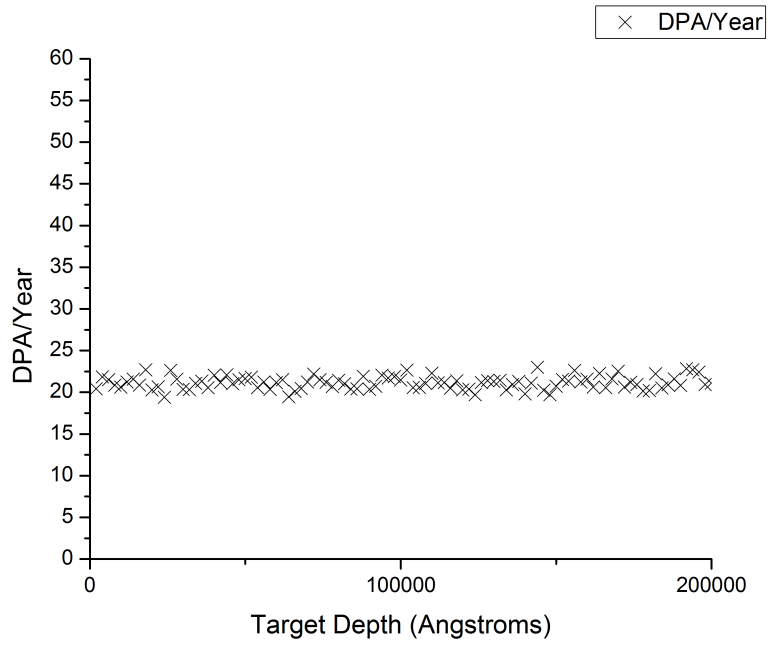

Figure 3.5: Surface (20 micron) damage illustration due to 14 MeV neutrons

The damage would appear to correspond to trends one would expect. One should note that these predictions are dependant on the cross-section library used, as illustrated in Gilbert *et al.* (2013). It may appear that these damage levels are high but it should be noted that the assumptions of hard ball collision and all collisions being elastic scatters explain this. Similarly, a simulation was set to record only the collisions that occurred within the surface (20 micron depth). Since more trajectories could be reasonably processed in this scenario, the simulation was increased to process 10^8 neutrons (Figure 3.5).

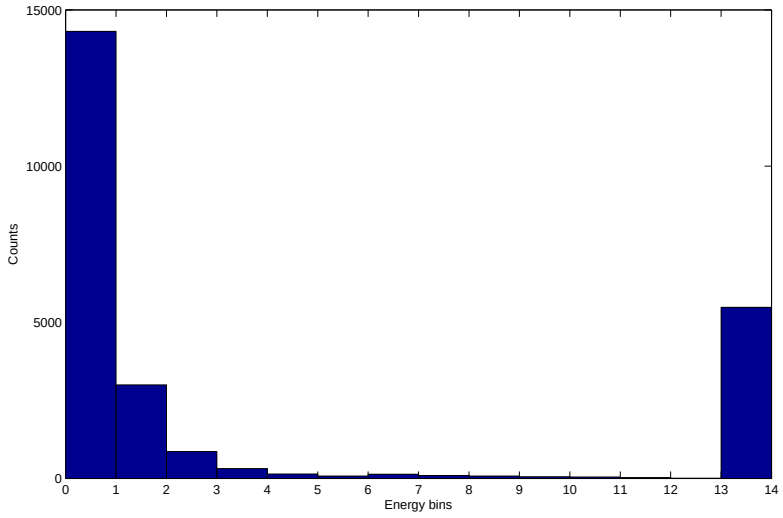

Figure 3.6: Histogram of collisions occuring in the surface

The disparity between the bulk and the surface damage is clear. This leads one to consider the fundamental nuclear physics that is in operation to result in this disparity. It has already been previously stated that by observation of literature and texts, the likley candidate for extensive damage in the surface is back-scattered neutrons. It is therefore imperative to examine the nature of these. An attempt to do so is made in the histogram shown in Figure 3.6. While there are some events that are of the 14 MeV energy, the large majority of them are within the thermal region (0 to 1 MeV). Furthermore, the 14 MeV neutrons are only likely to result in a single

event, causing surface damage, and then carry on to greater depths. The neutrons that cause damage are likely to be at a lower energy and therefore have significant local impact. However, it is difficult to be more qualitative by looking at simply one localised region. It would however be clearer if a continuous distribution could be determined allowed the change in damage to be seen. An attempt is made to do this here by analysing the bulk collisions. It has been suggested that the damage has a linear relation to the energy of the collision/event (Equation 3.1). Therefore, a tally was conducted where the energy of collision was converted to eV and summed for all events within a small region of 35 microns. This was then plotted onto a cumulative histogram as a semi-log plot (Figure 3.7). As one can observe the collisions "step up" at approximately the 10^4 micron(cm scale). Eventually after the 10^5 micron mark, most collisions have occurred.

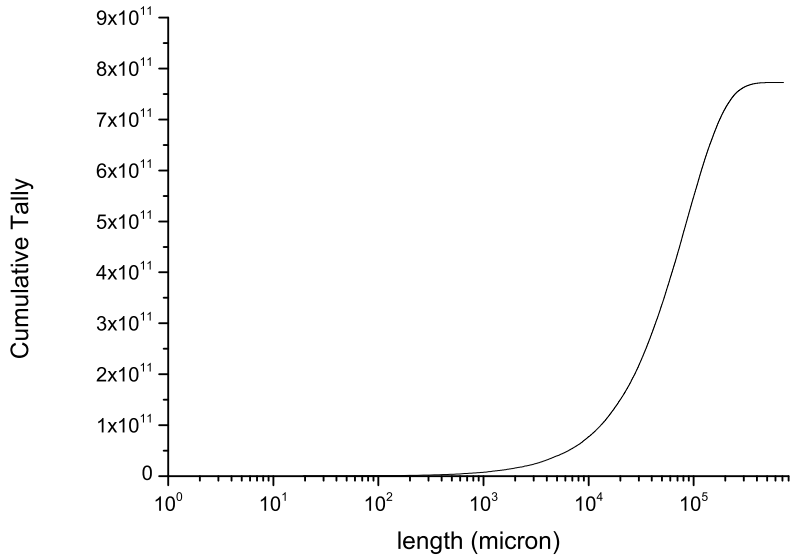

Figure 3.7: Semi log cumulative tally of collision energy

Another analysis was subsequently conducted where 40 micron slices were taken all the way from 0 to 40 cm in the material. The resulting events were put into 1 MeV bins. It should be noted that this is before the event and therefore not specifically

a primary knock on (PKA). This is demonstrated in Figure 3.8. It should also be noted that each slice was its own simulation. Therefore the trend observed is more credible since the results are completely independent of one another. It can clearly be observed that there is a peak in the 0 to 1 MeV distribution in the subsurface. These are the events that are more likely to cause localised damage. The flux distribution in Figure 3.9 which shows the neutron flux at various surfaces. Notice that as one progresses into the material, the tail (thermal events) rises.

3.5 Conclusion

With these results, it should be evident that surface damage will be significantly less than the bulk damage particularly when one considers the problem of a mean free path. This is highlighted in works (Harling *et al.*, 1975, 1976; Ye *et al.*, 2000) which considered neutron sputtering which again classify the lack of sputtering due to the high mean free path. However, there are certain improvements that could be made. Future work plans on investigating the continuous distribution of the damage. One of the ways we expect to do this is through either simplified analysis or using numerical approaches to the neutron transport problem. Furthermore, the quality of the simulation could also be further improved. For instance, reflective boundary conditions would be more indicative of neutrons coming in from all other sides and stopping the neutrons from escaping. Currently however, this was computationally difficult due to the number of events generated. Also, using the number of neutron events as a multiplier in the damage calculator is also cumbersome and probably unreliable.

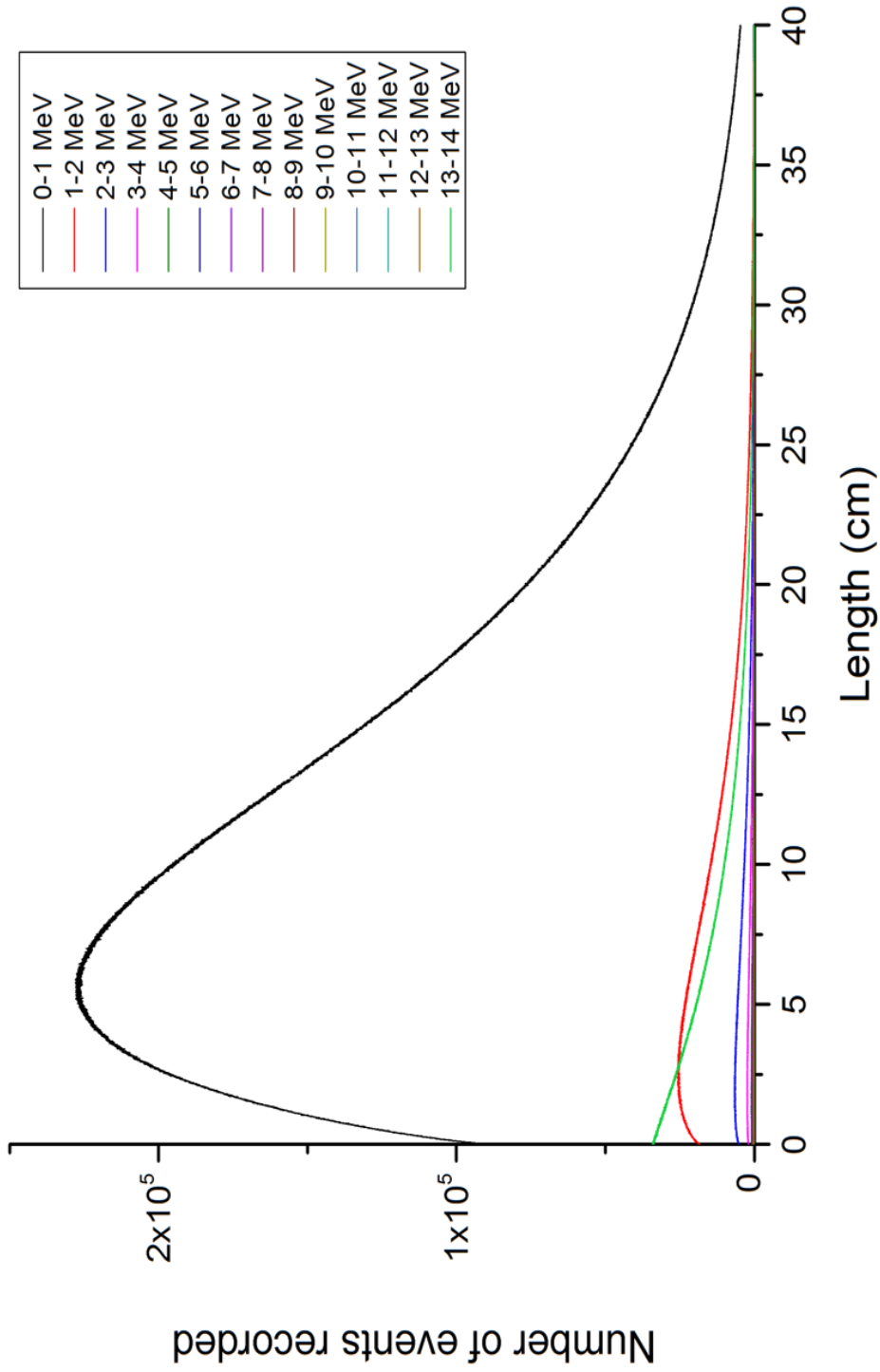

Figure 3.8: Distribution of events within the slab geometry.

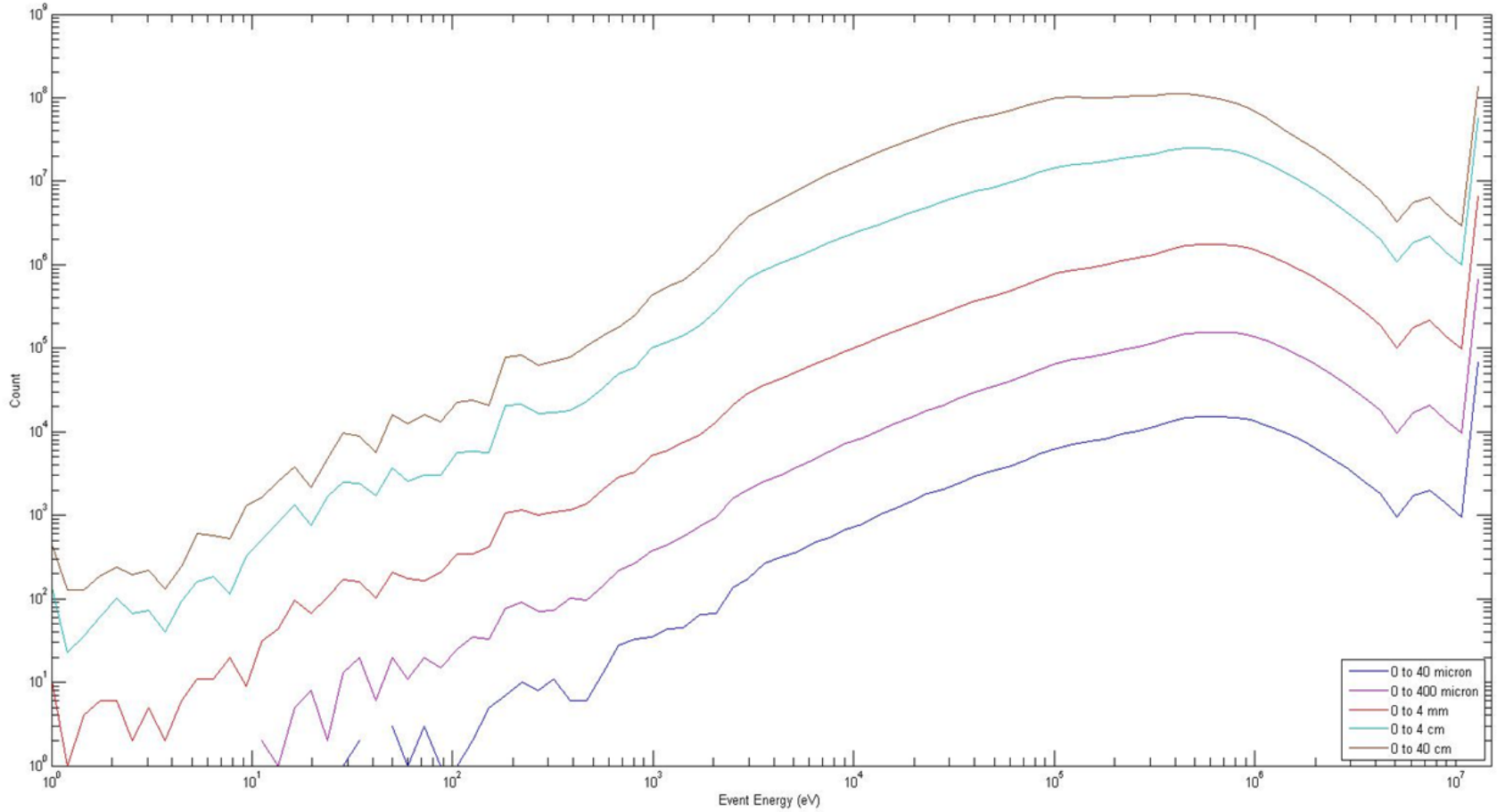

Figure 3.9: Distribution of neutron flux within the slab geometry as a function of depth.

Chapter 4

Neutronics Analysis in a Spherical Shell

4.1 Introduction

One of the key problems for a fusion reactor is that of 14 MeV neutrons and their deleterious effects on the behaviour of the materials forming the reactor. These are likely to create synergistic effects with the plasma damage which has been reviewed in works such as Wirth *et al.* (2011).

A previous study done (Hussain et al - in prep, Chapter 3) suggests that if 14 MeV neutrons directly impact a material, they would only likely affect in deeper regions of the material. However, it was also noted that the reason for this is that the neutrons cause localised damage once they have been moderated. These moderating capabilities may be affected by the material. Therefore there was an aim to create a study that would investigate the effect of moderated and back-scattered neutrons. The work itself is an extension of a previous work conducted

by Gilbert and Sublet (2016). The work simulated a tungsten shell surrounded by a homogeneous mixture of ferritic steel and water. This mimics a fusion reactor better since it has neutrons produced in a vacuum and attacking a tungsten shell surrounded by structural material.

4.2 Methodology

During the study, two fundamental methods of simulation were coupled. These were primarily MCNP6 (Goorley *et al.*, 2012) and Spectra-PKA (Gilbert *et al.*, 2015).

Monte Carlo N-Particle (MCNP) is a particle transport code developed at Los Alamos National Laboratories. It uses a probability based random number generator based on cross-sections. Further details of this approach can be found in references such as Lewis and Miller Jr. (1993); Lewis (2010).

Spectra-PKA is a tool for resolving primary events following the calculation of neutron flux within a system. It does so by deriving cross sections for primary events and then coupling these with the neutron flux to create a final profile. This is fundamentally more accurate than the hard sphere analysis that is used to derive damage or primary events from programs such as SRIM since the tool also applies quantum mechanics corrections to the profiles thus providing a potentially more accurate result. Details can be found within Ziegler *et al.* (2010); Stoller *et al.* (2013). The primary events are given as primary knock-on atoms (PKA).

Within MCNP a spherical vacuum of radius 10 cm is surrounded by a 2 cm thick tungsten layer which is then further surrounded by a homogeneous mixture of steel and water up until the depth from the centre is 50 cm. The setup is illustrated in Figure 4.1. The entire simulation is constructed using surfaces layered one on top of

another with the surfaces20 µm apart. This is done to provide multiple surfaces to record fluxes on since the aim of this study is to determine the effect of back-scatters on damage in a fusion environment. It should be noted that surface 1 is the first layer of tungsten and surface 20001 is the edge of the steel-water mix. The Figure shows a cross section of this setup with pink indicating tungsten and the blue indicating the homogeneous steel-water mix. The surrounding is a vacuum. 10^7 particles were used which passed all of MCNP checks and also seem to show clear trends within the subsequent results.

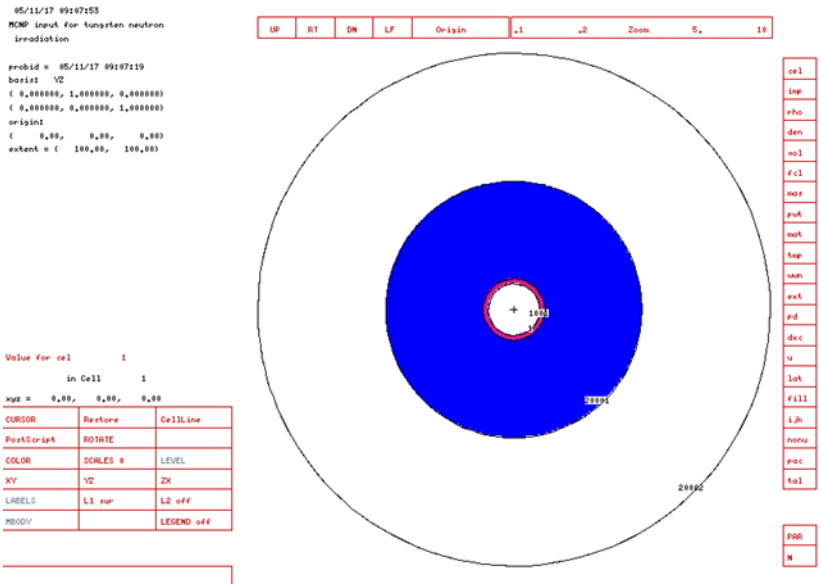

Figure 4.1: Spherical shell setup for simulation of transport of 14 MeV neutrons

The setup involves a point source of neutrons at [0, 0, 0] (which is the centre of the simulation) and then recording the fluxes through each of the surfaces. A total of 174 energy groups between 0 to 14 MeV are used to record the flux. The flux for each individual surface is then passed through Spectra-PKA to get an analysis of the primary events occurring within the solid materials. The aim is to understand the energy of a primary event and its exact location.

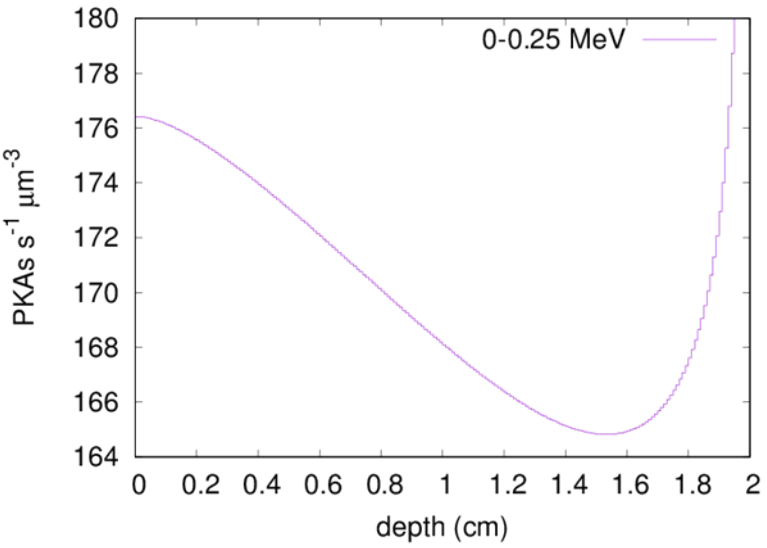

Figure 4.2: PKA profile for spherical shell, courtesy of M. Gilbert (CCFE) using a Spectra-PKA analysis.

4.3 Results

Figure 4.3 shows the overall primary events within the simulation based on the surface number. Two quantities measured are shown: the average PKA energy and the number of PKAs per second. It should be noted that the PKAs are based on 1 neutron per second from the point source and are normalised for area on each of the surfaces.

One of the clearest observations is the sudden spike in the number of primary events corresponding with a sharp decrease in the energy of these. It can be noted that this occurs at the interface of the tungsten and the steel-water mix, the latter behaving mostly as a moderator. This becomes obvious due to the clear decrease in the energy of the primary events. Another observation is there is peak in the number of events within the steel-water mix.

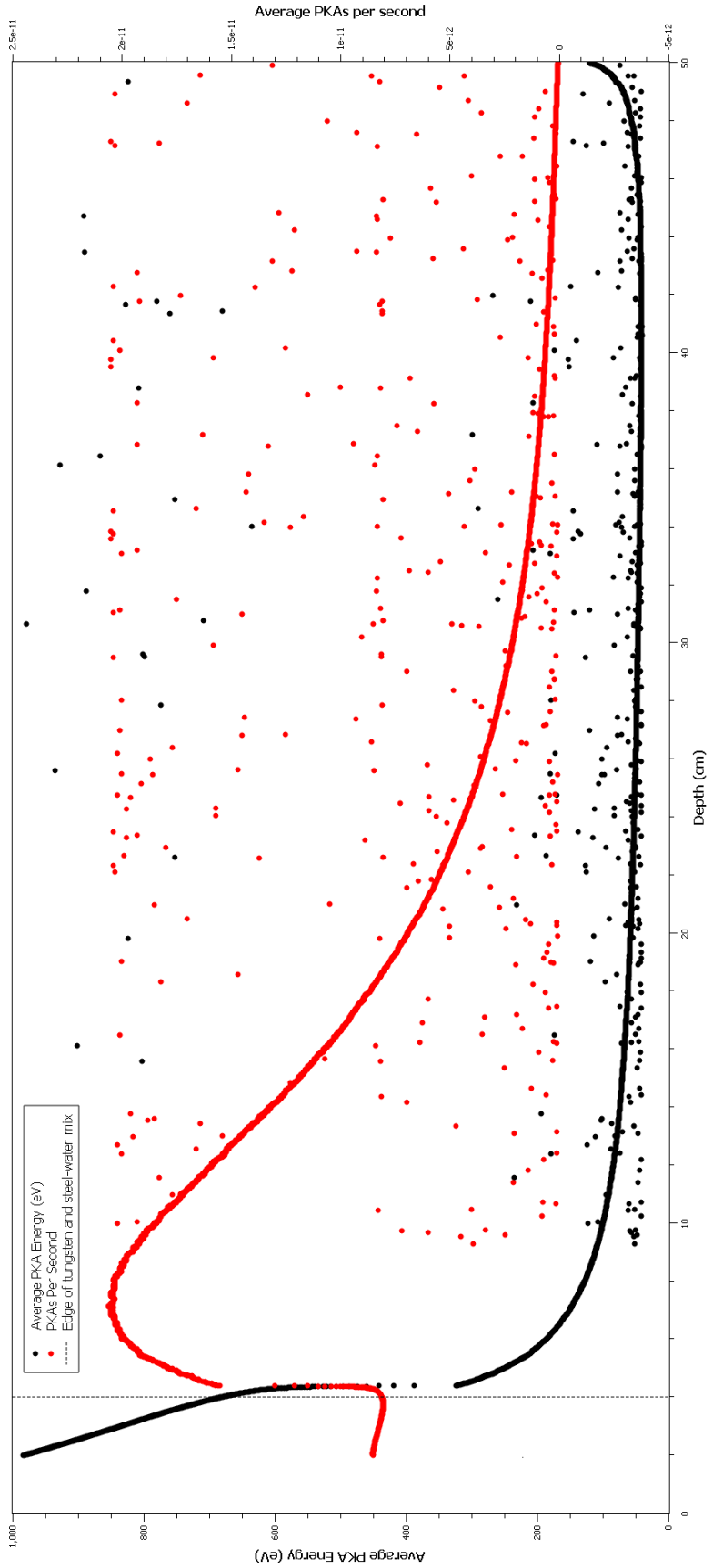

Figure 4.3: Analysis per surface of PKAs

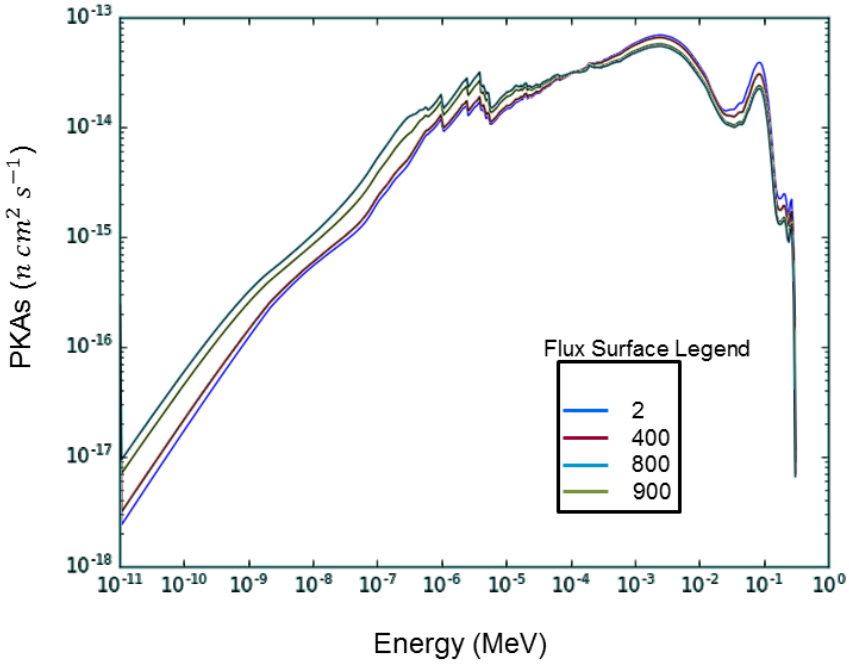

Figure 4.4: PKA flux spectrum for Spectra-PKA in a spherical shell simulation.

Figure 4.4 shows the profile from the primary events within the tungsten shell at various depths given by the surface number of these depths. As one can note, there is a change within the tail or lower energy primary events and a decrease in the higher energy ones as one goes deeper into the tungsten shell. Figure 4.5 shows the comparison of the primary events within the simulation. As one can note, there is a clear difference in the profiles within the moderator and the tungsten shielding. There appears to be fewer higher energy primary knock ons in the moderator although it must be remembered that the difference in materials will result in fundamentally different PKAs. For instance, the maximum energy of a primary knock on that can be achieved by the tungsten is 300 keV.

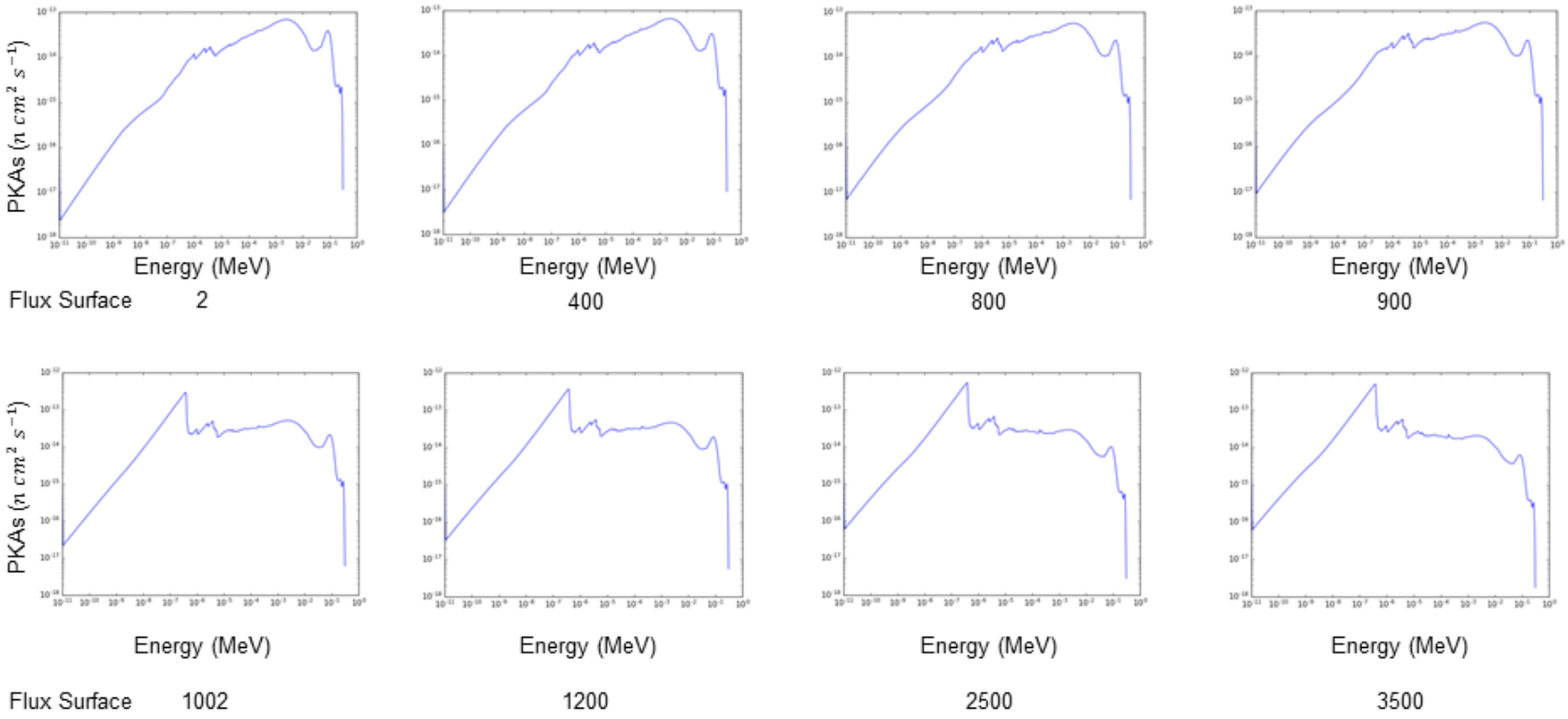

Figure 4.5: Comparison of PKAs at various surfaces of the spherical shell simulation. The row above are PKAs within tungsten, and the ones below within the steel-water moderator.

4.4 Discussion

As can be seen from Figure 4.3, the peak in the number of primary events is similar to the peak as observed in (Hussain et al - in prep, Chapter 3). This suggests that there is some sense that there is likely to be a spike in primary activity within the depth of the material. The possible reason for this could be due to the dropping off of higher energy neutrons which end up being moderated and causing further localised damage (Figure 4.5). However, there is going to be a clear peak in damage consequently in the surface of tungsten due to the back-scatters, the evidence of this can be seen in the number of primary events which tend to gradually decrease and subsequently the high average energy of these primary events.

This has a couple of consequences for the issue of synergistic effects within fusion reactors. Firstly, since we are now in a position to create very specific primary event profiles for the near surface; any experiment which uses ion damage as a proxy to neutron damage can be tailored to create very specific scenarios. Secondly, the issue of damage in the surface is quite likely the result of backscatters rather than the direct events. Therefore, in order to investigate the synergistic effects of plasmas and neutrons, it may not be necessary to have 14 MeV neutrons but sufficient conclusions could be made using fast neutrons.

4.5 Conclusion

As we have demonstrated in this work, we have a clear methodology for obtaining the primary event spectrum through various configurations. It should be noted that the values themselves should be treated cautiously since the simulations are merely "representative". However, they do tend to very clearly highlight the physical effects

that are likely to take place. We have managed to show a clear significance of backscattered neutrons on the damage on the surface and in a fusion reactor as a whole. It would be the aim of future work to delve simulations using Object Kinetic Monte Carlo (OKMC) and Molecular Dynamics (MD) to paint a more specific picture of the surface damage and its implications for the synergistic effects.

Chapter 5

Statistical Description of Primary Events in Tungsten using Molecular Dynamics

5.1 Introduction

Within the fusion community, there is a clear question about the synergistic effect of plasma and neutrons on materials in fusion reactors (Roth *et al.*, 2009; Roth and Schmid, 2011; Watanabe *et al.*, 2011; Markelj *et al.*, 2013b,a, 2014; Tyburska *et al.*, 2009). Currently, there is a trend to use ions as proxy for neutron damage (Abromeit, 1994) since there are no viable 14 MeV neutron sources that can be used to provide comprehensive material testing. However, as previous work has shown (Hussain et al 2017 - in prep, Chapters 3 and 4), there is clear indication that these may not be viable or indeed very careful consideration needs to go into designing such experiments.

This work is subsequently the next stage in investigating the nature of the primary events. It was deemed that molecular dynamics would be the most appropriate method to show cascade evolution from inception to stability. The aim is to build a comprehensive database of cascades and come up with clear statistical parameters for defining displacement cascades. This work is as much a development of method as of specifying quantitative parameters for future design and engineering. Seven directions were chosen (Figure 5.1), which were done considering the symmetry of a BCC lattice. Furthermore, three energies were chosen to demonstrate a suitable range of energy levels of damage. Specifically, these were 3 keV, 10 keV, and 100 keV. Figure 5.2 shows some samples of cascades at various energies and shows how the chosen energies represent onset of features such as branching.

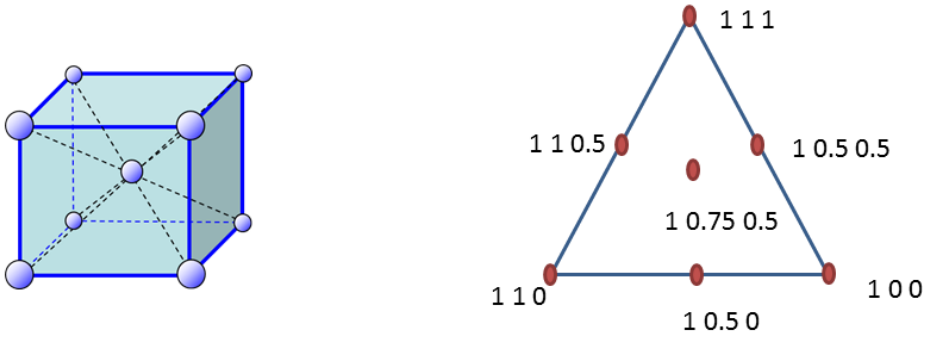

Figure 5.1: BCC lattice and subsequent consideration of symmetry for directions of primary knock ons.

5.2 Methodology

5.2.1 Molecular Dynamic Setup

The molecular dynamics code LAMMPS was used to set up the simulation and OVITO (Stukowski, 2012; Stukowski *et al.*, 2012) to do the visualisations and analysis where a Wigner Sietz analysis was used to identify point defects. The potentials used were of the Embedded Atom Model (EAM) style (Daw *et al.*, 1993), coupled with the ZBL potential for short range interaction (Ziegler *et al.*, 2010), and the two-temperature model (TTM) (Duffy and Rutherford, 2007) where parameters for the model were obtained from (Zarkadoula *et al.*, 2014b). The TTM was included to account for electronic effects within a material. This has been shown to be a good approach for the simulation as shown through the quantum mechanic derivations and comparisons done in the works of Race *et al.* (2010a, 2013).

The simulation was setup to have a single atom defined as the primary knock on within the setup. The simulation was run for 50 picoseconds in multiple stages to improve computational time and simulation accuracy at the same time. The time step is extremely refined at the initial 5 ps, done by estimating the maximum velocity and having the time step cover only ten percent of the lattice parameter. This is generally the displacement stage where a spike of damage exists. A further 10 ps is done at a larger time step representing the recombination stage. Finally the last 35 ps are done at a large time step which represents the final stage of relaxation. The temperature was set at 1000 K for the simulation which would be a realistic expectation for bulk fusion operating temperatures.

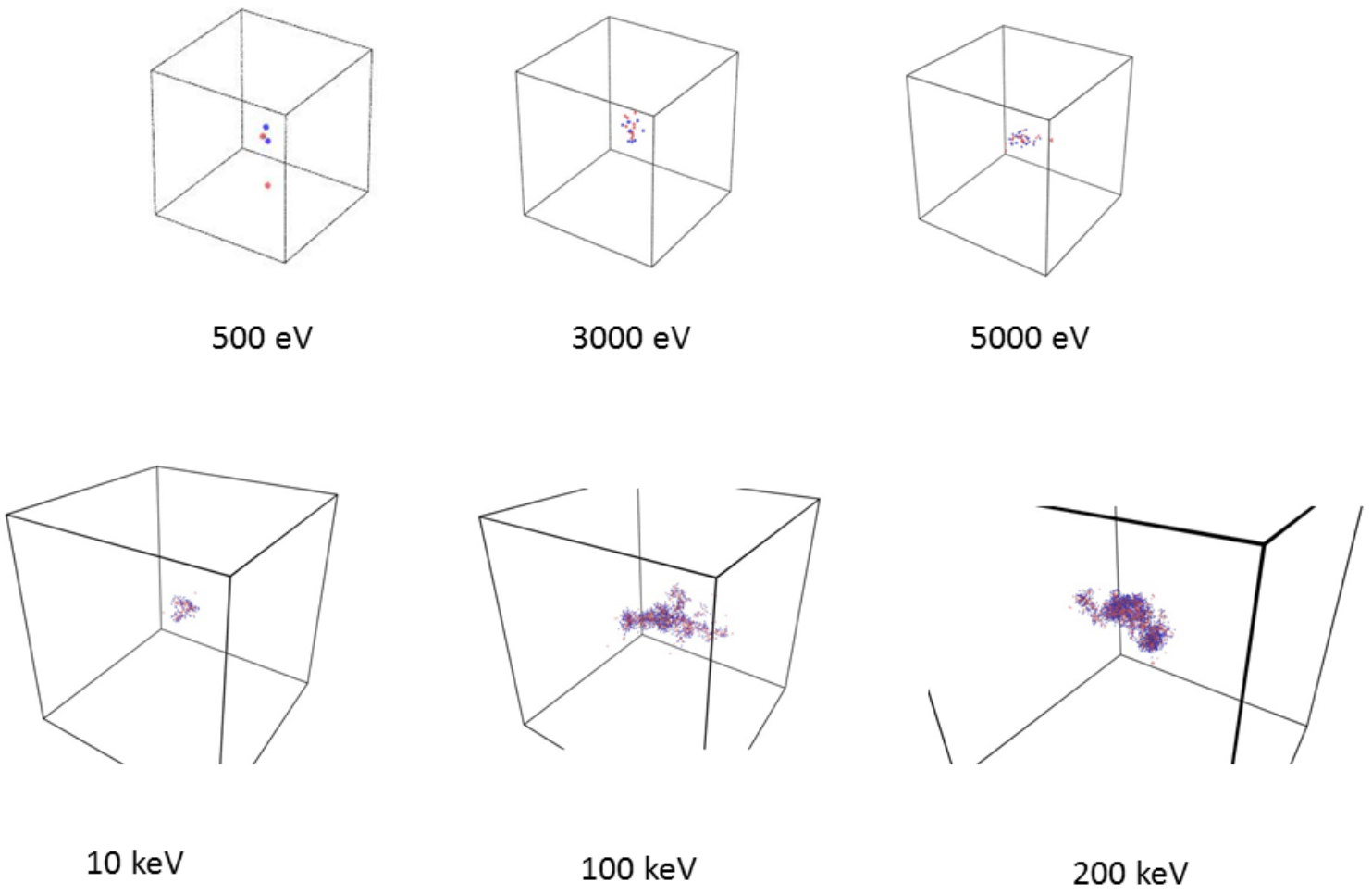

Figure 5.2: Cascades generated as a result of molecular dynamics simulations of tungsten.

5.2.2 Statistical Analysis

In order to create a system whereby the results for the cascades could be standardised, we conducted a statistical analysis on all of the datasets that were generated as a result of the molecular dynamics simulations. The four statistical moments were calculated for all cascades. These (the mean ($\bar{x}$), variance (σ^2), skewness (γ_1), and kurtosis (κ)) are given by the expressions:

$$\bar{x} = \frac{1}{n}\sum_{i=1}^{n} x_i, \tag{5.1}$$

$$\sigma^2 = \frac{1}{n}\sum_{i=1}^{n}(x_i - \bar{x})^2, \tag{5.2}$$

$$\gamma_1 = \frac{1}{n}\sum_{i=1}^{n}(x_i - \bar{x})^3, \tag{5.3}$$

$$\kappa = \frac{1}{n}\sum_{i=1}^{n}(x_i - \bar{x})^4. \tag{5.4}$$

Prior to determining the expressions however, a covariance analysis is conducted and the coordinates are transformed. This is to find the correct axis to find the moments upon. The significance of this can be observed from Figure 5.3. To do this, the eigenvectors of the covariance matrix must be determined (details of this can be found in texts such as Srivastava (2010)). The covariance matrix is given by:

$$\begin{pmatrix} \sigma_{xx} & \sigma_{yx} & \sigma_{zx} \\ \sigma_{xy} & \sigma_{yy} & \sigma_{zy} \\ \sigma_{xz} & \sigma_{yz} & \sigma_{zz} \end{pmatrix}, \tag{5.5}$$

Where:

$$\sigma_{xy} = \frac{1}{n^2} \sum_{i=1}^{n} \sum_{j=1}^{n} \frac{1}{2}(x_i - \bar{x})(y_i - \bar{y}). \tag{5.6}$$

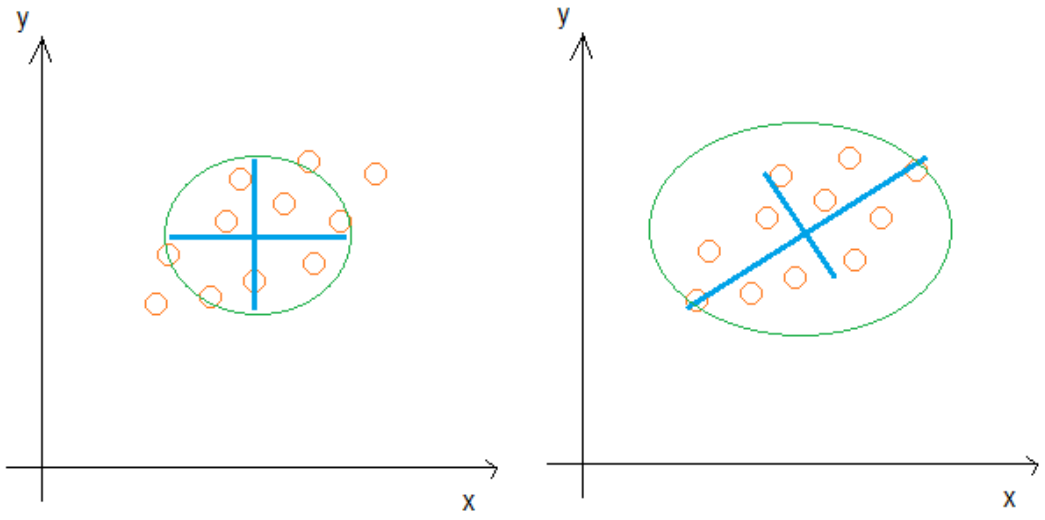

Figure 5.3: Depiction of how the basis for finding the statistical moments can affect the visualization of the cascade shape. Note how the cartesian vectors do not represent the system as well as the eigenvectors.

After this, the quantities are fitted onto a skewed normal curve for visualisation purposes. The probability distribution function and the statistical moments are given by:

$$f(x) = \frac{1}{\omega\pi} e^{\frac{x-\xi}{2\omega^2}} \int_{-\infty}^{\alpha(\frac{x-\xi}{\omega})} e^{\frac{t^2}{2}}.dt\,, \tag{5.7}$$

$$\bar{x} = \xi + \omega\delta\sqrt{\frac{2}{\pi}}, \tag{5.8}$$

$$\sigma^2 = \omega^2(1 - \frac{2\delta^2}{\pi}), \tag{5.9}$$

$$\gamma_1 = \frac{\frac{4-\pi}{2}(\delta\sqrt{\frac{2}{\pi}})^2}{(1 - \frac{2\delta}{\pi})^{\frac{3}{2}}}, \tag{5.10}$$

It should be noted that the skew normal curve cannot depict the kurtosis of a distribution. However, this was found to be the most suitable for depicting the shape of the cascades.

5.3 Comparison of Potentials

For this study, two fundamental potentials were used. Both of these are of the format of Embedded Atom Model (EAM) details of which can be found in works such as Daw *et al.* (1993). One was the Juslin Wirth potential (Juslin and Wirth, 2013), the other was a potential developed at the Culham Centre for Fusion Energy (CCFE) by Daniel Mason (2017 - private communication). The latter potential correctly predicts the instability of a tungsten di-vacancy which was a fundamental finding of work done by Becquart *et al.* (2010). While simulations were conducted with both potentials, analysis was only done for the Mason potential since the Juslin Wirth potential has already been used in a similar study done by Setyawan *et al.* (2015).

5.3.1 Basic Defects

Units = eV	1 1 1 Interstitial	1 1 0 Interstitial	1 0 0 Interstitial	Vacancy Formation
Juslin Wirth Potential	9.517	10.16	Not available/calculated	3.632
Daniel Mason Potential	8.969	9.756	10.0679	3.730
DFT	9.55 (Juslin and Wirth, 2013)	9.84 (Juslin and Wirth, 2013)	Not available/calculated	3.6 Clark *et al.* (2001)

Table 5.1: Fundamental defect energies for the two potentials and comparison to DFT calculations.

As can be observed from table 5.1, the Daniel Mason energy appears to under predict the energy requirements for the formation of defects except in the case of a vacancy. It is unclear what effect this would have since the energies are the fundamental quantities that affect how a potential is fitted. A remarkable difference is observed in the displacements produced as is shown.

5.3.2 Displacements

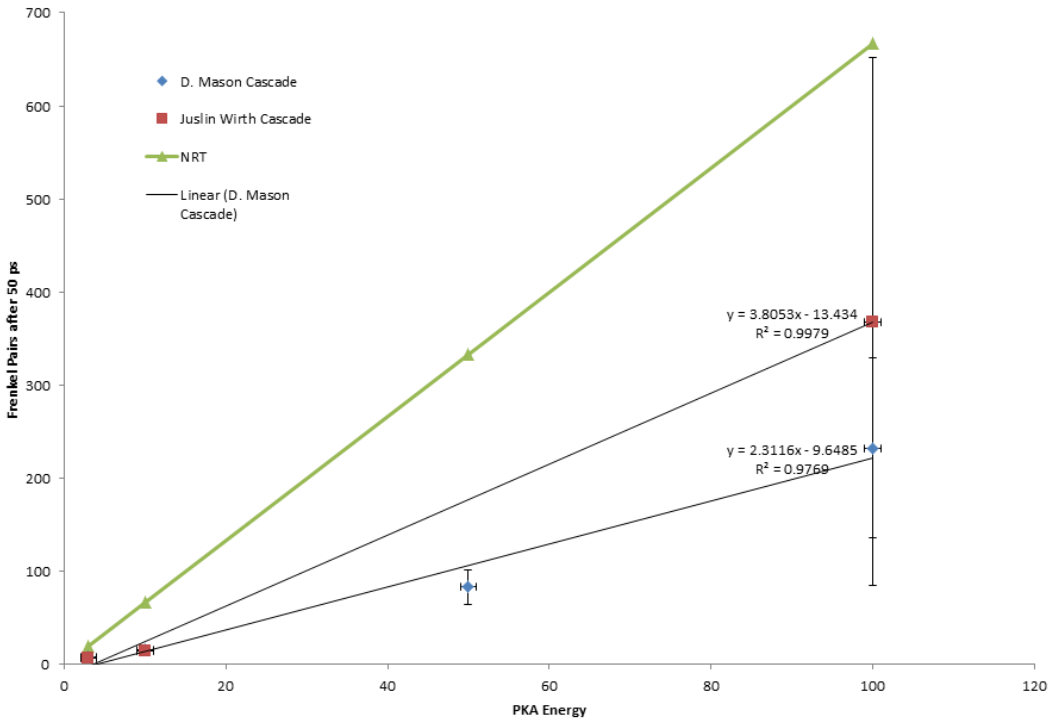

Figure 5.4: Comparison of defects produced in simulations using the two EAM potentials.

As Figure 5.4 demonstrates, both potentials fundamentally show that the displacements are far less than what is predicted by the NRT model (Stoller and Greenwood, 2001; Ziegler *et al.*, 2010). The NRT model is an empirical model of the number

of defects produced. This is important since the NRT is now fundamentally recognised as a upper limit to the number of displacements. What the MD simulations however also show (since the results were plotted 50 picoseconds after initiation) is that there is a relaxation healing process. This should be noted when engineering nuclear materials since materials are likely to heal further over longer timescales.

5.4 Statistical Overview of Displacement Cascades

Figure 11 depicts all the cascades as visualised using the skewed normal distribution. Table 5.3 specifies the exact numbers that were obtained. As can be clearly seen, there is evidence of electronic effects causing spreading of defects. There is also evidence of the electronic effects resulting in larger distances for the centre of mass of the defects. These are expected observations based on materials theory. What is not observed is a remarkable difference of the distance of centre of mass at high index directions. This warrants further investigation since it is generally considered that low index directions (ones where the unit vector of the direction is smaller), due to the presence of molecules directly and close in the path of the projectile, result in much higher damage. At higher energies however, there is clearly less spread and more focussed damage indicating that the electronic effects do dampen the projectile significantly before it causes damage. Generally the shapes appear to be spherical with few exceptions. The shapes appear to be so due to the overlapping of the resulting skew normal curves (Appendix A).

			x			y			z				
Sim	Energy	Direction	Mean	Variance	Skew	Mean	Variance	Skew	Mean	Variance	Skew		Distance
0	3 keV	1 1 1	6.75	2.23	-0.71	7.65	28.45	0.07	5.66	12.29	-0.03		11.67
1	3 keV	1 1 0	10.07	89.05	-0.68	9.39	20.93	-0.71	-0.79	28.92	-0.55		13.79
2	3 keV	1 0 0	11.97	22.47	0.08	1.71	44.74	-0.69	1.88	25.24	0.44		12.23
3	3 keV	1 1 0.5	4.45	7.55	0.02	6.21	2.66	0.70	2.73	2.79	-0.68		8.12
4	3 keV	1 0.5 0	16.29	84.67	-0.65	9.74	75.63	0.29	-1.66	66.03	-0.68		19.06
5	3 keV	1 0.5 0.5	7.47	52.56	0.06	3.84	7.22	-0.17	2.96	17.27	0.51		8.90
6	3 keV	1 0.75 0.5	14.42	81.92	0.16	7.17	76.53	-0.15	1.74	7.65	0.43		16.20
7	3 keV	1 0.875 0.5	7.72	8.18	0.38	5.69	10.34	-0.54	1.79	24.01	-0.51		9.76
8	3 keV	1 0.625 0.5	8.76	29.40	0.29	6.43	7.32	-0.59	4.03	14.05	0.67		11.59
9	3 keV	1 0.625 0.25	10.75	43.82	0.54	10.05	107.48	0.29	0.90	58.33	-0.18		14.75
10	10 keV	1 1 1	19.53	201.64	-0.11	2.41	127.94	-0.66	16.97	161.78	-0.67		25.98
11	10 keV	1 1 0	15.96	19.25	-0.57	11.45	81.06	-0.71	0.91	65.47	0.66		19.66
12	10 keV	1 0 0	13.35	148.92	0.69	-4.18	144.31	0.68	1.99	155.43	-0.27		14.13
13	10 keV	1 1 0.5	9.74	12.21	-0.27	11.09	78.49	0.07	2.40	62.19	0.36		14.96
14	10 keV	1 0.5 0	17.76	287.73	-0.28	7.61	279.97	-0.63	-4.77	241.54	-0.01		19.90
15	10 keV	1 0.5 0.5	9.34	62.11	0.39	4.31	15.48	0.68	4.36	21.18	0.71		11.17
16	10 keV	1 0.75 0.5	14.44	64.86	0.49	6.04	82.80	0.18	3.21	407.85	0.69		15.98
17	10 keV	1 0.875 0.5	13.42	62.24	-0.38	8.19	68.51	0.64	4.95	32.83	-0.22		16.48
18	10 keV	1 0.625 0.5	23.86	9.18	0.39	14.84	603.64	0.06	0.07	726.66	-0.53		28.10
19	10 keV	1 0.625 0.25	23.47	548.33	0.62	5.98	446.11	0.42	6.76	572.93	0.47		25.14
20	100 keV	1 1 1	19.18	339.69	0.37	31.78	1563.01	0.70	22.44	775.00	0.65		43.38
21	100 keV	1 1 0	55.66	18918.52	0.66	-26.70	17731.24	0.66	-55.78	16947.28	0.65		83.20
22	100 keV	1 0 0	96.61	8173.76	-0.70	11.66	8044.15	-0.70	18.48	5193.73	-0.67		99.05
23	100 keV	1 1 0.5	-0.43	23858.66	0.71	-13.55	11708.96	0.41	59.19	13458.85	0.69		60.73
24	100 keV	1 0.5 0	84.31	8820.68	-0.52	50.43	9089.44	-0.52	12.39	9435.71	-0.47		99.02
25	100 keV	1 0.5 0.5	60.50	42.64	0.70	23.75	15.53	0.14	23.38	68.73	0.19		69.07
26	100 keV	1 0.75 0.5	83.18	4.16	-0.54	68.89	4.50	0.69	49.64	298.56	-0.02		118.86
27	100 keV	1 0.875 0.5	83.68	17.56	0.69	81.09	29.49	0.70	62.22	141.02	-0.69		132.09
28	100 keV	1 0.625 0.5	-18.68	8550.33	-0.66	104.08	8116.95	-0.67	47.46	7863.57	-0.66		115.91
29	100 keV	1 0.625 0.25	118.66	848.45	-0.64	68.47	412.46	-0.21	19.84	305.68	0.11		138.42

Table 5.3: Tabulated statistics from simulations done for primary knock on cascades formed in tungsten using the D Mason potential.

5.5 Conclusion

As far as the molecular dynamics investigation of the cascades goes, there were three main focuses:

1. The shape of cascades,
2. The variance of displacements with direction,
3. Building a database for the characterisation of primary events.

Within the shape, it would appear for lower energies (up to 10 keV), one could characterise that a spherical container with random particles should be appropriate since these strongly appear to have a speherical shape. This we infer from the overlapping nature of the curves which is clearer in Appendix A. Indeed work done by De Backer *et al.* (2016) shows that there is no significant difference when using various random distributions close by for lower energy. For higher energies however, the directions will need to be taken into account and therefore there will need to be appropriate representation of secondary events or directions a projectile can take. Whether these would appropriately represented using statistical averages is an investigation for Object Kinetic Monte Carlo (OKMC) methods since they build to the appropriate length and time scales. It should be noted that the resolving of divacancies seems to have resulted in lowering the number of displacements in the D Mason potential. This may however simply be a result of the increased energy required to form defects and therefore may need re-fitting to ensure appropriate results.

Part II

Relaxation and Merger of Plasma Magnetic Flux Ropes

Chapter 6

Introduction and Literature Review

6.1 Basic Plasma Theory

6.1.1 Kinetic description of plasma

Assuming we are dealing with a region that consists of charged particles and nothing else, we are in a position to completely define the material of interest using charged particle physics. This can be described by the following equations (Feynman *et al.*, 1963):

Maxwell's equations

$$\nabla . \boldsymbol{E} = \frac{\boldsymbol{\rho}}{\epsilon_0}, \tag{6.1}$$

$$\nabla \times \boldsymbol{E} = -\frac{\partial \boldsymbol{B}}{\partial t}, \tag{6.2}$$

$$\nabla . \boldsymbol{B} = 0, \tag{6.3}$$

$$c^2 \nabla \times \boldsymbol{B} = \frac{j}{\epsilon_0} + \frac{\partial \boldsymbol{E}}{\partial t}, \tag{6.4}$$

Charge conservation

$$\nabla . j = -\frac{\partial \rho}{\partial t}, \tag{6.5}$$

Lorentz force

$$\boldsymbol{F} = q(\boldsymbol{E} + \boldsymbol{v} \times \boldsymbol{B}), \tag{6.6}$$

Motion

$$\boldsymbol{F} = \frac{d(m\boldsymbol{v})}{dt}, \tag{6.7}$$

Where ∇ is the gradient operator, E is the electric field, ρ is the charge density, ϵ_0 is the permittivity of free space, B is the magnetic field, t is time, c^2 is the speed of light squared, j is the current, F is the force on the particle, q is the charge of the particle, v is the velocity of the particle, and m_i is the mass of the species.

In order to completely model a plasma, individual particles are resolved using equations . This is referred to as the kinetic description of plasma. This is quite cumbersome since plasmas are expected to have 10^{23} particles (Aymar, 2001) which is currently computationally prohibitive even with assumptions. If one is only concerned with the steady-state situation, one may use a Monte Carlo approach in order to obtain quantities such as particle fluxes on the wall etc. This too however may be prohibitive in a fusion environment to gain statistical significance with a myriad of varying behaviours.

6.1.2 Fluid description of plasma (MHD)

In order to be able to make plasma analysis approachable, a common approach is to treat plasma as a continuum. This is typically referred to as the fluid description of plasma or magnetohydrodynamics (MHD). This form shall now be concisely derived based on typical approaches which can be found in textbooks such as Hazeltine and Waelbroeck, 1998.

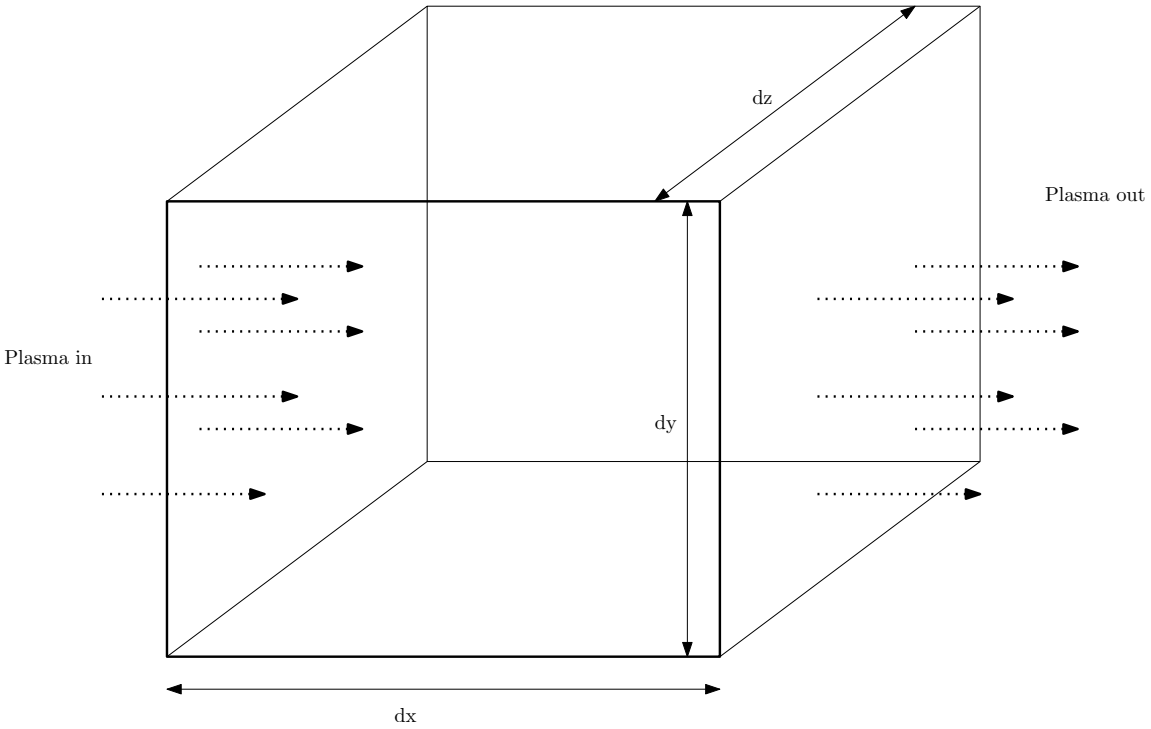

Figure 6.1: Unit volume for plasma flow

Figure 6.1 shows an infinitesimal volume which we shall use to consider our flow of plasma. We shall consider a single species for the derivation (either ions or electrons). These can later be coupled by considering either a collisionless plasma or collision and subsequent neutralisation. Treating as a continuum, we define our particles using a distribution function.

$$d\boldsymbol{n} = \boldsymbol{f}(x, v, t).d\boldsymbol{v}, \tag{6.8}$$

Where $\boldsymbol{n}$ is a small section of particles, $\boldsymbol{f}$ is the distribution function in terms of $\boldsymbol{x}$ (position), $\boldsymbol{v}$ (velocity) and t (time). We shall be working in the velocity phase space.

We can expect a change in the distribution based upon collisions within the volume. We shall disregard other sources for the moment.

$$\frac{d\boldsymbol{f}}{dt} = C(\boldsymbol{f}), \tag{6.9}$$

C is the collision function which is a function of the distribution function. Expanding the differential using the chain rule:

$$\frac{d\boldsymbol{f}}{dt} = \frac{\partial \boldsymbol{f}}{\partial t} + \frac{\partial \boldsymbol{f}}{\partial x_i}\frac{\partial x_i}{\partial t} + \frac{\partial \boldsymbol{f}}{\partial v_{x_i}}\frac{\partial v_{x_i}}{\partial t} = \frac{\partial \boldsymbol{f}}{\partial t} + \boldsymbol{v}.\nabla \boldsymbol{f} + \frac{\partial \boldsymbol{v}}{\partial t}\nabla_v \boldsymbol{f} = C(\boldsymbol{f}). \tag{6.10}$$

Equation 6.10 is also known as the Vlasov equation and relates the change in distribution to collisions within the plasma. We shall now assume a collision-less plasma. Noting that $\boldsymbol{v}.\nabla \boldsymbol{f} = \nabla(\boldsymbol{f}\boldsymbol{v}) - \boldsymbol{f}.\nabla \boldsymbol{v}$, $\nabla \boldsymbol{v} = 0$, $\int \boldsymbol{f}.d^3v = n$, $\boldsymbol{n}\boldsymbol{u} = \int \boldsymbol{v}\boldsymbol{f}.d^3\boldsymbol{v}$ and $\frac{d\boldsymbol{v}}{dt} = \boldsymbol{a} = \frac{\boldsymbol{F}}{m}$ where $\boldsymbol{F}$ is force, m is mass, $\boldsymbol{u}$ is the fluid velocity (as opposed to the particle velocity) and $\boldsymbol{a}$ is acceleration; we integrate the collision-less Vlasov equation over the velocity phase:

$$\frac{\partial n}{\partial t} + \nabla n\boldsymbol{u} + \frac{1}{m}\int \boldsymbol{F}\frac{\partial \boldsymbol{f}}{\partial \boldsymbol{v}}.d^3\boldsymbol{v} = 0. \tag{6.11}$$

Based on integration by parts: $\frac{1}{m}\int \boldsymbol{F}\frac{\partial \boldsymbol{f}}{\partial \boldsymbol{v}}.d^3\boldsymbol{v} = \frac{1}{m}[\boldsymbol{F}\boldsymbol{f}]_{-V_\infty}^{V_\infty} - \int f\frac{d\boldsymbol{F}}{d\boldsymbol{v}}.d^3\boldsymbol{v} = 0$ by

stating that there are going to be no particles at the extreme end of the velocity spectrum and a similar approach with the second term. Therefore we have:

$$\frac{\partial n}{\partial t} + \nabla n\boldsymbol{u} = 0. \tag{6.12}$$

This can be recognised as the continuity equation.

Integrating over an entire volume we obtain:

$$\frac{\partial N}{\partial t} + \int \nabla n\boldsymbol{u}.dV = Source. \tag{6.13}$$

Here we could possibly modify the collision function and use it as source (negative sink) to account for a collisional plasma.

To obtain the force momentum balance, we consider the control volume illu

$$\frac{\partial}{\partial t}(\rho) = \nabla.(\rho v) - P\nabla.v + \eta j^2 + Q_{visc} \tag{6.14}$$

strated in Figure 6.1. Relative velocity (the difference between the fluid and particle velocity$u - v$) is used to determine the momentum change. Using the principle of Newton's rate of change of momentum is the force on the body:

$$\frac{d\boldsymbol{p}}{dt} = \frac{\partial mn\boldsymbol{u}}{\partial t} + \nabla \int m(\boldsymbol{u} - \boldsymbol{v})(\boldsymbol{u} - \boldsymbol{v})\boldsymbol{f}.d^3\boldsymbol{v} = \boldsymbol{F}, \tag{6.15}$$

$$m(\boldsymbol{u}\frac{\partial n}{\partial t} + n\frac{\partial \boldsymbol{u}}{\partial t}) + m\nabla \int (\boldsymbol{uu} - \boldsymbol{uv} - \boldsymbol{vu} + \boldsymbol{vv})\boldsymbol{f}.d^3\boldsymbol{v} = \boldsymbol{F}. \tag{6.16}$$

The products $\boldsymbol{uv}$ and $\boldsymbol{vu}$ integrate to zero. We define the pressure tensor:

$$\boldsymbol{P} = m. \int \boldsymbol{vvf}.d^3\boldsymbol{v}, \tag{6.17}$$

And the force due to Lorentz force (equation 6.6). We obtain:

$$m(\boldsymbol{u}\frac{\partial n}{\partial t} + n\frac{\partial \boldsymbol{u}}{\partial t}) + m\nabla \boldsymbol{u}\boldsymbol{u}n = -\nabla \boldsymbol{P} + nq(\boldsymbol{E} + \boldsymbol{u} \times \boldsymbol{B}), \tag{6.18}$$

$$m(\boldsymbol{u}\frac{\partial n}{\partial t} + n\frac{\partial \boldsymbol{u}}{\partial t}) + mn\boldsymbol{u}\nabla \boldsymbol{u} + m\boldsymbol{u}\nabla n\boldsymbol{u} = -\nabla \boldsymbol{P} + nq(\boldsymbol{E} + \boldsymbol{u} \times \boldsymbol{B}), \tag{6.19}$$

Subtracting the product of $m\boldsymbol{u}$ and the continuity equation (equation 6.12):

$$m(\boldsymbol{u}\frac{\partial n}{\partial t} + n\frac{\partial \boldsymbol{u}}{\partial t}) + mn\boldsymbol{u}\nabla \boldsymbol{u} + m\boldsymbol{u}\nabla n\boldsymbol{u} - m\boldsymbol{u}\frac{\partial n}{\partial t} - m\boldsymbol{u}\nabla n\boldsymbol{u} = -\nabla \boldsymbol{P} + nq(\boldsymbol{E} + \boldsymbol{u} \times \boldsymbol{B}), \tag{6.20}$$

$$mn(\frac{\partial \boldsymbol{u}}{\partial t} + \boldsymbol{u}\nabla \boldsymbol{u}) = -\nabla \boldsymbol{P} + nq(\boldsymbol{E} + \boldsymbol{u} \times \boldsymbol{B}). \tag{6.21}$$

The fluid equations which are basically equations 6.12 and 6.21 can now be used for a variety of purposes. They can be used for general plasma flows by fixing n as the overall plasma or solved individually for various ion species and electrons. Therefore, for a D-T plasma, we would have six equations plus the Maxwell equations along with a criterion to provide closure to the problem. While this is tedious it is still significantly less intensive than solving the full kinetic description for all particles in the system.

Furthermore, now that we have both the kinetic and fluid descriptors for plasma, we

can move on to examine the effects we expect within a fusion environment. Plasma particles move along field lines.

6.2 Magnetic Reconnection

Magnetic reconnection is a phenomenon that is observed in both laboratory and astrophysical plasmas. Magnetic reconnection occurs when oppositely directed fields are pushed together in a highly conductive plasma. It may also occur if oppositely directed fields simply occur in a plane (2D) rather than actual 3D topologies being oppositely directed. This causes a localised breaking of the frozen in condition, resulting in a change in the magnetic topology. This in turn results in the conversion of magnetic energy, into kinetic and thermal energy on timescales faster than the global resistive diffusion. Within the corona the phenomenon has been proposed to involve twisted magnetic field lines that then relax into a minimum energy state (Taylor, 1974, 1986; Priest and Forbes, 2000; Bhattacharjee, 2004; Schnack, 2009; Zweibel and Yamada, 2009; Yamada *et al.*, 2010).

Magnetic field lines are generally moving through the fluid and can then twist and combine with other field lines which is what results in field lines that are twisted. This process has been observed in astrophysical plasmas and is referred to as stressing (Klimchuk, 2015). Magnetic reconnection in laboratory plasmas (i.e Tokamaks) is a result of forced merging compression experiments. In this scenario, two toroidal flux tubes are formed which are then bought together. When the two meet and twist they then relax into a minimum energy state. The benefit of this is in the observation that the energy that is released as a result of the process heats up the plasma. As such the amount allows attainment of ion temperatures up to 1 keV (Ono *et al.*, 2011). Furthermore, heat losses are minimised (possibly through the short

timescales and the large spatial distribution of reconnection) which allows efficient heating of plasma (the fundamental aim Tokamak plasmas is to be hot enough to achieve nuclear fusion) .

6.2.1 Sweet Parker Reconnection and Current Sheet Parameters

Many details of magnetic reconnection are still unclear. However, it has been shown through numerical studies that there is often the formation of a Sweet Parker current sheet before the topological reorientation of connecting flux ropes into one (Biskamp, 1984, 1997) which appear to follow particular scaling laws. Within a reconnection event, it may be described using the Equation $< u >=< E_z >< v_A >$ where u is the upstream velocity, E_z is the reconnection rate and v_A is the Alfven velocity. The resistivity of the plasma affects the behaviour of the current sheet. This is understood by considering that $u_\infty B_\infty = \eta j_m = c$ where u_∞andB_∞ indicate the upstream values of the velocity and magnetic field, η is the resistivity and j_m is the current density at the x point (Figure 6.2) and c is a constant.

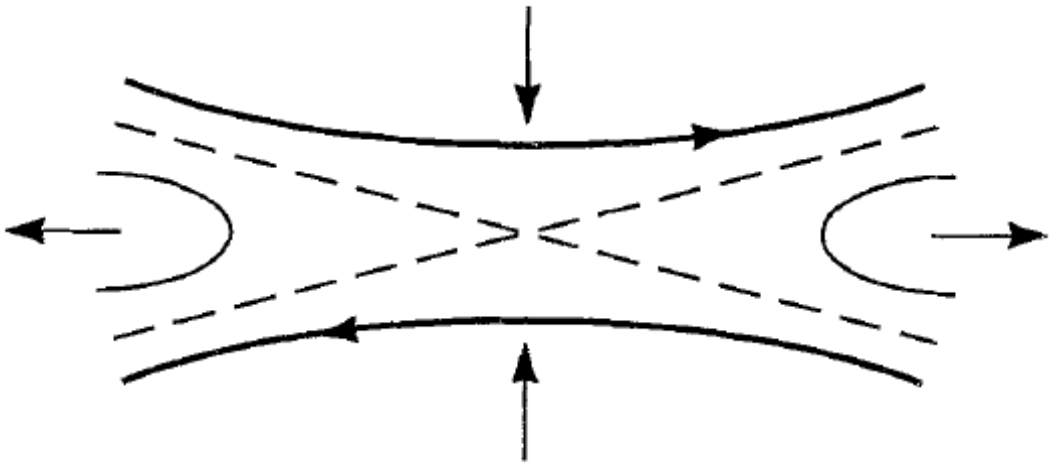

Figure 6.2: Diagram of Magnetic Reconnection
Source: Biskamp

Setting that $B \propto \eta^{-v}$ right in front of the diffusion layer (where v is some constant):

$$B = j_m \delta, \tag{6.22}$$

$$=> \delta = \eta^{(1-v)}, \tag{6.23}$$

Where δ is the current layer thickness and then considering the length of the current sheet (Δ) from Ohm's law and mass conservation:

$$\Delta = \frac{B\delta^2}{\eta} \propto \eta^{(1-3v)}. \tag{6.24}$$

Computations find that $v = \frac{2}{3}$. This suggests that the reconnection reaches the system size very quickly at which point it is independent of the resistivity (Parker, 1957; Biskamp, 1984, 1997)

6.2.2 Hyper-Resistivity

Fluid modelling of merging compression has found that if simple ohmic resistivity is considered, then the reconnection event takes longer with oscillatory motion within the approaching flux tubes observed (Browning *et al.*, 2014, 2015). A correction to this is to use the Hall MHD equations which is also included in the work of Stanier *et al.* (2013) discussed later. These include an additional resistivity term of $\eta_H(\nabla^2 J)$ which can be interpreted as an electron viscosity term.

An alternate explanation is that it could be a term represented as fluctuating mean magnetic field – which is the premise of the Boozer (1986) generalized Ohm's law derivation. This is further supported by the Equationtion of Hall MHD Stanier *et al.* (2015) which includes η_H through:

$$\partial_t \boldsymbol{B} + \nabla \times (\boldsymbol{B} \times \boldsymbol{V}_e) = -\eta \nabla \times (\nabla \times \boldsymbol{B}) + \eta_H \nabla \times (\nabla \times \nabla^2 \boldsymbol{B}). \tag{6.25}$$

Hyper resistivity reduces the oscillatory behaviour. Due to the uncertain physics of hyper resistivity, Browning *et al.* (2014) conducted parameter scans which tended to show a more realistic reconnection timescale as well.

6.2.3 Constant Rate of Reconnection

In the presence of high guide field and hyper resistivity – a key result was that of a normalised reconnection rate being independent of size of the system simulated (i.e. the length of the flux tubes merged) (Stanier *et al.*, 2015). The rate was also found to be of a similar value when considering either fast dispersive waves (Larmour radius much greater than ion skin depth) or without these (ion skin depth much greater than Larmour radius). There was more variation to be found with the later

however the former gave a constant rate of 0.15. The normalised reconnection rate was defined as:

$$< E_z^* >= \frac{1}{T}[\frac{1}{(\hat{x}.\boldsymbol{v_a})(\hat{x}.\boldsymbol{B})}\frac{\partial \psi_r}{\partial t}], \tag{6.26}$$

where E_z is the reconnection rate, T is the temperature, v_a is the Alfven speed, B is the magnetic field, and $\frac{\partial \psi_r}{\partial t}$ is the rate of change of flux.

6.2.4 Plasma Heating in Merging Plasmas: Experimental Results

A study conducted by Ono *et al.* (2011) investigated the temperature of species following a magnetic reconnection event. This was conducted in Tokamaks TS-3/TS-4 ($R = 20$ cm and 50 cm,$n = 5 * 10^{19}$, $B = 0.05T$) with the distinction being that there was no guide field. The resultant event raised the ion temperature from 10 eV to up to 200 eV, giving a release of 230 J of magnetic energy (80% of energy went into heating). Another study conducted by Inomoto *et al.* (2015) in the UTST Tokamak was done with a centre field solenoid (i.e. no toroidal field and no guide field). Here in conclusion they found two fundamental results of their reconnection experiments. Firstly they plotted initial magnetic energy (which seems to lie near to be equal to $0.11I_P^2$ where I_P is the poloidal current) compared to the released magnetic energy. The magnetic energy released seems to be equal to $0.033I_P^2$ which seems to indicate that 30% of energy is released (which would subsequently heat plasma). In this situation (where the reconnection was within 30μs), it is found that the ion and electron temperatures are quite heavily scattered.

In order to comment on the variation in electron and ion heating due to guide fields (or lack thereof) Inoue *et al.* (2014) conducted a 2D PIC (particles in cell)

simulation of the reconnection region. This allowed a simulation with and without a guide field and examine the effects. The simulations were conducted in general terms rather than for specific conditions therefore allowing the commentary to be more comparative in nature (Stanier *et al.*, 2012, 2013, 2015). Initially without commenting on the distribution; the results suggest that with a guide field there was a near complete dissipation of poloidal field energy flux with the gains going towards the plasma energy (approximately 55%), plasma acceleration (10%) and the toroidal magnetic energy flux (30%). Whereas the no guide field condition saw a loss of nearly 80% poloidal energy flux of which mostly all energised the plasma. This subsequently led to an investigation on how the species were specifically heated. With a guide field, the distribution of energy between ions and electrons is approximately 2:1. The contribution to ion enthalpy is only 1/3, the rest in involved in ion acceleration. The authors argue that the guide field results in a field aligned electron current along the seperatrix which then in turn generates an out of field magnetic flux. There is the suppression of non-linear ion dynamics due which results in lower enthalpy gain than without a guide field. The increased energy for ions in zero guide field is also argued due to the existence of an electrostatic potential which results in ionic acceleration. This potential diminishes as a guide field is introduced. Also, it is argued that a guide field electronically traps electrons close to the sepearatrix. This is demonstrated by the fact that the particles demonstrate increased enthalpy and energy close to the seperatrix in the presence of a guide field while without one there is a broader spatial distribution.

6.3 Relaxation and Helicity Conservation

In work conducted on reverse field pinch (RFP) plasma experiments (Taylor, 1974, 1986), it was proposed that a plasma flux rope approaches a largely stable con-

figuration after achieving a minimum energy state. The dimensionless energy of a magnetic field is defined as:

$$E = \frac{1}{2}\int_V \boldsymbol{B}^2 dV, \tag{6.27}$$

where $\boldsymbol{B}$ is the magnetic field integrated over the volume (V)Taylor relaxation theory (Taylor, 1974, 1986) begins by proposing that a stable plasma having undergone transition does so by achieving a minimum energy state with the constraint that the helicity and axial flux is conserved which are defined as:

$$K = \int_V \boldsymbol{A}.\boldsymbol{B}\, dV, \tag{6.28}$$

$$\nabla \times \boldsymbol{A} = \boldsymbol{B}, \tag{6.29}$$

$$\Psi = \int_S B_z dS, \tag{6.30}$$

where K is the helicity, Ψ is the axial flux, and $\boldsymbol{A}$ is the magnetic potential. Helicity can be visualised as streamlines within a fluid flow remaining constant. Magnetic helicity, specifically, quantifies linkage and topology in a flux rope. While flux conservation can generally be accepted as true in a closed system, the matter of helicity conservation is a little more involved. The matter is fully explored in the work of Finn and Antonsen Jr. (1985). The minimum energy state is then given by $\nabla \times \boldsymbol{B} = \alpha \boldsymbol{B}$ where α is a constant and related to current by $\alpha = \mu_0 \frac{\boldsymbol{j}.\boldsymbol{B}}{\boldsymbol{B^2}}$ (where $\boldsymbol{j}$ is the current vector), and the solution of which is of the form of a Bessel function:

$$B_r = 0, \tag{6.31}$$

$$B_\theta = B_1 J_1(\alpha r), \tag{6.32}$$

$$B_z = B_1 J_0(\alpha r), \tag{6.33}$$

J_0 and J_1 are the zeroth and the first Bessel functions of the first kind. The α parameter is given by the invariance of helicity and axial flux in a flux rope of radius a.

$$\frac{K}{\Psi^2} = \frac{l}{2\pi a}[\frac{\alpha a[J_0^2(\alpha a) + J_1^2(\alpha a)] - 2J_0(\alpha a)J_1(\alpha a)}{J_1^2(\alpha a)}]. \tag{6.34}$$

There have been works which have frequently shown that Taylor relaxation is a good approximation for the energy released during the relaxation of a flux rope. Works that show this include Bareford *et al.* (2013); Dahlburg *et al.* (1988).

6.4 Hydrodynamic and Plasma Stability

Hydrodynamic stability deals with issues of stability within fluid like systems that can resolved using the Navier Stokes equations (or similar). A good review of general fluid stability can be found in texts such as Drazin and Reid (2004). As such the

fundamental equations are given by,

$$\frac{D(\rho \mathbf{u})}{Dt} = 0, \tag{6.35}$$

$$\rho \frac{\partial \mathbf{u}}{\partial t} + \rho \mathbf{u} \nabla . \mathbf{u} = \mathbf{F}, \tag{6.36}$$

where $\mathbf{u}$ is the velocity of the fluid, ρ the density, t time, and $\mathbf{F}$ is any force acting on the system. Equation 6.35 reduces to $\nabla \mathbf{u} = 0$ when the fluid is considered to be incompressible. The forces typically consist of solid body forces, viscous forces, and pressure forces.

Within a plasma system, the typical Navier Stokes equations must be extended to account for the fact that the species in a plasma are charged, and therefore subject to electromagnetic forces. These are taken into account in the force term of the Navier Stokes equations. However, due to the additional terms, the system requires extension in the form of Maxwell's equations to provide closure. These equations are referred to as the Magnetohydrodynamics (MHD) equations. A form of these is given by,

$$\frac{\partial \rho}{\partial t} + \nabla . (\rho) = 0, \tag{6.37}$$

$$\rho \frac{\partial \mathbf{u}}{\partial t} + \rho \mathbf{u} \nabla . \mathbf{u} = -\nabla p + j \times \mathbf{B} + \rho g, \tag{6.38}$$

$$\frac{\partial \mathbf{B}}{\partial t} = \nabla \times (\mathbf{u} \times \mathbf{B}), \tag{6.39}$$

$$\mathbf{j} = \frac{1}{\mu} \nabla \times \mathbf{B}, \tag{6.40}$$

$$\nabla . \mathbf{B} = 0, \tag{6.41}$$

where $\mathbf{B}$ is the magnetic field vector, $\mathbf{j}$ is the current vector, and μ is the permeability. Derivations for these can be found in texts such as Priest (2014).

Within fluid stability there are fundamentally two approaches to dealing with the

mathematical Equationtion: linear or non-linear. Both approaches commence by defining a perturbation to the system (such as fluid velocity, $u = u_0 + u_1$ where u_0 is the undisturbed velocity and u_1 the perturbation). Linear methods involve looking at the stability threshold under small perturbations whereas non-linear systems are more concerned with the direction a system would move towards under arbitrary disturbances. Full descriptions of stability analysis can be found within texts such as Drazin and Reid (2004), Priest (2014), Wesson (1987), and (for a more rigorous mathematical description) Jordan and Smith (1999). Within this document, only linear analysis will be focussed on. This can be done in two ways.

If a perturbation is defined as a periodic function ($u_1 = Ce^{\iota(m\theta+\gamma t)}$ where C is the amplitude, m and t are the wave numbers) then one could proceed to adopt this within the appropriate system of equations. Then once can determine whether the potential energy of the system is in a stable state or not. Alternatively, one could construct an eigenvalue problem and examine the behaviour of the time constant. This would allow one to observe if the system would appear to "grow" implying an instability.

For instance, the linearised potential energy of a plasma system is given by.

$$\delta W = -\frac{1}{2}\int \xi F dV, \tag{6.42}$$

where ξ is the physical displacement of the system due to a disturbance. The force can be obtained from the relevant system of equations. If one observes a decrease in potential energy (i.e negative δW) then the system would be unstable.

For the eigenvalue approach, simply place a functional form of the disturbance (for instance, approximating as a wave using Euler's approximation). The flow is then deemed to be unstable if (for instance) the analysis dictates that the velocity would

grow exponentially.

The ideal kink instability is (as is in the name) an ideal MHD instability. Ideal refers to the fact that occurs in the absence of resistive component (i.e, the system of MHD equations will show an instability even if resistance is considered negligible. A perturbation for this can be of the form (Priest, 2014):

$$\boldsymbol{\xi} = f(z)[\xi^R(R)\hat{R} - i\frac{B_{0z}}{B_0}\xi^0(R)\hat{\phi} + i\frac{B_{0\phi}}{B_0}\xi^0(R)\hat{z}]e^{i(m\phi+kz)}, \tag{6.43}$$

where r, ϕ, z (R specifically is the radius of the flux rope) are the coordinates of a polar system, $\boldsymbol{B}$ is the magnetic field, and ξ is the displacement or perturbation. m and k are the mode numbers. Subsequent analysis shows (Hood and Priest, 1979; Baty, H.; Heyvaerts, 1996; Evstatiev *et al.*, 2006; Delzanno *et al.*, 2007; Priest, 2014) that the kink instability is achieved when the flux rope is perturbed (or twisted) greater than a specific angle ϕ.

Chapter 7

A Relaxation Model of Coronal Heating in Multiple Interacting Flux Ropes

7.1 Introduction

Recently, it has been shown using 3D magnetohydrodynamic (MHD) simulations that one kink-unstable flux rope can trigger energy release in a stable neighbour Tam *et al.* (2015). If the two ropes are initially sufficiently close, the unstable rope interacts with the stable one, releasing free magnetic energy from both flux ropes, with the two ropes merging through magnetic reconnection into a single twisted flux rope. This has important implications for coronal heating, since stored energy can be released even if a flux rope is stable. Subsequently, Hood *et al.* (2016) considered a set of 23 twisted loops, one unstable, with the remaining 22 loops stable, showing that the onset of instability in the one unstable loop triggered a series of mergers with the stable neighbours, with energy released in bursts as the loops merge in turn.

Such numerical simulations are very computationally demanding, and it is not viable to explore a wide parameter space. For this reason, a simpler, semi-analytical model has been developed. To this end, the methodology used within Taylor (1974, 1986) becomes apt for developing such a model.

Browning *et al.* (2014) uses relaxation to model merging flux ropes, with application to merging-compression formation in the MAST spherical Tokamak, and then applied to interacting solar coronal flux ropes. However, the initial state in this model represents adjacent flux ropes separated by current sheets, which does not address the onset conditions for flux rope merger and cannot readily be applied to the situation modelled numerically by Tam *et al.* (2015) and Hood *et al.* (2016).

Our aim here is to develop a relaxation model in which the initial state consists of a number of twisted magnetic threads in force-free equilibrium. The final relaxed state as the threads interact, and potentially merge, is determined using Taylor theory. The approach is developed and tested for a pair of flux tubes, and benchmarked against the 3D mumerical simulations of Tam *et al.* (2015). The methodology is set out in Section 7.2, with results presented in Section 7.3. Then, in Section 7.4, we extend the model to a system with a large number of flux ropes, making a comparison with the numerical results of Hood *et al.* (2016). Conclusions are presented in Section 7.5.

7.2 Theoretical approach and methodology

7.2.1 Initial field configuration

Our aim is to consider the interactions of a number of discrete twisted magnetic threads that are initially in force-free equilibrium. Therefore, following Tam *et al.*

(2015) and Hood *et al.* (2016) we model each individual thread as a cylindrical force-free flux rope (radius R_i and length L) with zero net-current (see also Melrose (1991); Hood *et al.* (2009); Bareford *et al.* (2011)).Thus, the azimuthal field B_θ is zero at the edge of the flux rope. In between the threads, there is a uniform axial field $B_z = B_e$. Initially, all fields are continuous, so that $B_z(R_i) = B_e$. We non-dimensionalise the equations by setting:

$$B = \frac{B^*}{B_0}, \;\; L = \frac{L^*}{L_0}. \tag{7.1}$$

We set the initial radius $R_i = 1$. Since our model is one-dimensional, the length is only a linear scaling factor, but for comparison with previous work, we specifically set $L = 20$. To non-dimensionalise the analysis, the magnetic permeability is also set to unity ($\mu_0 = 1$). Comparisons requiring numerical values are obtained by considering typical parameters for a coronal loop, for example, $B_0 = 0.01$ T, $\rho = 1.67 \times 10^{-12}$ kg m^{-3}, and $L_0 = 1$ Mm; a single unit of energy represented in this work corresponds to 7.96×10^{19} J ($\approx 10^{20}$ J).

In order to develop and benchmark the model, we first consider two initial flux ropes, but later (Section 7.4) we extend this to multiple flux ropes. A suitable model for the initial field, allowing direct comparison of our relaxation model with numerical simulations, is given by Hood *et al.* (2009); Tam *et al.* (2015):

$$B_\theta = \begin{cases} B_0 \lambda r (1 - r^2)^3, & r \leq 1 \\ 0, & r > 1 \end{cases}, \tag{7.2}$$

$$B_z = \begin{cases} B_0 \sqrt{1 - \frac{\lambda^2}{7} + \frac{\lambda^2}{7}(1 - r^2)^7 - \lambda^2 r^2 (1 - r^2)^6}, & r \leq 1 \\ B_0 \sqrt{1 - \frac{\lambda^2}{7}}. & r > 1 \end{cases}, \tag{7.3}$$

$$B_r = 0. \tag{7.4}$$

The initial magnetic field is chosen to be force-free (i.e. $\mathbf{j} \times \mathbf{B} = 0$). Since the flux rope arises from localised twisting at the photospheric footpoints, the azimuthal field (B_θ) must vanish at the edge of the rope (hence the field is continuous with the surrounding purely axial field). Thus, by Ampere's law, the net axial current along the loop must vanish. Indeed, the axial current associated with the fields in equation 7.2 changes sign between the centre of loop (r = 0) and the edge (r = 1), allowing the net current to be zero (see Hood *et al.* (2009)). Hence, the configuration arises as a result of localised twisting within the two regions of the photosphere. The parameter λ quantifies the twist in the flux rope. One observes this relationship by considering the angle of rotation of a field line from one end of the loop to the other,

$$\Phi(r) = \frac{LB_\theta}{rB_z} = \lambda L \frac{(1-r^2)^3}{\sqrt{1 - \frac{\lambda^2}{7} + \frac{\lambda^2}{7}(1-r^2)^7 - \lambda^2 r^2 (1-r^2)^6}}, \tag{7.5}$$

hence the twist on axis $r = 0$ is simply

$$\Phi_0 = \lambda L. \tag{7.6}$$

In order to ensure that each flux rope has an identical field at $r = 1$, allowing continuity with the surrounding uniform field, it is required that

$$B_0 \sqrt{1 - \frac{\lambda^2}{7}} = B_e, \tag{7.7}$$

is the same for each flux rope, where B_e is the external field (a constant axial field). B_e is set to 0.7329, which corresponds to $B_0 = 1$ and $\lambda = 1.8$.

As the twist is increased, the ropes will become kink-unstable. Previous calculations, taking line-tying at the ends of the flux ropes (Hood and Priest, 1979; Bareford *et al.*, 2011) into account, show that the ropes are linearly-unstable to the ideal kink mode at $\lambda_{crit} = 1.586$. Note that this value will change if the aspect-ratio L/R_i is changed. There is a strict upper limit on the allowable value of λ, since B_z must be real ($\lambda_{max} = 2.438$).

The magnetic helicity (K) is defined as:

$$K = \int_V \mathbf{A}.\mathbf{B}\, dV, \tag{7.8}$$

where $\mathbf{A}$ is the magnetic vector potential, such that $\nabla \times \mathbf{A} = \mathbf{B}$. Since the loop is not fully bounded by a magnetic surface, the expression for helicity must be adjusted to ensure gauge-invariance (Finn and Antonsen Jr., 1985). The most convenient implementation of the gauge-correction for a geometry such as ours, in which the field at the two ends of the loop $z = 0$ and L is identical, is to consider the loop to be a periodic system, that is, an infinite-aspect ratio torus. The necessary "gauge-correction" term arising due to an unspecified flux through the torus can be made to vanish by specifying $A_z(R) = 0$, where R is the loop radius (Bevir *et al.*, 1985; Browning *et al.*, 2014).

The aim here is to have an analytical model. However, given the form of the profile for B_z, the vector potential cannot be found analytically. Therefore, a polynomial approximation for B_z up to the seventh order is used. This is shown to provide a high degree of accuracy in section 7.2.8. Such an approximation was used instead of numerical integration since calculation of helicity requires repeated integration, and it is convenient to have explicitly analytic expressions for the various quantities. This approximation is only used to provide expressions for the helicity and the axial

flux; other quantities such as energy can be calculated directly from equation 7.3. Therefore, B_z is given by:

$$B_z = \sum_{n=0}^{7} C_n r^n. \tag{7.9}$$

The coefficients are determined by using a least squares polynomial fit after evaluating the field for a specific λ.

The expressions for energy, axial flux, and helicity are derived subsequently.

7.2.2 Energy

The magnetic energy is given by:

$$E = \frac{1}{2}\int_V \mathbf{B}^2 dV = \pi L \int_R r(B_z^2 + B_\theta^2) dr. \tag{7.10}$$

Using

$$B_z = B_0\sqrt{1 - \frac{\lambda^2}{7} + \frac{\lambda^2}{7}(1-r^2)^7 - \lambda^2 r^2 (1-r^2)^6}, \qquad B_\theta = B_0 \lambda r (1-r^2)^3, \tag{7.11}$$

and performing the integration, the magnetic energy is given by:

$$E = B_0^2 \pi L (\frac{1}{2} - \frac{\lambda^2}{16}). \tag{7.12}$$

7.2.3 Axial flux

The axial flux must be calculated using the approximate B_z, and is given by

$$\Psi = \int_S B_z dS = 2\pi \int_R r B_z dr = 2\pi \sum_{n=0}^{7} \frac{C_n}{n+2}. \tag{7.13}$$

7.2.4 Helicity

Calculating first the vector potential $\mathbf{A}$, where $\nabla \times \mathbf{A} = \mathbf{B}$:

$$\implies \begin{array}{c} \frac{\partial A_r}{\partial z} - \frac{\partial A_z}{\partial r} = B_\theta, \\ \frac{1}{r}\frac{\partial (r A_\theta)}{\partial r} - \frac{1}{r}\frac{\partial A_r}{\partial \theta} = B_z. \end{array} \tag{7.14}$$

For cylindrical fields as used here, $\mathbf{A} = (0, A_\theta(r), A_z(r))$, hence

$$A_z = -\int_R B_\theta . dr, A_\theta = \frac{1}{r}\int_R r B_z . dr. \tag{7.15}$$

Requiring that $A_z(r=1) = 0$, gives

$$A_z = -\int B_0 \lambda r (1-r^2)^3 . dr = B_0 \frac{\lambda}{8}(r^2-1)^4, \tag{7.16}$$

and (using the approximate form of B_z)

$$A_\theta = \sum_{n=0}^{7} \frac{C_n r^{n+2}}{n+2}. \tag{7.17}$$

Defining

$$K = \int_V (A_\theta B_\theta + A_z B_z) dV, \tag{7.18}$$

and using $B_z = \sum_{n=0}^{7} C_n r^n$, gives

$$K = 2\pi L B_0 \int_0^1 [\lambda r^2 (1-r^2)^3 \sum_{n=0}^{7} \frac{C_n}{(n+2)} r^{n+1} + \frac{\lambda}{8}(1-r^2)^4 \sum_{n=0}^{7} C_n r^n] dr. \tag{7.19}$$

Multiplying out the brackets and integrating gives

$$\begin{aligned} K = 2\pi B_0 \lambda L \sum_{n=0}^{7} C_n [&\frac{1}{8(n+2)} - \frac{1}{2(n+4)} + \frac{1}{(n+2)(n+4)} + \frac{3}{4(n+6)} - \frac{3}{(n+2)(n+6)} \\ &- \frac{1}{2(n+8)} + \frac{3}{(n+2)(n+8)} + \frac{1}{8(n+10)} - \frac{1}{(n+2)(n+10)}] \\ &= 2\pi B_0 \lambda L \sum_{n=0}^{7} C_n \frac{96}{(n+2)(n+4)(n+6)(n+8)(n+10)}. \end{aligned} \tag{7.20}$$

$$E = B_0^2 \pi L (\frac{1}{2} - \frac{\lambda^2}{16}), \tag{7.21}$$

$$K = 2\pi B_0 \lambda L \sum_{n=0}^{7} C_n \frac{96}{(n+2)(n+4)(n+6)(n+8)(n+10)}. \tag{7.22}$$

It should be noted in all the above expressions that, for fixed external field B_e, the field on the flux rope axis, B_0 is given as a function of λ according to equation (6). Thus, magnetic energy is indeed an increasing function of twist (λ).

For a system of multiple threads, the energy, axial flux, and helicity are determined as the summation of the individual quantities for each flux rope. Note that the

external (current-free) field makes no contribution to helicity, but does affect the total energy and axial flux - although the latter quantities will only alter if the volume of this region changes (since the field B_e is uniform and unchanging); this is discussed further in Section 7.2.5.

7.2.5 Relaxed state

The Taylor relaxation model (Taylor, 1974, 1986) determines the lowest energy state obtainable with the total helicity conserved. This predicts a magnetic field, which is a linear force-free field ($\nabla \times B = \alpha B$) with the value of α determined by the constraints that the helicity (K) and axial flux (Ψ) are the same as in the initial state. This is usually accomplished by conserving the dimensionless ratio K/Ψ^2. In a cylindrical configuration, the relaxed state is given by

$$B_\theta = B_1 J_1(\alpha r), \quad B_z = B_1 J_0(\alpha r), \tag{7.23}$$

where B_1 is a constant (the magnitude of the relaxed field on axis) and J_0 and J_1 are the zeroth and first order Bessel functions of the first kind.

In the following, we assume that the relaxed state is a cylindrical flux tube with radius R_f. The external (potential) field remains unaltered during the relaxation process. Unlike the laboratory situation, relaxation in the solar corona is a free boundary problem (Dixon *et al.*, 1989). The simulations strongly suggest that the relaxed field is a flux tube of approximately circular cross-section, and it is likely that a circular boundary should give lowest energy (by analogy, for example, with the shape of bubbles).

The external field outside the flux ropes is unchanged during the relaxation process. It should be noted that, in general, the full field configuration in the relaxed state thus contains a current sheet at the flux rope boundary (the magnetic field is discontinuous). This is observed to some extent in simulations, although the sheet becomes a layer of finite width (see also Bareford *et al.* (2013)). A current sheet is also predicted in models of localised relaxation applied to the edge region of Tokamaks (Gimblett *et al.*, 2006).

For the relaxed state (equation 7.23), the normalised helicity, with the gauge-invariance condition $A_z(R_f = 0)$, can thus be shown to be

$$\frac{K}{\Psi^2} = \frac{L}{2\pi R_f} \frac{\alpha R_f [J_0^2(\alpha R_f) + J_1^2(\alpha R_f)] - 2J_0(\alpha R_f) J_1(\alpha R_f)}{J_1^2(\alpha R_f)}, \tag{7.24}$$

(in agreement with Taylor (1974, 1986)).

7.2.6 Relaxation calculation

We begin by developing the relaxation model to represent as closely as possible the 3D MHD simulations undertaken by Tam *et al.* (2015), thus testing and benchmarking the approach. As in Tam *et al.* (2015), four cases for the initial field, each with two ropes, were considered. The cases vary in terms of the twist λ, and whether or not they merge in a magnetic reconnection event (which in the simulations is controlled by the distance between the threads). In the simulations, merging occurs when the two flux ropes initially just touch at a single line (i.e. the centre of the second flux rope is exactly $2R_i$ away from the centre of the first). If the flux ropes are sufficiently separated, they do not interact and it is likely that there is a maximum separation below which interaction occurs. The Taylor relaxation model does not explicitly model the location of the initial flux ropes, but we can specify whether

the final state should be a single flux rope, or whether the flux ropes should relax individually, in order to compare with the relevant simulations.

In order to provide direct comparison with the numerical results, a "simulation box" can be defined. The simulation box is defined as a rectangular cross-section region outside the flux ropes with a uniform axial magnetic field $B_z = B_e = B_0\sqrt{1 - \frac{\lambda^2}{7}}$, of dimensions 8 by 4 by 20. When a simulation box is used, the total energy of the system includes a contribution from the external field. A simulation box setup is illustrated for cases 2 and 4 in Figure 7.1. The energy of the external region remains unchanged if the the volume of the flux tubes remains constant, but may change otherwise.

As discussed above, the relaxed state is assumed to be cylindrical but it is not immediately clear what the radius of the final flux rope should be. Simulations of the relaxation of a single unstable twisted flux tube show that the relaxed state has limited extent a little larger than the initial flux tube, which is a form of "partial relaxation" (Bareford *et al.*, 2013). Thus, initially, we considered the outcomes of the relaxation model treating the final radius (R_f) as an unspecified variable, with the energy change recorded accordingly. Various approaches were then used to determine the final radius. The first is simply a conservation of volume (thus the total cross-sectional area of the initial and final flux ropes is the same). The second is equating the magnetic pressure to the background magnetic pressure (which is unchanged during the relaxation process, as the external field is unchanging), which is illustrated in equation 7.2. The third constraint takes account of the fact that the dissipated magnetic energy is converted into thermal energy and, hence, the gas pressure inside the flux rope increases, and should be added to the magnetic pressure. This is illustrated in equation 7.27, where an ideal gas has been assumed and γ is the adiabatic index. Constraints 2 and 3 maintain force balance across

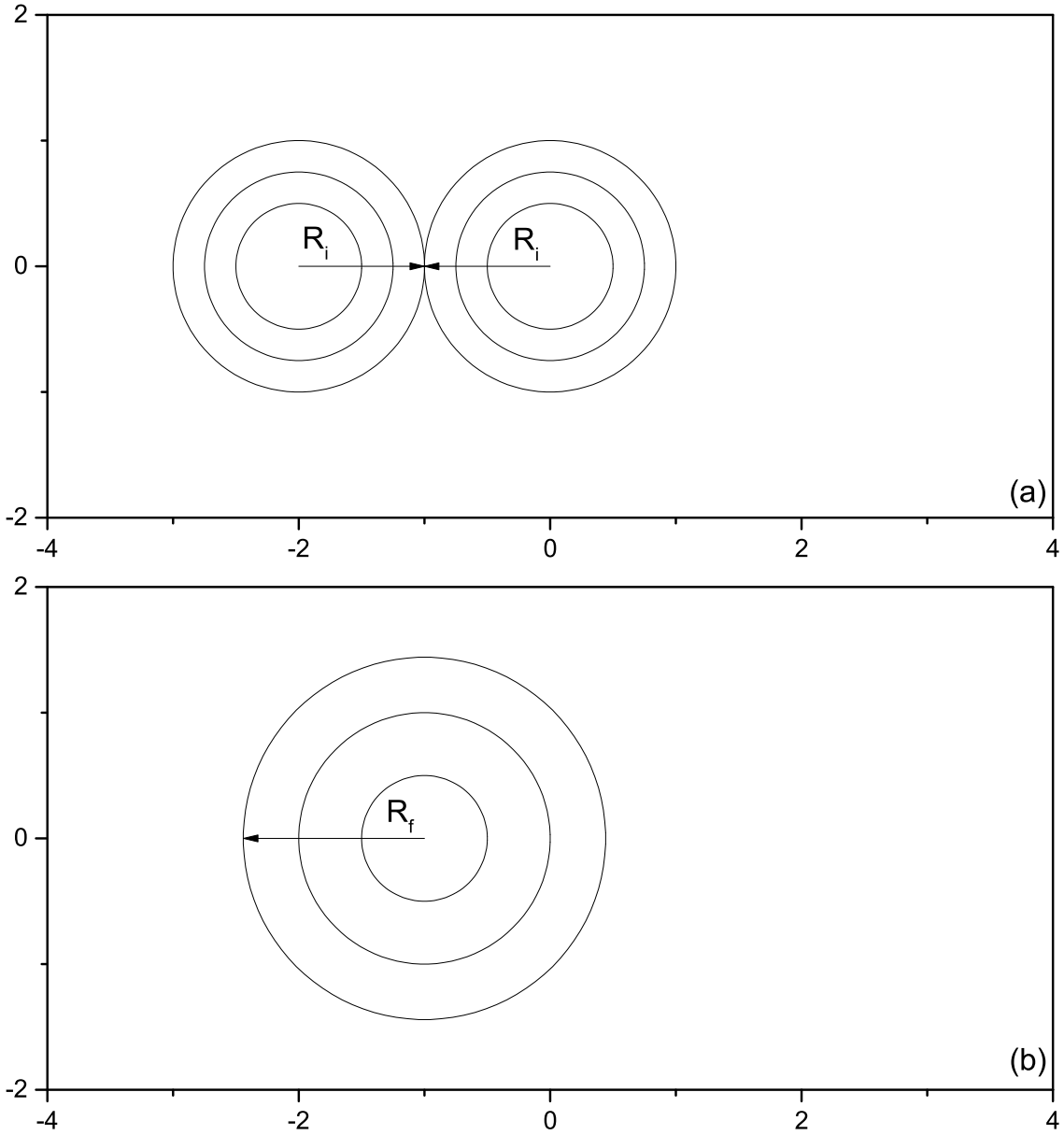

Figure 7.1: Azimuthal field lines of flux ropes as initially setup (a) and then relaxing to form a single flux rope (b) in an $8\times4\times20$ simulation box. The final state depicted is specific to cases 2 and 4.

the interface between the twisted flux rope and the external field. Constraint 1 has no particular physical justification but is simple to apply and appears to match the simulations quite well, and will be shown to produce rather similar results in terms of energy released. Another possible constraint could have been that of $B_\theta(R_f) = 0$. However, since the magnetic pressure constraint finds that $B_\theta \approx 0$, this is deemed redundant.

To summarise, the radius is constrained by:

- **Constraint 1:** Conservation of volume between the initial and final flux ropes,

$$\sum^{n\,ropes} \pi R_i^2 L = \pi R_f^2 L \implies R_f = \sqrt{\sum R_i^2}. \tag{7.25}$$

- **Constraint 2:** Equating magnetic pressure at the edge of the final flux rope to the background magnetic pressure,

$$B_z^2(R_f) + B_\theta^2(R_f) = B_e^2 = B_0^2(1 - \frac{\lambda^2}{7}). \tag{7.26}$$

- **Constraint 3:** Equating the sum of magnetic pressure at the edge of the final flux rope and built up gas pressure to the background magnetic pressure,

$$\frac{\delta E(\gamma - 1)}{Vol} + \frac{1}{2}(B_z^2(R_f) + B_\theta^2(R_f)) = \frac{1}{2}B_0^2(1 - \frac{\lambda^2}{7}). \tag{7.27}$$

The methodology is then as follows. An initial field is selected, as described in Section 7.2.7. The value of α in the final state is calculated by equating the helicity of the final flux rope (normalised with respect to axial flux - which is also conserved) to the total helicity of the initial flux ropes (equation 7.22), for a given radius of the final flux rope, R_f. For constraints 2 and 3, R_f is iterated to achieve the required

Table 7.1: Initial field conditions for the relaxation of two flux ropes.

Case 1	Ropes not touching and relaxing separately; $\lambda_1 = 1.8$, $\lambda_2 = 1.8$.
Case 2	Ropes touching and merging; $\lambda_1 = 1.8$, $\lambda_2 = 1.8$.
Case 3	Ropes not touching, unstable rope relaxing separately; $\lambda_1 = 1.4$, $\lambda_2 = 1.8$.
Case 4	Ropes touching and merging; $\lambda_1 = 1.4$, $\lambda_2 = 1.8$.

pressure balance. The energy release, which is presumed to be converted into plasma thermal energy, is then simply the difference between the energy of the initial state and the final state.

7.2.7 Cases studied

In order to benchmark the relaxation model, we first develop it for the same cases studied numerically by Tam *et al.* (2015). The various cases for the initial field considered are given in table 7.1.

Thus cases 1 and 2 have two unstable flux ropes, while in cases 3 and 4, one flux rope is unstable and the other is stable - hence the latter will not release any energy unless somehow disrupted. In cases 2 and 4, the flux ropes merge into a single flux rope. In cases 1 and 3, the unstable flux rope ($\lambda = 1.8$) relaxes individually to constant state.

Later, in Section 7.4, we also consider a much larger array of flux ropes, representing the avalanche situation simulated in Hood *et al.* (2016).

7.2.8 Validation of field approximation

We first check the accuracy of the polynomial approximation to the axial field profile (equation 7.9; see Figure 7.2). Here, excellent agreement is shown between the

approximation to the field (equation 7.3) and the exact force-free field.

Within Figure 7.2, one observes that the fit is very good since only three curves can be visually observed despite six being plotted, which allows confidence in using the approximation. Further confidence is provided by matching the B_z profiles (Figure 7.3) to the ones in Tam *et al.* (2015).

The initial total magnetic energy for cases 1 and 2 was found to be 175.52 and for cases 3 and 4 to be 174.37 (in dimensionless units). These are in good agreement with the associated values reported in Tam *et al.* (2015).

7.3 Results

7.3.1 Effect of the radius of final flux rope

Initially, the radius R_f of the final flux rope was varied to observe the dependence of the energy output on this quantity, bearing in mind that the relaxation is a "free surface problem" in the corona. Figure 7.4 shows the energy release from two flux ropes merging into one (as in cases 2 and 4) as a function of the final radius, R_f. Similarly, Figure 7.5 shows the energy released due to a single flux rope relaxing (as in the case of the unstable flux ropes in cases 1 and 3). The energy is calculated both with a "simulation box" (in which the magnetic energy of the external region varies) and without (in which only the energies of the flux ropes are included).

If two flux ropes relax into a single rope, and volume is conserved, the radius of the final flux rope will be $\sqrt{2}$, as indicated by the vertical line in Figure 7.4. Note that if the volume is conserved (which is similar to the situation in a laboratory plasma confined within a rigid container), the energy change is negative - as expected for a relaxation to a minimum energy state. In this case, we expect that

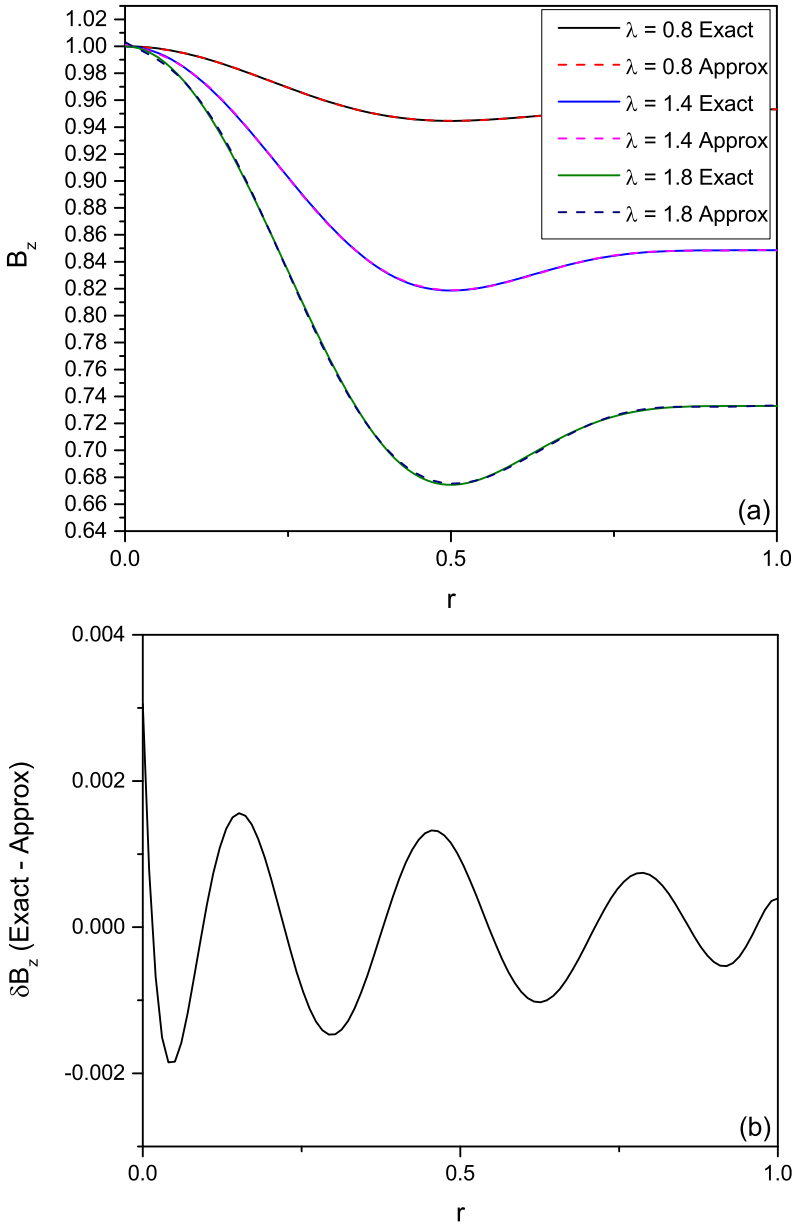

Figure 7.2: (a) Approximating polynomial and exact function for axial field $B_z(r)$, demonstrating the quality of fit, for $\lambda = 0.8$ (approximate, orange dashed, and exact, black), $\lambda = 1.4$ (approximate, pink dashed, and exact, blue), $\lambda = 1.8$ (approximate, dark blue dashed, and exact, green). Note that only three curves are visible since the exact and approximate curves are almost identical. (b) The difference between the exact and the approximation function for $\lambda = 1.8$.

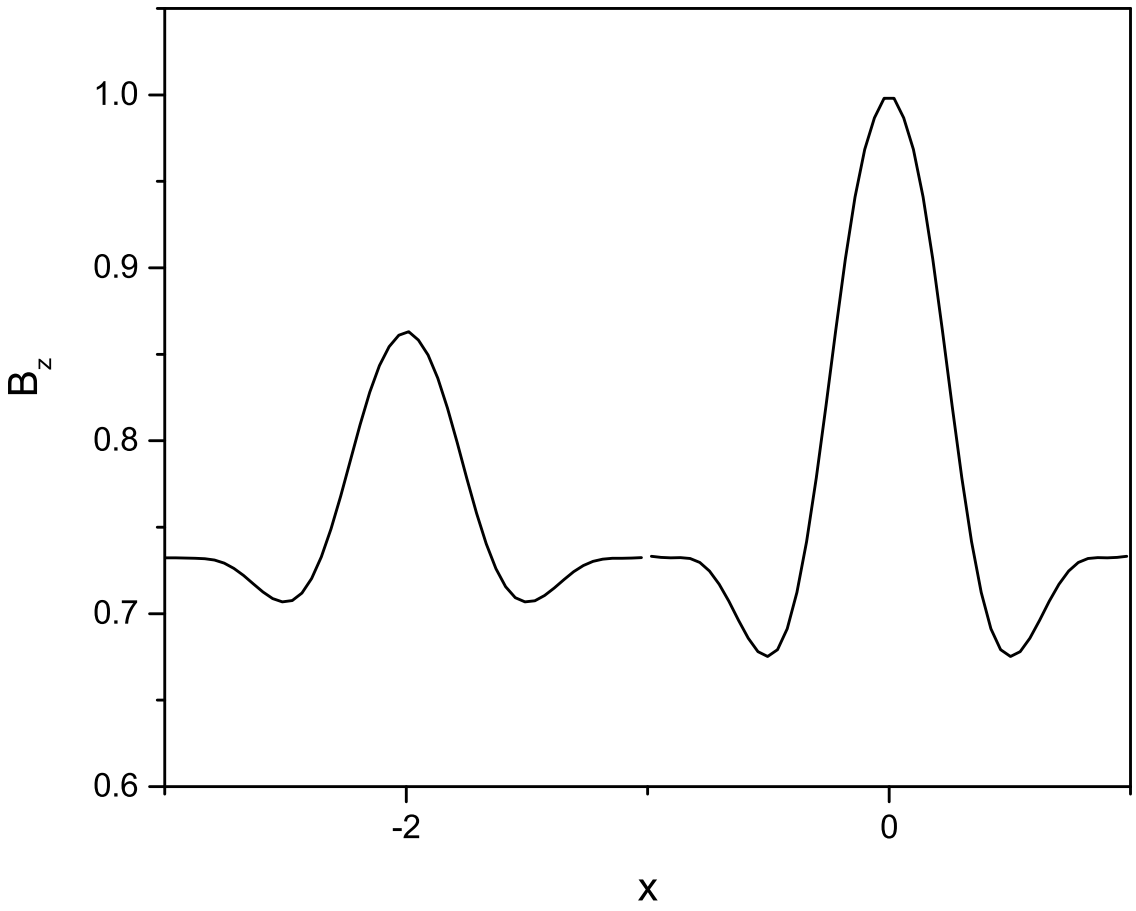

Figure 7.3: Initial axial field B_z for two flux ropes, using the approximate polynomial, for case 4; the flux ropes centred at $(0, 0)$ and $(-2, 0)$.

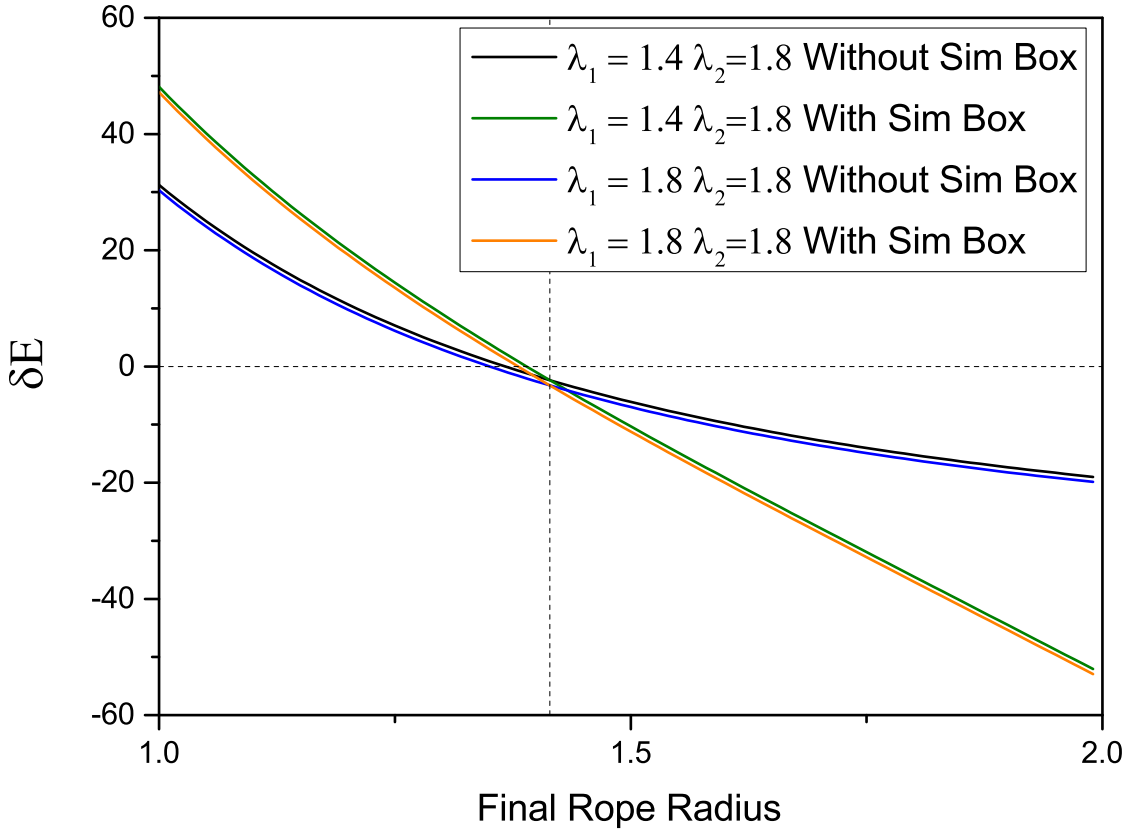

Figure 7.4: Energy change for two flux ropes merging and relaxing against final rope radius, both with (green, $\lambda_1 = 1.4$ $\lambda_2 = 1.8$; orange, $\lambda_1 = \lambda_2 = 1.8$) and without (black, $\lambda_1 = 1.4$ $\lambda_2 = 1.8$; blue, $\lambda_1 = \lambda_2 = 1.8$) a simulation box. Positive values represent an increase in energy from the initial to final state. The vertical line represents conservation of volume.

the released magnetic energy is converted into thermal energy. Initially, as demonstrated in simulations (Browning *et al.*, 2008; Hood *et al.*, 2009; Tam *et al.*, 2015) some magnetic energy is converted into kinetic energy associated with reconnection outflows, but this is viscously dissipated as a relaxed state is approached. If the flux tube volume decreases significantly, the magnetic energy rises, due to the increase in energy caused by compression dominating the decrease due to relaxation; we do not expect this situation to arise in practice (as some external work would need to be done to compress the flux ropes). Conversely, there is an increasing conversion of magnetic energy into heat as the flux tube volume increases.

Furthermore, note that when volume is conserved, the cases with and without "simulation box" are identical - because the axial field external to the flux ropes is unchanged in both magnitude and volume through the relaxation, and hence makes no contribution to the energy change. The released energy depends quite strongly on the choice of final radius, and we now consider the possible ways in which this can be determined.

7.3.2 Calculation of energy release and comparison with simulations

We now apply the three constraints that might determine the radius of the relaxed flux rope, as set out in Section 2.3 (eqs. (7.25) to (7.27)).

For constraints 2 and 3, the radius is determined by iterating R_f until the appropriate pressure balance is attained. The energy release is calculated for initial fields for each of the four cases, which can then be compared with the outcomes of the 3D numerical simulations Tam *et al.* (2015). The latter are calculated as the difference in magnetic energy between the initial value and that at the end of the simulation; we note that

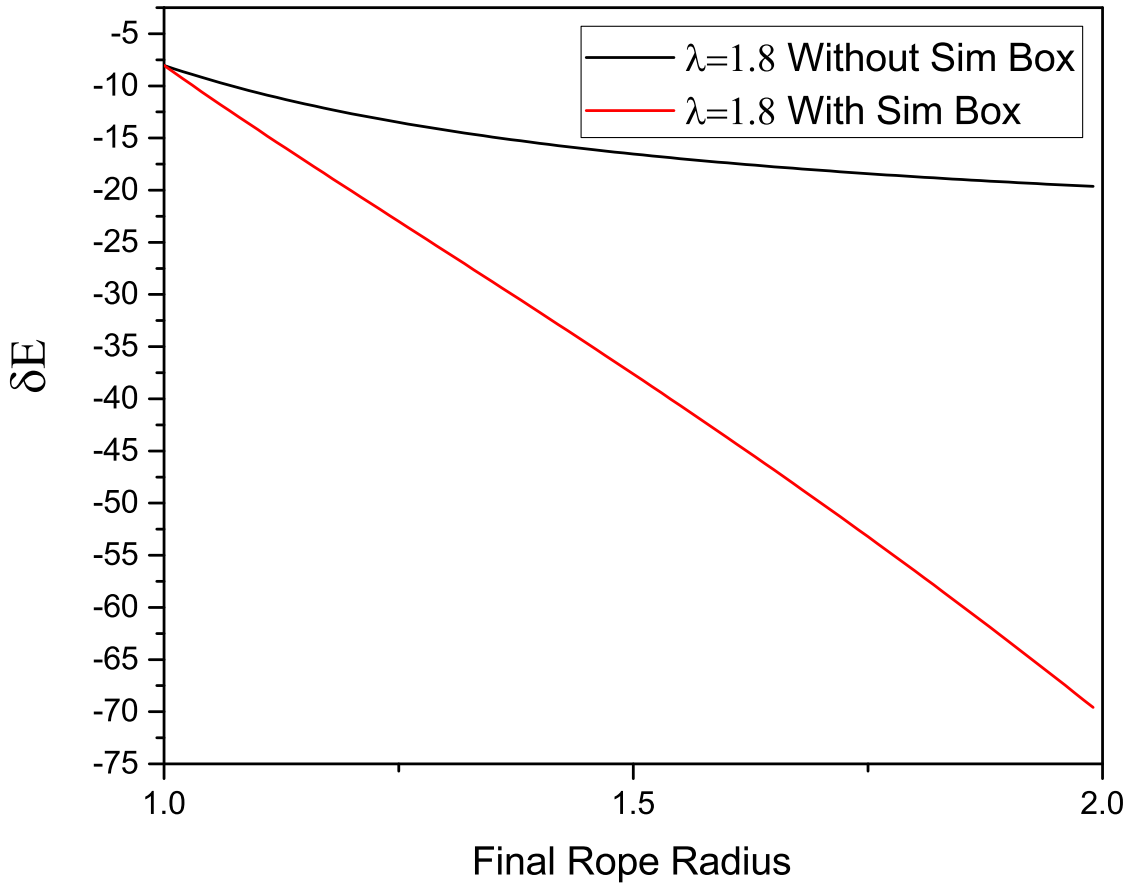

Figure 7.5: Energy output for a single flux rope relaxing ($\lambda = 1.8$) against final rope radius (R_f) with (red) and without (black) a simulation box.

Table 7.2: Results of the Taylor model compared to the MHD model.

Case	**Final Radius**				**Taylor δE**			**MHD δE**
	Constraint 1	*Constraint 2*	*Constraint 3*	*MHD (estimate)*	*Constraint 1*	*Constraint 2*	*Constraint 3*	
1*	1.0 (each)	0.999 (each)	1.018 (each)	1.0-1.5	-2.70	-2.608	-3.88	-3.031
2	1.414	1.412	1.445	1.3-1.5	-3.26	-3.164	-4.69	-3.069
3*	1.0 (each)	0.999	1.006	1.2-1.5	-1.35	-1.304	-1.94	-1.5
4	1.414	1.413	1.437	1.4-1.5	-2.36	-2.29	-3.41	-2.3

Note: *Case 3 only considers one flux rope (in the Taylor model) resolving itself since the first rope is stable, case 1 is twice that of case 3. The force free parameter (α) for case 2 is 0.258, for case 4 is 0.2133, and for a single kink unstable flux rope of $\lambda = 1.8$ is 0.510.

this has some margin of uncertainty, since the energy is still changing to some extent. From Table 2, it can be seen that there is generally good agreement between the numerical MHD result and the relaxation model. Also, the calculated energy release does not depend strongly on the choice of constraint. Some discrepancies between the numerical energy release and the relaxation predictions arise; both because the numerical simulations do not necessarily achieve full relaxation by the end of the simulation and because the expansion in loop radius observed numerically for a single relaxing loop is not fully accounted for by any of our constraints. The final radius for two merging loops is much better predicted by our model (all constraints giving little change in volume) than for a single loop.

Constraint 3 is arguably the most physically correct, as it accounts for the loop expansion due to plasma heating. However it is quite complex numerically, as it requires multiple stages of numerical iteration. The energy release predicted by the relaxation model in this case is somewhat larger than the numerical value: this may be because the fully relaxed state is not attained by the end of the numerical simulations. Constraint 1 (constant volume), on the other hand, has no clear physical justification, but is simple to apply, and the calculated energy release agrees relatively closely with the other constraints. Therefore, this could be useful in future modelling. Here, we choose to use Constraint 2 in the following sections, as this gives the best agreement with the numerical results and is relatively simple to apply. We may also compare the predicted final radius from the three constraints with the outcome of

the MHD simulations; however, it is difficult to measure this accurately from the simulations, and this cannot be used to discriminate between the three proposed Constraints. It does appear that when an individual flux rope relaxes (as in cases 1 and 3), there is a clear expansion of the rope, which has been suggested to be approximately 1.2 times the initial radius (Bareford *et al.*, 2013). The analysis of Bareford *et al.* (2013) suggests that this is due to the unstable twisted flux rope reconnecting with the surrounding axial field and thus 'eating into' the untwisted field region. This effect is not accounted for in our model, although it could be. The extent of this expansion is determined essentially by the nonlinear amplitude of the kink instability, but at present, we have no way to predict this a priori, and this is a subject for future investigation.

In general, there is very good agreement between the energy changes predicted by the relaxation model and the outcomes of the simulation. Furthermore, there is a very clear consistency in the trends of variation between the different cases.

7.3.3 The dependence of energy release on initial fieldline twist

The major advantage of the relaxation approach is that the energy can be calculated easily for a wide parameter space, and thus (in contrast with numerical simulations, which are very demanding of computer resources), we can explore how coronal heating varies with the paramaters of the twisted flux ropes. Thus, having benchmarked the approach against the simulations, we now investigate how the energy release varies with the flux rope twist, quantitified by the parameter λ. We thus calculate the energy change for the full range of possible initial twists for a pair of flux ropes. For each pair of λ values, the initial energy and helicity are calculated as described

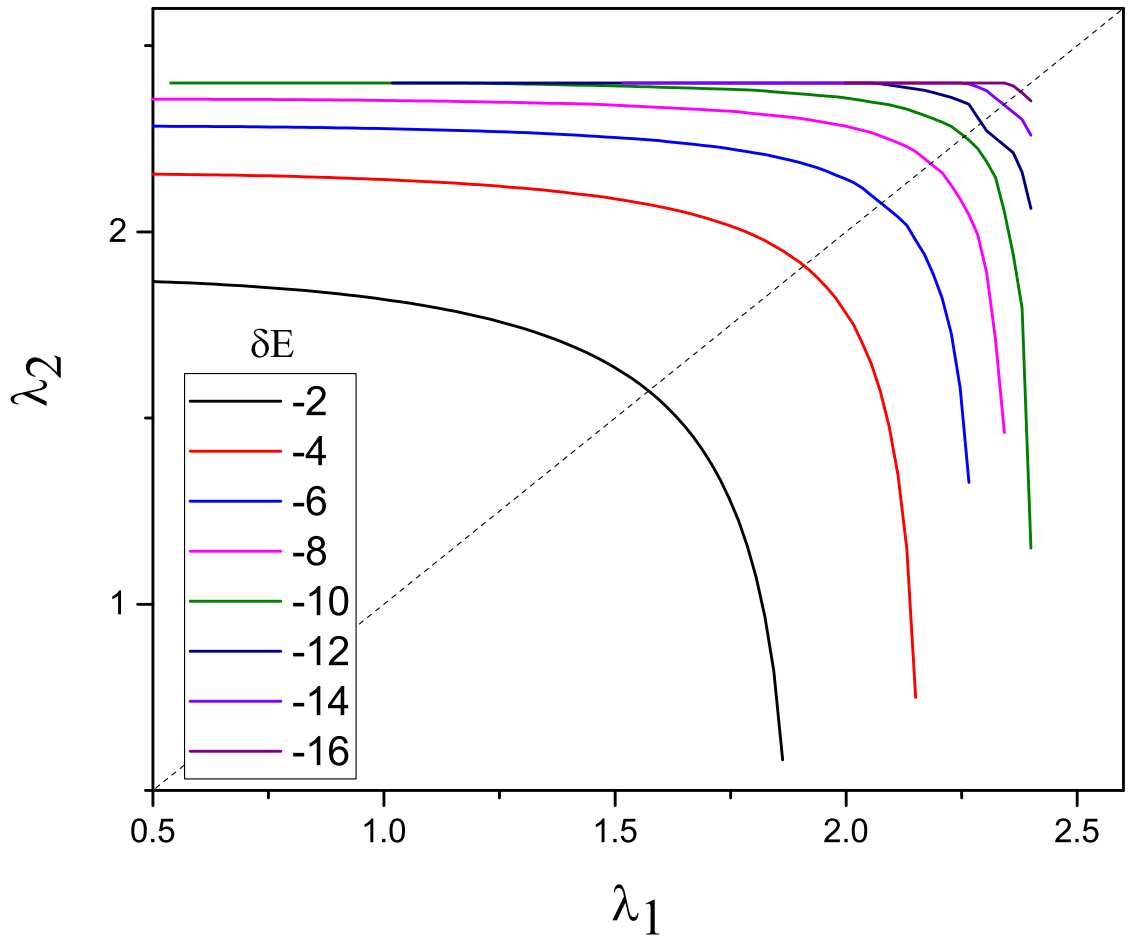

Figure 7.6: Contours of energy change for two flux ropes merging and relaxing with various λ. The dotted line represents $\lambda_2 = \lambda_1$.

in Section 2.1 above (with the set of coefficients C_n determined for each λ). The external field B_e is held fixed, so that the peak axial field B_0 is determined by equation 7.7. The flux ropes are assumed to merge, relaxing to a single constant-α flux rope. The resulting energy change is illustrated in the form of a contour map in Figure 7.6. Note that, in order for relaxation to happen at all, at least one flux rope must be unstable, so the region in which both values of λ are less than approximately 1.6 should be excluded.

As one can observe, the contours depict an increasing output of energy for higher overall twist. Furthermore, the energy output seems to be dominated by the con-

tribution of a highly unstable flux rope, as the contours are closely parallel to the x and y axes, respectively, for larger twist. We also note that the energy output rises strongly as λ increases towards its upper limit (i.e. $\lambda_{max} = 2.438$, beyond which B_z becomes imaginary), tending to infinity at this limit. It should be noted that this is purely a mathematical artefact of the flux rope configuration, infinite energy is not physically possible! However, whilst the general increase of energy release with field line twist is entirely expected, this singular behaviour is an artefact of the chosen mathematical model. The dependence of energy change on twist is further shown in Figure 7.7, which considers two identical initial flux ropes $\lambda = \lambda_1 = \lambda_2$ (corresponding to the dotted line on Figure 7.6). Figure 7.8 shows the variation of the force-free parameter (α) with varying twist; the other flux rope is fixed at $\lambda = 1.8$. One can observe that the parameter increases as the twist increases.

7.4 Large multi-threaded flux ropes

One strength of the Taylor model is its ease of applicability to larger regions, and more complex initial fields, without an increase in computational requirements. Hood *et al.* (2016) used 3D MHD simulations to demonstrate an avalanche of heating in an array of 23 twisted flux ropes, consisting of one unstable rope surrounded by stable ropes. However, such simulations are highly demanding of computational resources. We, therefore, consider this situation using the relaxation approach. The initial conditions were set to have one central flux rope unstable at $\lambda = 1.8$ surrounded by stable flux ropes, $\lambda = 1.4$, as depicted in Figure 7.9. In the simulation described by Hood *et al.* (2016), an avalanche was observed as the unstable flux rope "absorbs" the other flux ropes in a cascading sequence, releasing energy from the stable twisted flux ropes in succession.

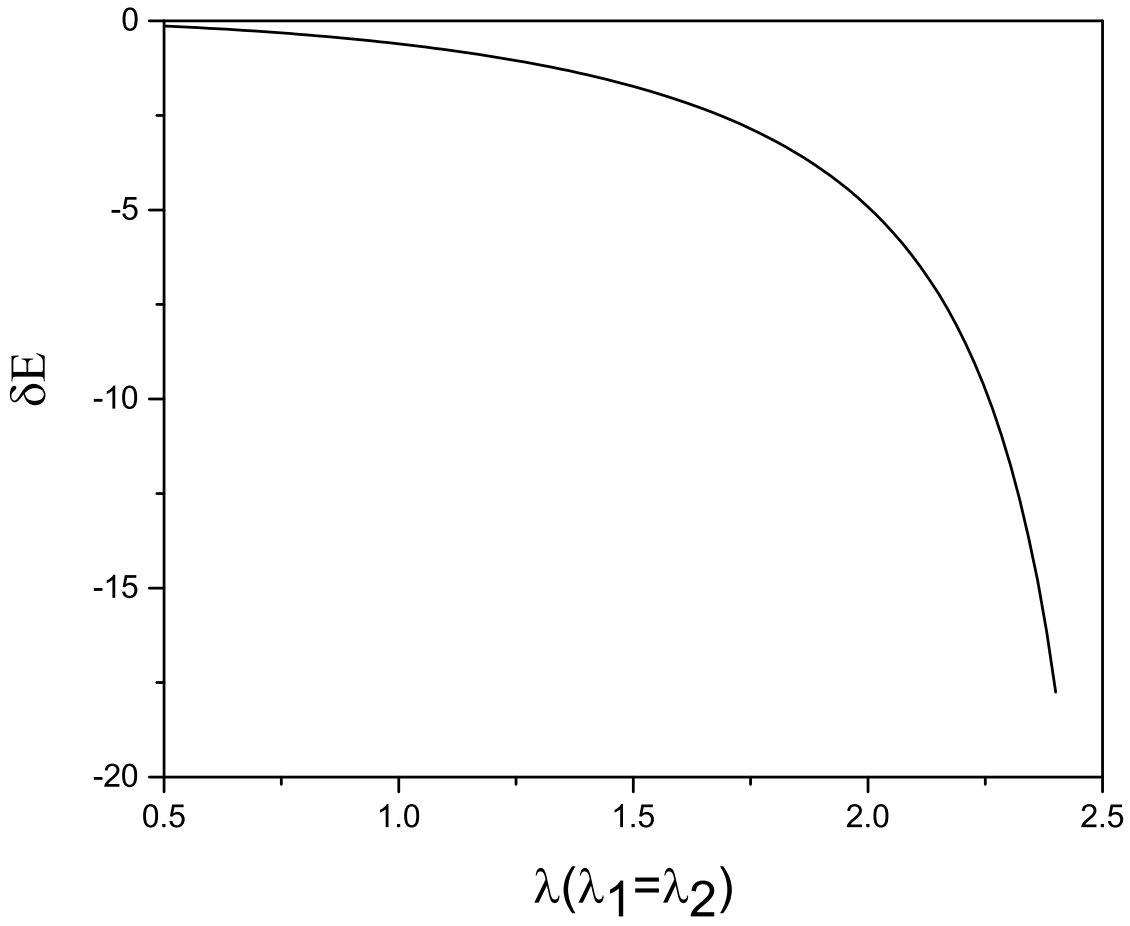

Figure 7.7: Energy output as a function of twist for two initially identical flux ropes $\lambda = \lambda_1 = \lambda_2$

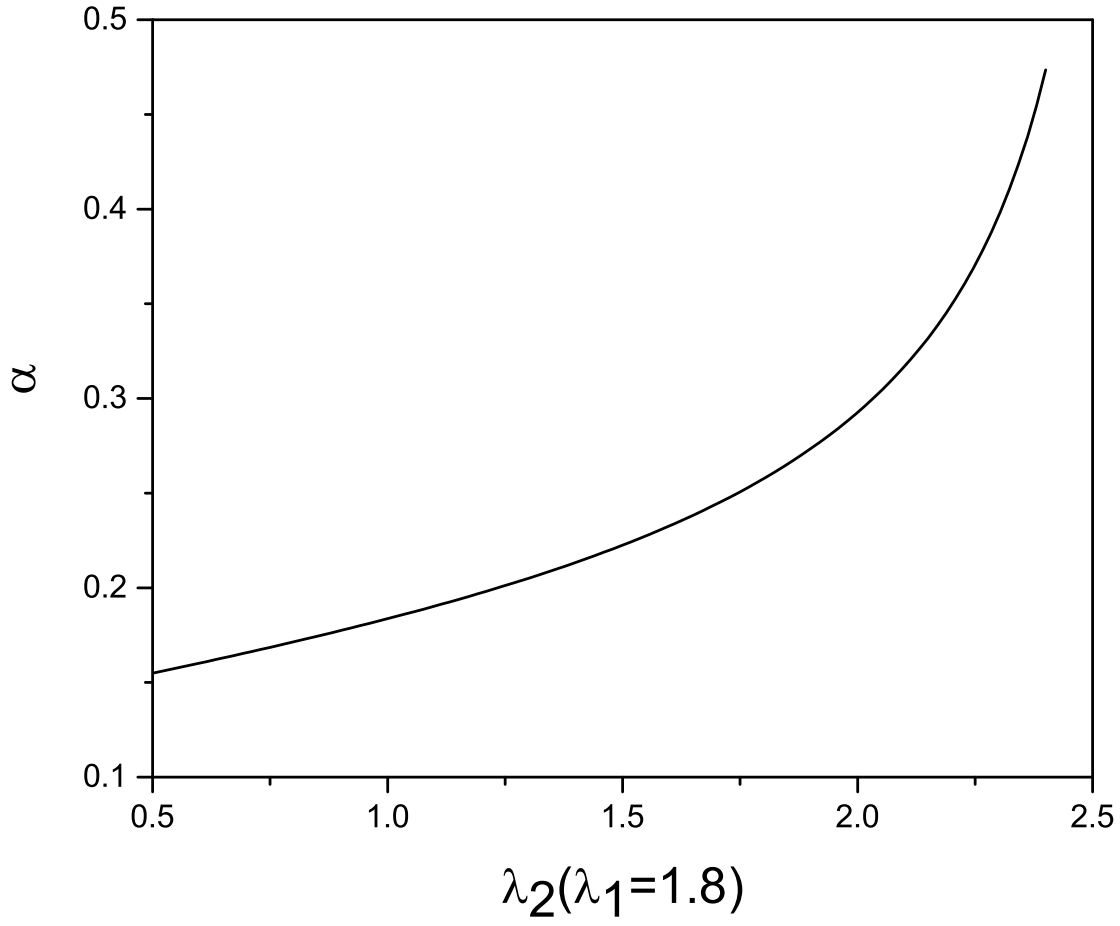

Figure 7.8: Variation of α vs. λ_2, where λ_1 is fixed at 1.8.

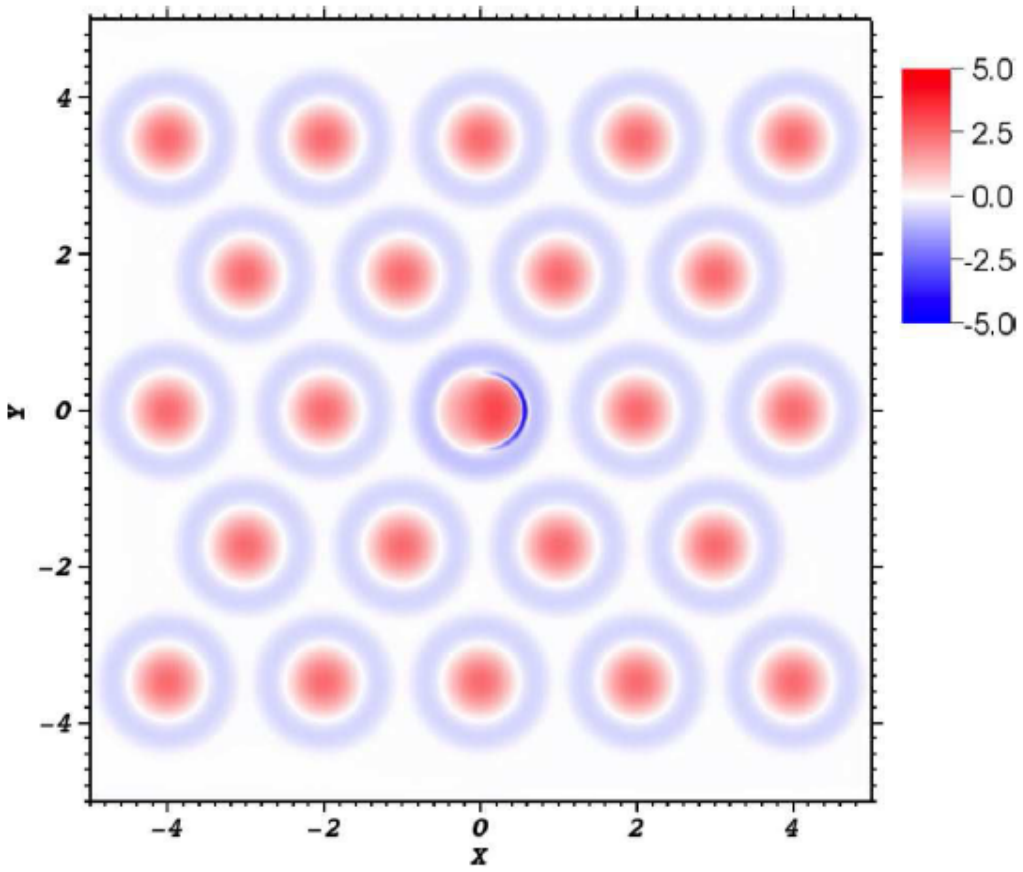

Figure 7.9: Simulation setup for 23 flux ropes merging. The Figure shows current density in the midplane $z = L/2$, taken from the early stage of the MHD simulations. The central rope is the unstable flux rope ($\lambda = 1.8$) while the rest are stable ($\lambda = 1.4$). Note that the central unstable flux rope shows signs of the initial kink instability, with a current sheet forming at the right-hand side of the loop. Originally published in Hood *et al.* (2016)

Table 7.3: Results of the Taylor model compared to the MHD model for the 23 flux rope simulation.

Final Radius				**Taylor** δE			**MHD** δE
Constraint 1	*Constraint 2*	*Constraint 3*	*MHD (estimate)*	*Constraint 1*	*Constraint 2*	*Constraint 3*	
4.12	4.12	4.18	4.2-4.8	-15.1	-14.9	-22.2	-14.2

Note: It should be noted that only 18 ropes relaxed in the simulation and the energy output from the Taylor model is provided up to this point only.

The approach in applying the Taylor model is similar to the preceding work; at each stage, the individual energies and helicities are calculated, then superimposed to find the total value. However, we now extend the approach described for two flux ropes in Section 7.3 to superimpose the flux ropes one at a time, providing a direct comparison to the avalanche model. Thus, first a stable flux rope and an unstable one are relaxed into a single flux rope (as in case 4 above). Then, this is combined with a further stable flux rope, and relaxed into a new combined (larger) flux rope - and so on. At each stage, helicity is conserved, and the energy change is evaluated. The results are presented in Table 7.3, and illustrated in Figure 7.10. For these purposes, it is assumed that each relaxation takes the same time, and this timestep has been chosen to match the overall time for the simulations.

In this case, the Taylor and MHD models are seen to be in very good agreement. It is further observed that the energy drop between each step is slowly approaching a constant energy release. A possible explanation is as follows. The Taylor model assumes a fully relaxed state. As each additional stable flux rope (which are identical, with $\lambda = 1.4$) is absorbed, almost all the free energy of this rope is released. Once the energy output is dominated by the $\lambda = 1.4$ flux ropes rather than the single unstable ($\lambda = 1.8$) one, then the energy output is simply directly proportional to the number of flux ropes merged. It is noted that in the MHD simulation, only 18 flux ropes merged. It is unclear whether or not there would be further merging if the simulation were run for longer. However, this could not be checked without risking inconsistency due to numerical errors. One possible explanation for the termination

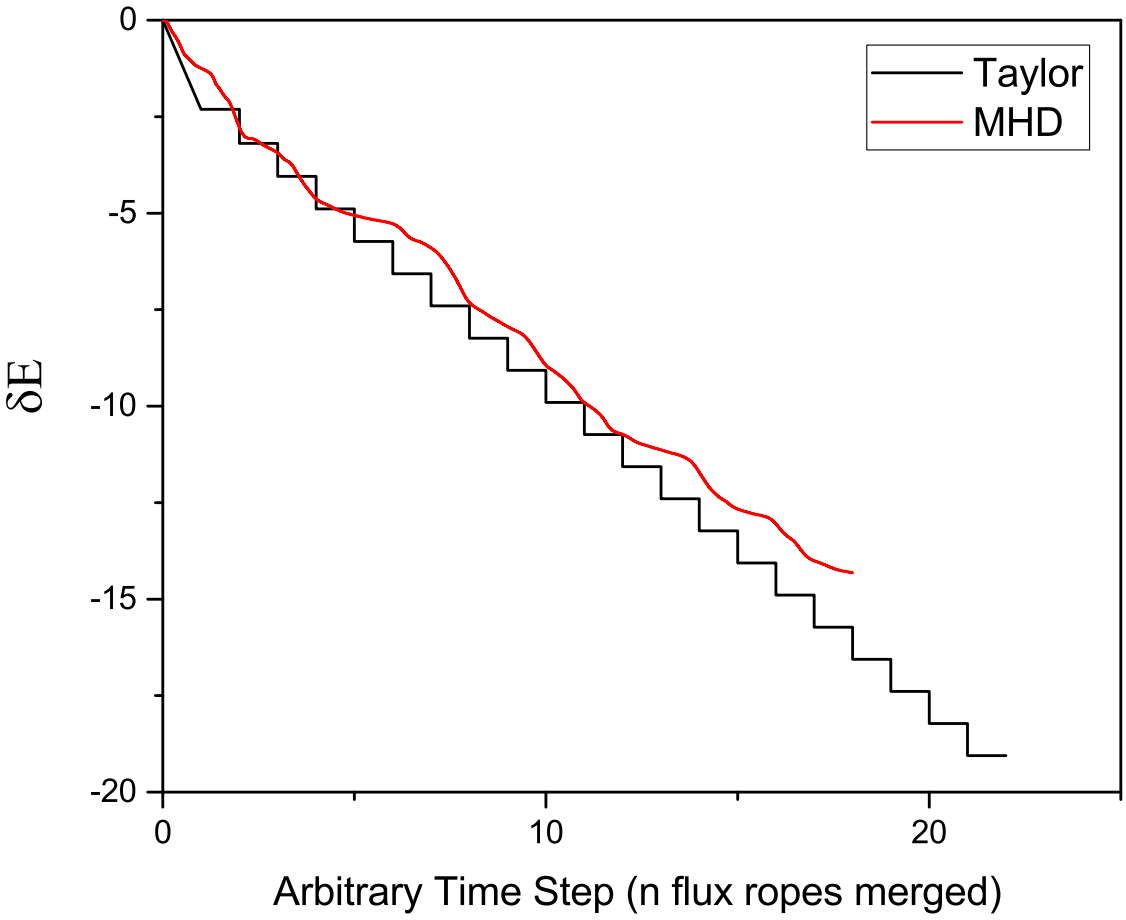

Figure 7.10: Energy release from merging of individual flux ropes showing the MHD simulation (red) and relaxation model (black). The arbitrary time step depicts the number of flux ropes that have been absorbed into the reconnection process. The MHD time has been normalised to scale to the Taylor model. This is needed since the Taylor model does not provide a time factor.

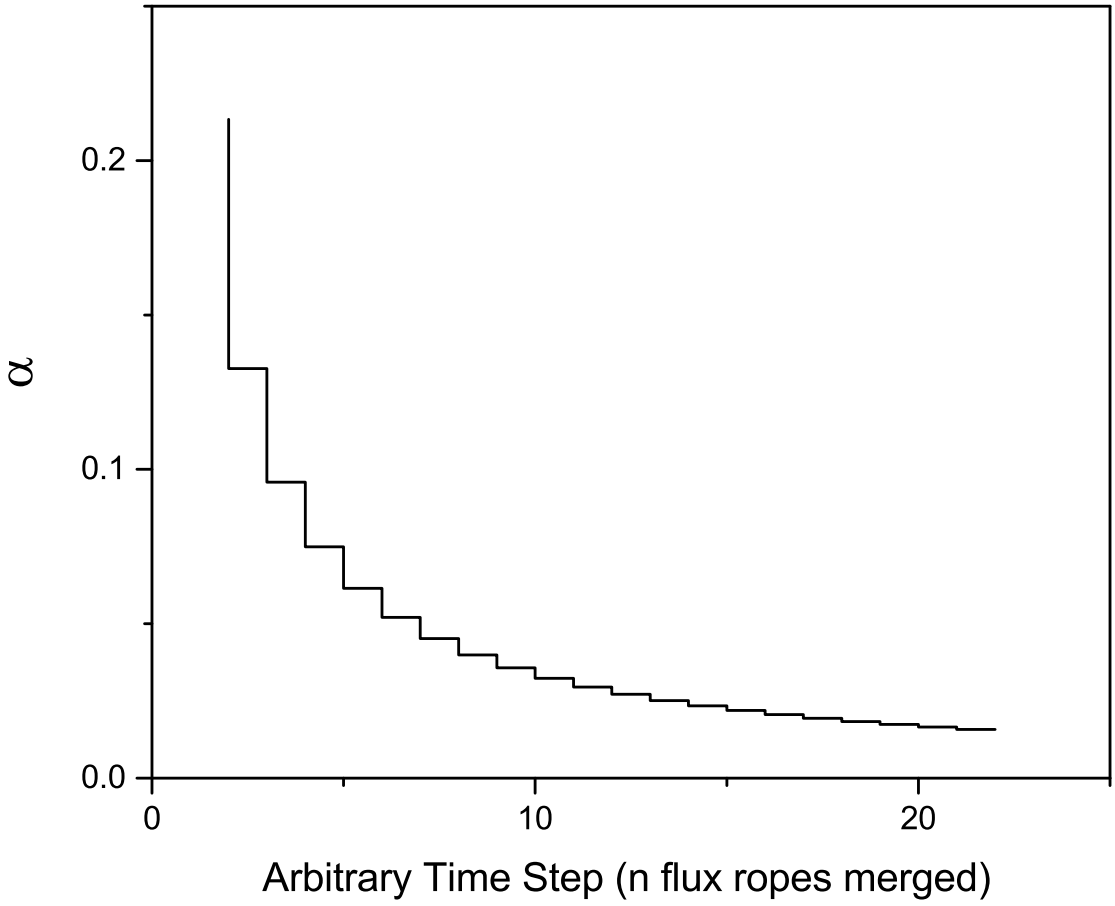

Figure 7.11: Variation of force-free parameter, α, for the avalanche model.

of the avalanche is provided, however, by observing the force-free parameter (α) for the avalanche model (Figure 7.11). As one can observe, the parameter appears to have an exponential-type decay. This suggests that as it approaches a minimum value, the current sheet surrounding the relaxed field (the Taylor model is not zero at the edge therefore resulting in an azimuthal current sheet) will become very weak after a large number of threads have merged, and no longer be sufficient to cause a disruption in the neighbouring flux ropes.

7.5 Discussion & Conclusions

We have presented a model for the energy released as one, two or many twisted flux ropes relax, and in (some cases) merge into a single flux rope, based on a helicity-conserving relaxation as hypothesised by Taylor (1974). A direct comparison shows that the Taylor model and 3D MHD simulations (Tam *et al.*, 2015) are in good agreement. This has been demonstrated for various cases of pairs of twisted flux ropes. Furthermore, the relaxation model has been successfully compared with a 23-flux-rope simulation, showing excellent agreement with the outcomes of numerical simulations by Hood *et al.* (2016).

The model is based on the concept that relaxation and energy release may be triggered by kink instability in a single unstable flux rope. This may trigger the release of stored magnetic energy from neighbouring magnetic threads which are stable. This scenario has important consequences for understanding how the solar corona is heated. The avalanche of heating will occur if the threads are sufficiently close together, but the exact conditions under which the avalanche proceeds (or stops) should be a topic of further investigations. What is important is that sometimes a large number of threads may release their energy, whilst in others, only one

or two threads release energy. Thus, a distribution of heating events, or "nano-flares", of different sizes, is expected. Furthermore, within an individual avalanche, the heating is bursty and time dependent. The relaxation model can easily predict the energy release, for given initial and onset conditions (number of threads merging, number of unstable threads and so on).

One challenge in applying relaxation models to the solar corona - as opposed to laboratory plasmas - is that solar coronal fields have no conducting walls and, thus, calculation of the relaxed state is a "free boundary problem" (Browning, 1988; Dixon *et al.*, 1989). We assume here that the final relaxed state has circular cross-section - which indeed appears to be the case in the numerical simulations. However, some means to predict the radius of this flux rope must be provided. We propose that this is determined by pressure balance at the boundary between the flux rope and ambient field, and calculate this both allowing for the increase in thermal pressure due to magnetic energy dissipation, and also without this effect (considering magnetic pressure only). One observation that warrants further investigation is the fact that the volume of the flux ropes is very well conserved when magnetic pressure is assumed to balance at the boundary. If it could be demonstrated that this applies more generally in all flux tube mergers, this would be an interesting result and provide simpler conditions for future analysis. In the case of a single unstable flux rope relaxmergeding, the final relaxed state has been shown to have somewhat larger radius - for a range of initial twist profiles, this has been shown to be typically approximately a factor of 1.2 times the initial radius (Bareford *et al.*, 2013). This is attributed to the unstable flux rope reconnecting with the surrounding axial field, an effect which we do not consider here. Future work is required to further investigate the factors that determine the radius of the final flux rope. Nevertheless, our predictions based on magnetic pressure balance are in good agreement with simulations. Relaxation in unbounded systems can also be interpreted as a localised relaxation (Bareford

et al., 2013), in which the relaxation extends over a limited region. Indeed, it is important to recall that Taylor theory predicts only the lowest energy state that could be attained, and that full relaxation may be not be achieved. For example, when the initial field has a braided structure, numerical simulations demonstrate that the final relaxed state consists of two parallel weakly twisted flux ropes, each of which approximately corresponds to a Taylor state, but which do not merge into the lower energy overall constant-α field (Pontin *et al.*, 2010). Furthermore, two flux ropes with opposite twist will release more energy if they relax than if the twists were in the same sense; but it is less likely that the relaxation will happen in this case, since the azimuthal fields at the interface between the ropes do not reverse. However, if one of the flux ropes is kink-unstable, the helical distortion may be sufficient to allow reconnection, although the reconnection may be slower in this case. Further investigations with 3D MHD simulations are required to determine the conditions under which twisted flux ropes merge into a Taylor state.

It is worth noting that a consequence of allowing relaxation over a localised region is that a current sheet (usually) must form between the relaxed field and the ambient axial field (Gimblett *et al.*, 2006; Bareford *et al.*, 2013). Indeed, there is evidence of such a reversed current layer in the 3D numerical simulations (Bareford *et al.*, 2013; Tam *et al.*, 2015; Hood *et al.*, 2016), although naturally the current layers in this case have finite width. In the case of multiple flux ropes, it appears that this current layer plays a role in the merger of adjacent threads as the avalanche proceeds (Hood *et al.*, 2016).

There are naturally some discrepancies between the outcomes of numerical simulations and the theoretical predictions. On the one hand, the simulated fields may not attain a fully relaxed state, as this depends on there being sufficient small-scale turbulence and reconnection throughout the volume to dissipate the free energy and

re-distribute the currents. Thus, the energy release predicted by relaxation theory is an upper bound on the actual energy release. The final state in the numerical simulations is still full of small scale current sheets, and the spatial distribution of α does not appear to be particularly constant. Nevertheless, the magnetic fields (which average over the small scale current structure) are relatively well represented by constant-α fields, and the final energy is even better approximated by the relaxed-state value, since small departures from a mimimum-energy state give quadratic deviations in energy. The predicted energy release also depends on the size of the relaxed flux tube. Our model seems to under-estimate this somewhat (particularly in the case of a single relaxing flux rope, as discussed above), and this effect causes the predicted energies to be lower than the actual values.

The successful development of this model could potentially pave the way for determining outputs of larger and more complex systems, allowing more realistic modelling (potentially) of Active Regions of the solar corona. This is because the Taylor model is not restricted by the number of ropes simulated, particularly due to the fact that the system is setup as a simple superposition in the case of multiple flux ropes. This allows for very rapid calculation times, regardless of system size. Thus, it would be easy to simulate large numbers of flux ropes, with variations in size, and twisted to different degrees (including the possibility of twists of opposing sign, which are readily accounted for in the relaxation model). In future, we propose to use further numerical simulations to devise simple 'rules' as to when flux ropes merge or not, and then to use these to simulate complex systems of flux ropes.

Chapter 8

Magnetohydrodynamic Simulations of Twisted Magnetic Flux Ropes

8.1 Introduction

The coronal heating problem, as defined within Klimchuk (2015), involves understanding how the corona achieves the high temperatures it does compared to the chromosphere. A postulated mechanism for this is the twisting of footpoints in the chromosphere that result in a "charging" up of the coronal loops that then relax to heat the corona. Priest and Cowley (1975); Browning and Van der Linden (2003), postulated that a mechanism for this to occur would be the ideal kink instability in a single magnetic flux rope. This could trigger an avalanche effect that then results in enhanced coronal heating. Such a mechanism was suggested in previous studies that suggested a cellular automaton model, and was proven in a simulation by Hood *et al.* (2016).

8.2 Approach and Methodology

Following the development of a relaxation model (Hussain *et al.*, 2017), it is clear that the a relaxation model with a magnetic pressure constraint is a good approximation to results of MHD simulations that involve multiple interacting flux ropes which evolve following a kink instability (Tam *et al.*, 2015; Hood *et al.*, 2009, 2016). However, it is noted that relaxation is blind to the physical process of whether or not flux ropes undergo merger or relaxation. For an individual flux rope, the trigger for relaxation is clear, i.e. kink instability will force the flux rope to acquire a minimum energy state. However there are questions as to whether this flux rope will trigger a stable flux rope to also undergo relaxation and (as a result) a merger. As a result of analysis and simulation, we have developed a few fundamental questions regarding merging flux ropes that we hope to comment on using MHD simulations. These questions are as follows: 1) What is the maximum distance under which an unstable flux rope will interact with a stable flux rope to result in relaxation and merger? 2) Is there a minimum threshold for the twist of a stable flux rope below which it will not be triggered by a kink unstable flux rope? 3) How long does the relaxation process take? 4) At what point in an avalanche will the relaxation process no longer occur? To answer these questions, a series of MHD simulations were carried out. These all involved two flux ropes with varying centres and twist parameters. The MHD simulations in general operate in the following conditions. The MHD systems of equations, solved in the code Lare3d (Arber *et al.*, 2001) are given as:

$$\frac{\partial \rho}{\partial t} = -\nabla.(\rho v) \tag{8.1}$$

$$\frac{\partial}{\partial t}(\rho v) = -\nabla.(\rho v v) + 1/\mu_0(\nabla \times B) \times B - \nabla P + \nabla.S \tag{8.2}$$

$$\frac{\partial B}{\partial t} = \nabla \times (v \times B) - \nabla \times (\eta(\nabla \times B)/\mu_0) \tag{8.3}$$

$$\frac{\partial}{\partial t}(\rho) = \nabla.(\rho v) - P\nabla.v + \eta j^2 + Q_{visc} \tag{8.4}$$

Where ρ is the mass density, v, B, S, j are the velocity, magnetic, stress tensor, and current vectors, η is the anomalous resistivity, and Q is the viscous heating. Lare3D is a Lagrangian remap code (Caramana *et al.*, 1998; Owen and Shashkov, 2014) and works by solving the equations of MHD on a staggered grid for multiple time steps. The time step as a non dimsionalised function of the Alfven time.

The simulations simulate two magnetic flux ropes which are defined by the following:

$$B_\theta = B_0 \lambda r (1 - r^2)^3 \tag{8.5}$$

$$B_z = B_0 \sqrt{(1 - \frac{\lambda^2}{7} + \frac{\lambda^2}{7}(1 - r^2)^7 - \lambda^2 r^2 (1 - r^2)^6)} \tag{8.6}$$

The field is a force free field where the λ is the twist parameter. It was originally developed by Hood and Priest (1979) when investigating the ideal threshold for the ideal kink instability. In this case and field, the kink instability is $\lambda_{crit} = 1.586$ and the maximum twist possible is $\lambda_{max} = 2.438$ since we have a condition that the field must be real.

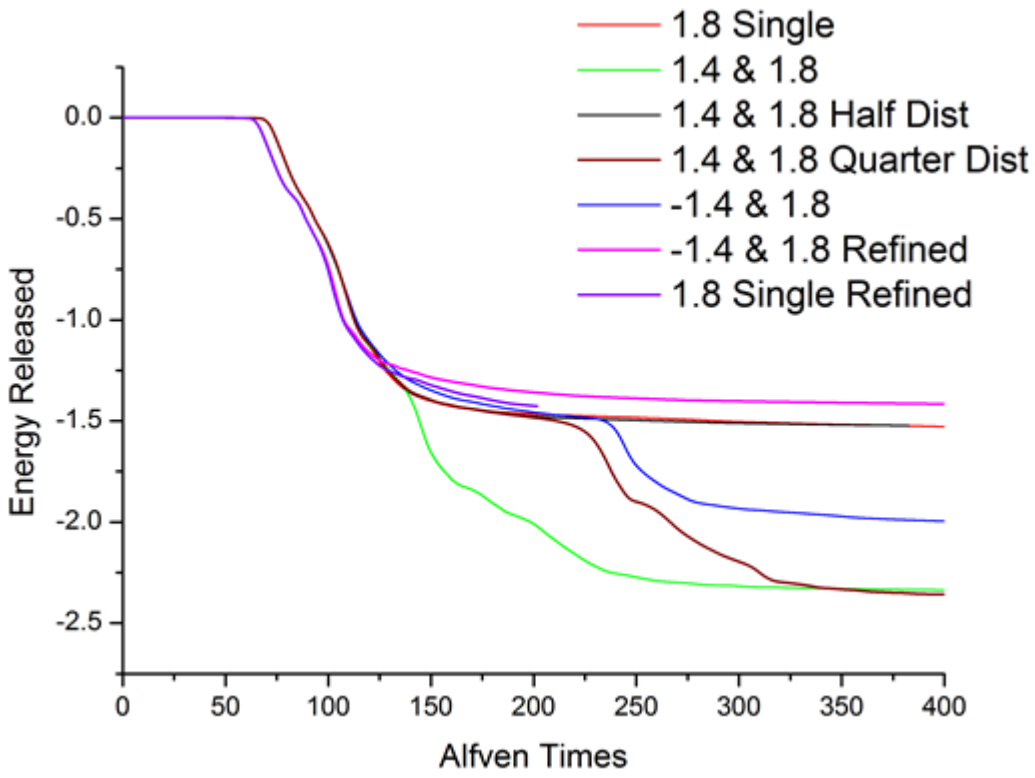

Figure 8.1: Energy (dimensionless) output from flux rope simulations. The lines show various simulations. In situations of two flux ropes, two λ(twist) parameters are given. In situations where the flux rope is reversed, a minus sign is used. Half distance and quarter distance refer to 0.5 units and 0.25 units of separation between the edge of the flux ropes (normalised to Alfven wavelength). but probably interesting

Figure 8.1 shows the various simulations that were done for this investigation. The 1.4 & 1.8 curve is the same simulation as done in Tam *et al.* (2015) and shows that a kink unstable flux rope causes the relaxation (and merges with) a neighbouring stable flux rope. Subsequently, simulations were done by setting the edges apart by 0.25 units and 0.5 units. Simulations were also done with a reverse twist since extending the simulations of Hood *et al.* (2016) show that the reversed flux ropes might also relax. Single kink unstable flux ropes are also done for reference.

8.3 Maximum Separation

With regards to the minimum distance required to cause a stable flux rope to undergo relaxation, three simulations were carried out with two flux ropes. All of these involved one stable flux rope ($\lambda = 1.4$) and one kink unstable flux rope ($\lambda = 1.8$) with the difference being the separation between these. The simulations are dimensionless. The distance between the origins of the two flux ropes are 1) 1 unit, 2) 1.25 units, and 3) 1.5 units. Therefore, in the first kind the edges of the ropes touch each other, in the second they are 0.25 units apart, and in the third they are 0.5 units apart. We observe that simulations 1 and 2 result in the stable flux rope relaxing and merging but simulation 3 only results in the unstable flux rope undergoing relaxation on its own. Therefore, we state that the maximum distance is somewhere between 0.25 and 0.5 units.

Furthermore, as can be seen from Figure 8.1, the time at which the merger occurs is directly affected by the distance. Simulation 1 (1.4 & 1.8, green line) shows no clear distinction between relaxation of the unstable flux rope and stable. However, with the quarter distance (1.4 & 1.8 quarter dist, burgundy), this is triggered approximately 150 Alfven times after the initial relaxation process. The half distance shows that there is no clear drop in energy showing that the stable flux rope does not undergo relaxation.

8.4 Twist in Stable Flux Rope

Simulations showed that stable flux ropes as low as $\lambda = 0.6$ did undergo relaxation. Since this is very low twist and does not yield an excessively large free energy, we did not lower the twist any further.

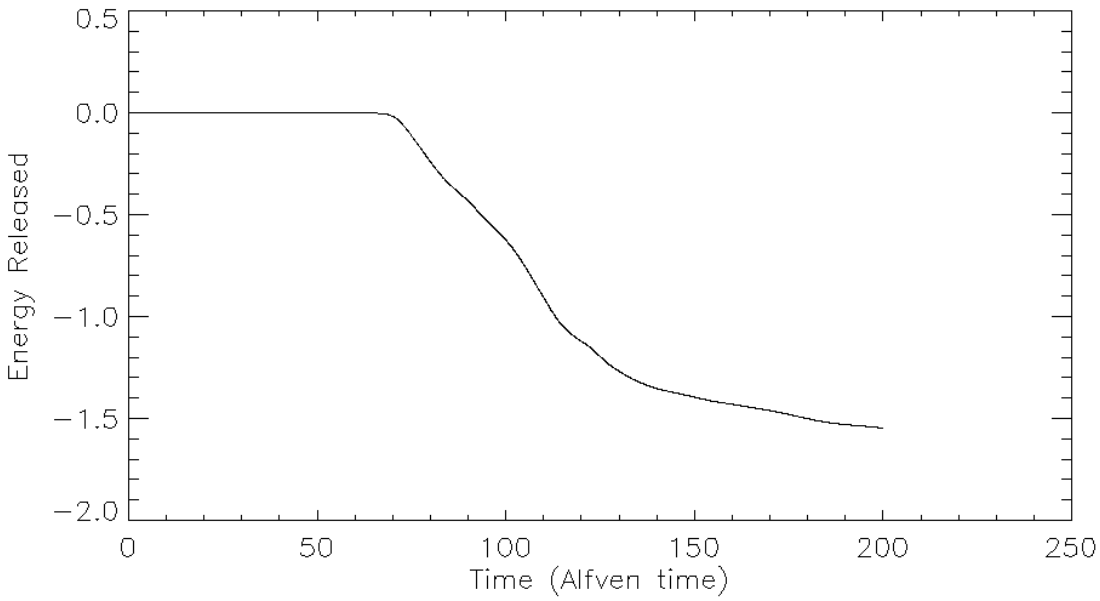

Figure 8.2: Simulation of two merging flux ropes: $\lambda_1 = 0.6$ and $\lambda_2 = 1.8$

8.5 Reverse Twist

As a result of extending the avalanche (Hood *et al.*, 2016), it was observed that the simulations with reversed flux ropes underwent relaxation (A. W. Hood, Private Communication). However, given the nature of Lare3D, there was a suspicion that this was a result of numerical errors since the effect was observed sufficiently late into the simulation. Therefore, in order to investigate this, a two flux rope simulation was done with a reversed stable flux rope next to a kink unstable flux rope (Figure 8.3). In one of the simulations done, a merger was observed while not in an identical second simulation. Therefore, it was suspected that this was a numerical error. It was confirmed when the simulation was repeated with a refined mesh, which confirmed no merger of the two flux ropes. We are confident that the normal results do not have this problem since they match previous results (Tam *et al.*, 2015) as well as being in line with expectation.

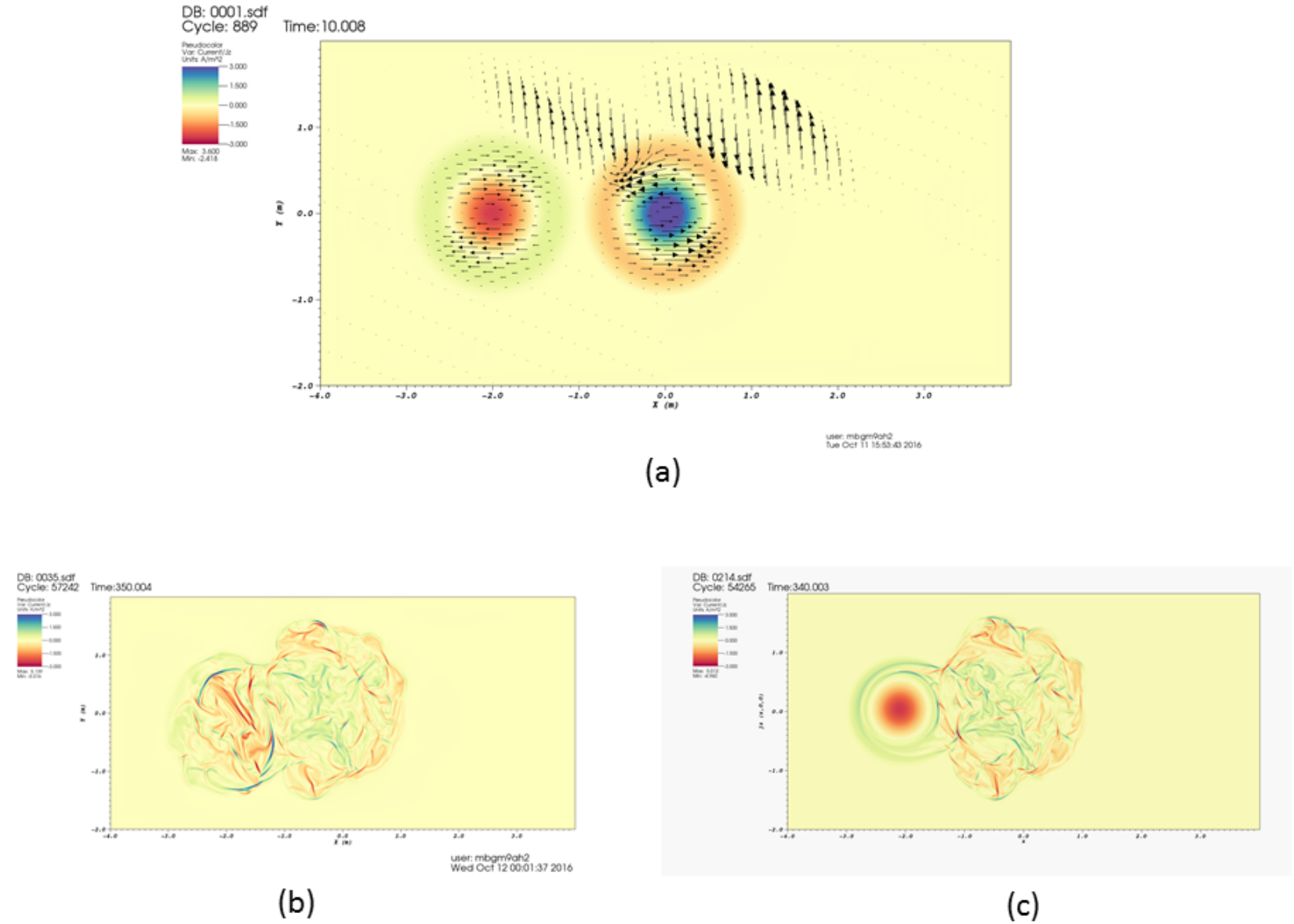

Figure 8.3: Simulations of two flux ropes with one single reversed rope (left). (a) depicts the initial setup, (b) depicts the merger that was observed, and (c) depicts the lack of merger after refining the mesh.The vectors show the tiwst of the flux ropes.

8.6 Relaxation Trigger

Considering an avalanche model that was first shown in Hood *et al.* (2016), the authors show that a single unstable flux rope can cause an avalanche of energy release. The simulation shows that a stable flux rope can cause relaxation in up to 17 flux ropes, within a grid of 23 tightly packed flux ropes. Within Hussain *et al.* (2017), we observed that the relaxation parameter for the force free field in an avalanche appears to have an exponential decay as one increases the number of stable flux ropes merged to the final relaxed state as shown in Figure 8.4.

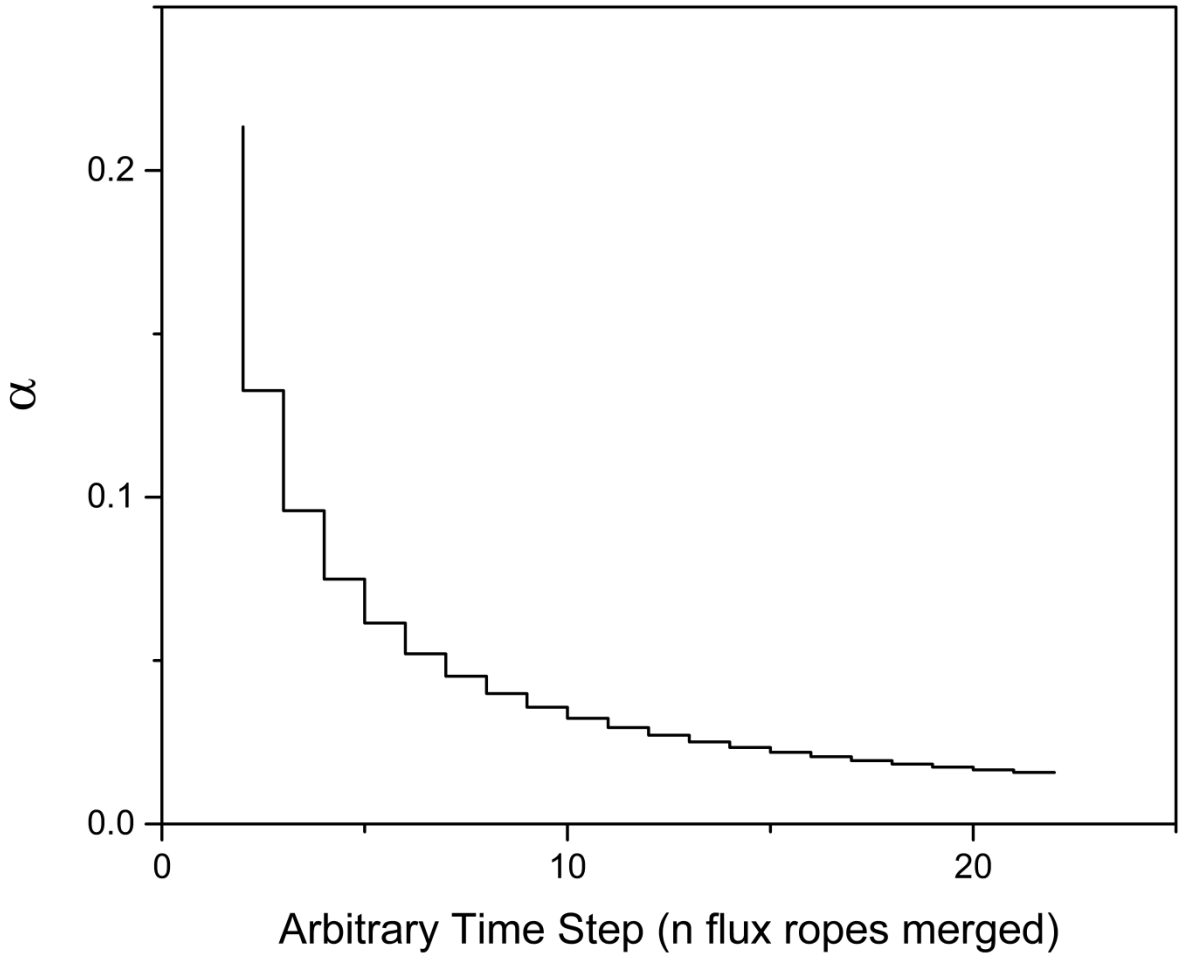

Figure 8.4: Relaxation alpha with number of flux ropes merged

Relaxation analysis is blind to when should stable flux ropes no longer merge. How-

ever, the relaxation parameter is directly correlated to the current since it is a force free field. T but probably interestinghe relaxed field is of the Bessel form (Taylor, 1974):

$$B_\theta = B_1 J_1(\alpha r)$$

$$B_z = B_1 J_0(\alpha r)$$

$$\nabla \times B = \alpha B$$

In order to investigate this effect, we try and observe the current at the edge of the stable flux rope. We commence by observing the current at the edge of the stable flux rope in the quarter distance simulation. We do this by measuring the magnitude of the current along the line [-1.25, 0, -10] to [-1.25, 0, 10] (Figure 8.5). As one can observe, there are spikes of magnitude greater than 5. A similar line out for the half distance simulation ([-1.5, 0, -10] to [-1.5, 0, 10] and Figure 8.6) is shown to compare. We occasionally observe that the spikes within the quarter distance simulation reach over 5 (which is when anomalous resistivity is triggered) suggesting that there may be resistive instabilities.

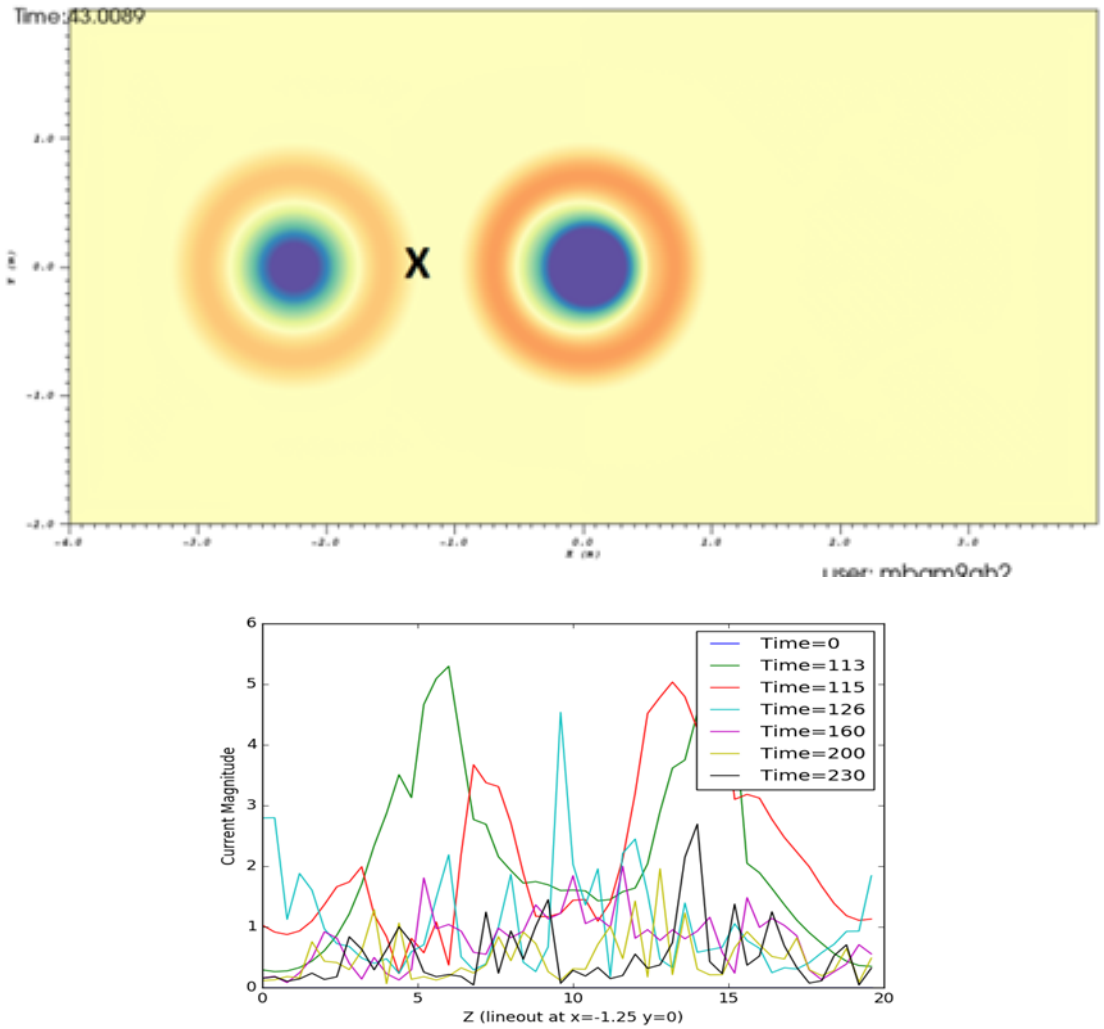

Figure 8.5: Simulation of two merging flux ropes 0.25 units apart depicting a line out of current magnitude on the edge of the stable magnetic flux rope (marked with X).

The images (Figure 8.5) show that for the simulation where there is no separation, the current seems to average at 2 units throughout the simulation. When compared to the results for the half distance (Figure 8.6), we only see spikes on occasion but not a consistent current value that also appears very late into the simulation.

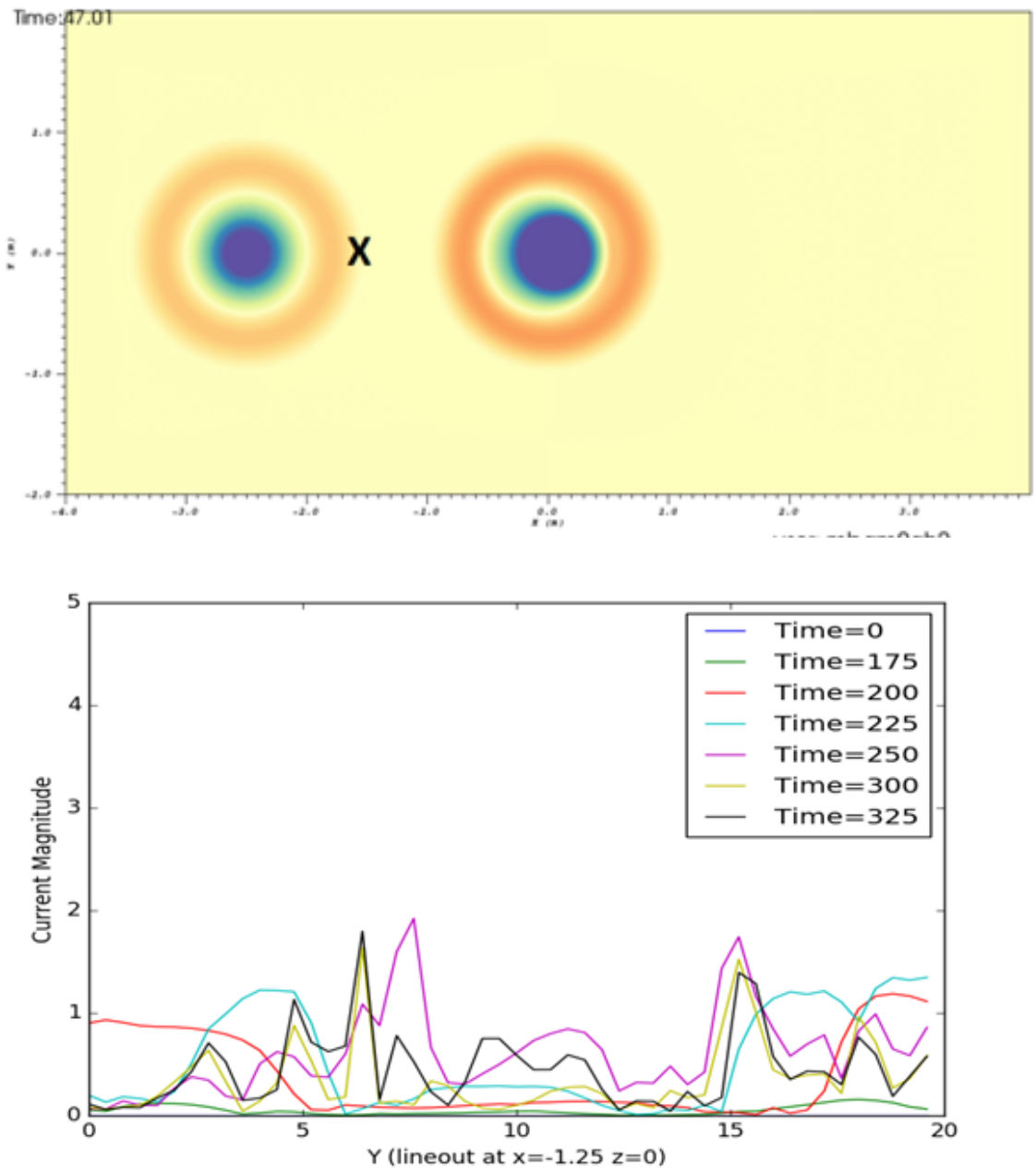

Figure 8.6: Simulation of two merging flux ropes 0.5 units apart depicting a line out of current magnitude on the edge of the stable magnetic flux rope (marked with X).

Another effect noticed is that of a magnetic wave that is produced as the kink unstable flux rope undergoes relaxation. This is observed within the 0.5 distance simulation by observing the magnetic field (B_x) along a line midway between the

two flux ropes (line out depicted in Figure 8.7). The graphs suggest the presence of a wave. Taking the Fourier transform of B_x at the point [0.3, 0, 0] (Figure 8.8) over all time steps also suggests that there is a wave present. However, further work needs to be done to properly confirm since the sharp peaks in the graphs could suggest an under resolved mesh. Furthermore, the wave needs to be classified (longitudnal, torsional, etc) aswell.

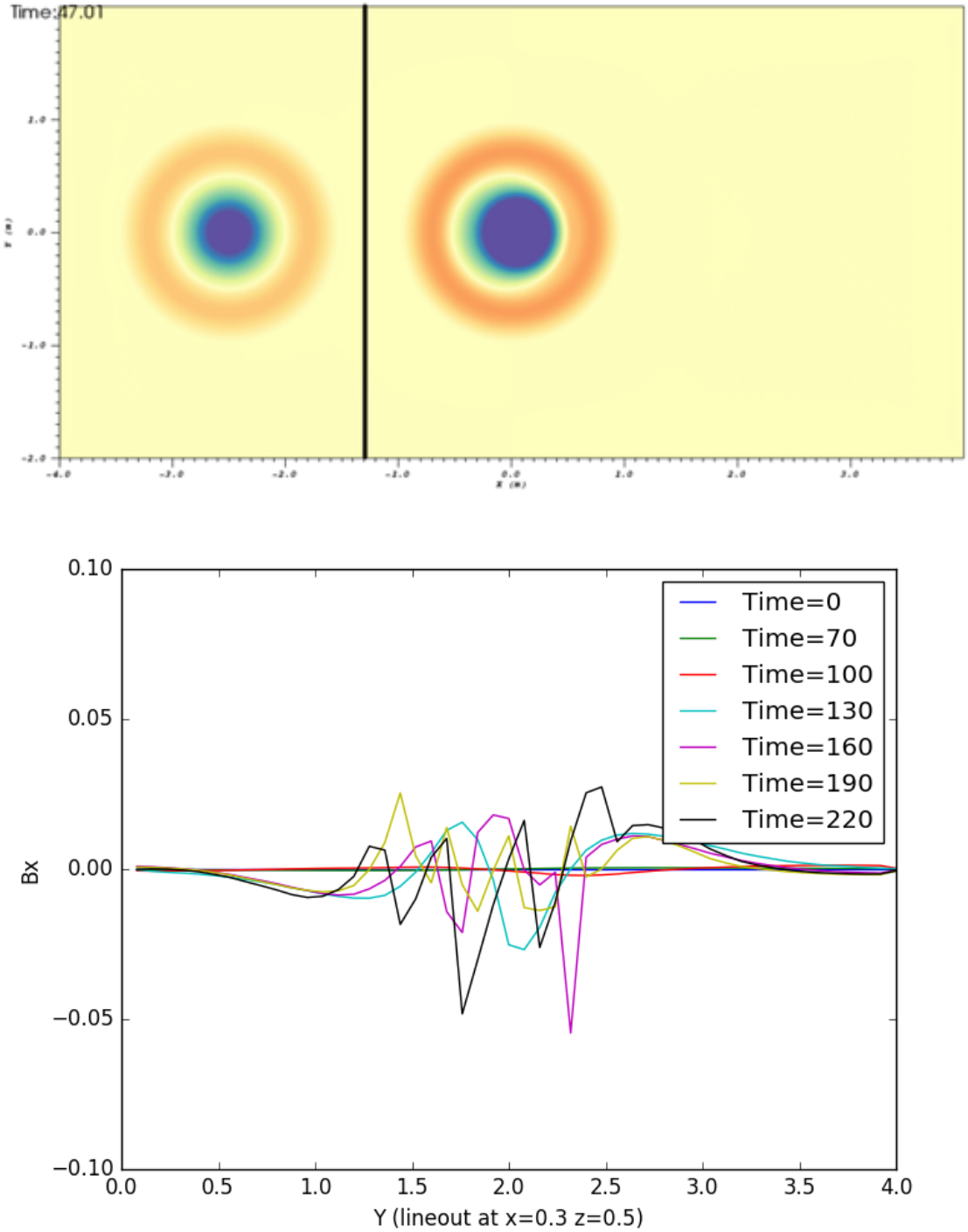

Figure 8.7: $B_x$line out at $x = 0.3$

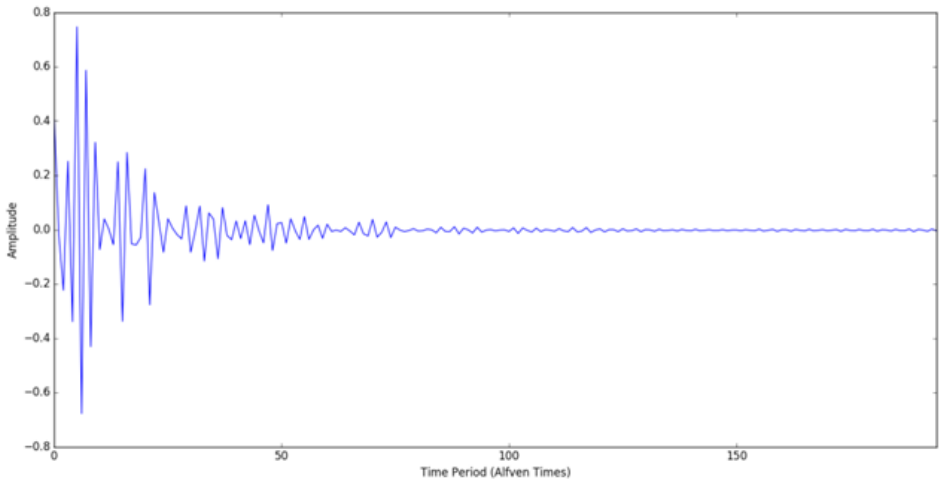

Figure 8.8: Fourier transform of B_x at [0.3, 0, 0] across all time steps.

Part III

Effect of Plasma Instabilities on Fusion Materials

Chapter 9

Applying an Edge Localised Mode Relaxation Model for Damage in Fusion Relevant Tungsten

The previous sections of this thesis describe essentially two separate strands of work. Here, we present some preliminary suggestions for how these two approaches (plasma-material interactions and relaxation theory) could be brought together, in order to understand the effect of Edge Localized Modes in Tokamak plasmas on the walls.

Edge localised modes or ELMs are pressure driven instabilities within the plasma (Connor *et al.*, 1998, 2008). They are seen to exist under a confinement condition called H-mode (for high confinement as opposed to L-mode). H-mode confinement times are typically double that of L-mode (Stangeby, 2000). Initially it was found that heating the plasma would reduce the confinement time until it was heated up to a certain threshold. This however comes with the trade-off that the build up of energy drives instabilities that is released through the edge of the plasma (therefore

on the plasma facing surface). It is a periodic disturbance classed from Type I (high energy, low frequency) to Type III (low energy, high frequency). Type II ELMs are expected for Tokamak operation in H-mode for Tokamaks such as ITER and DEMO since completely eliminating them would have the consequence of massive pressure build up.

The mode of operation for ELMs can be seen in the illustration of pressure versus the position along the chamber where it can be seen the pressure build-up collapses under an ELM operation (Figure 9.1).

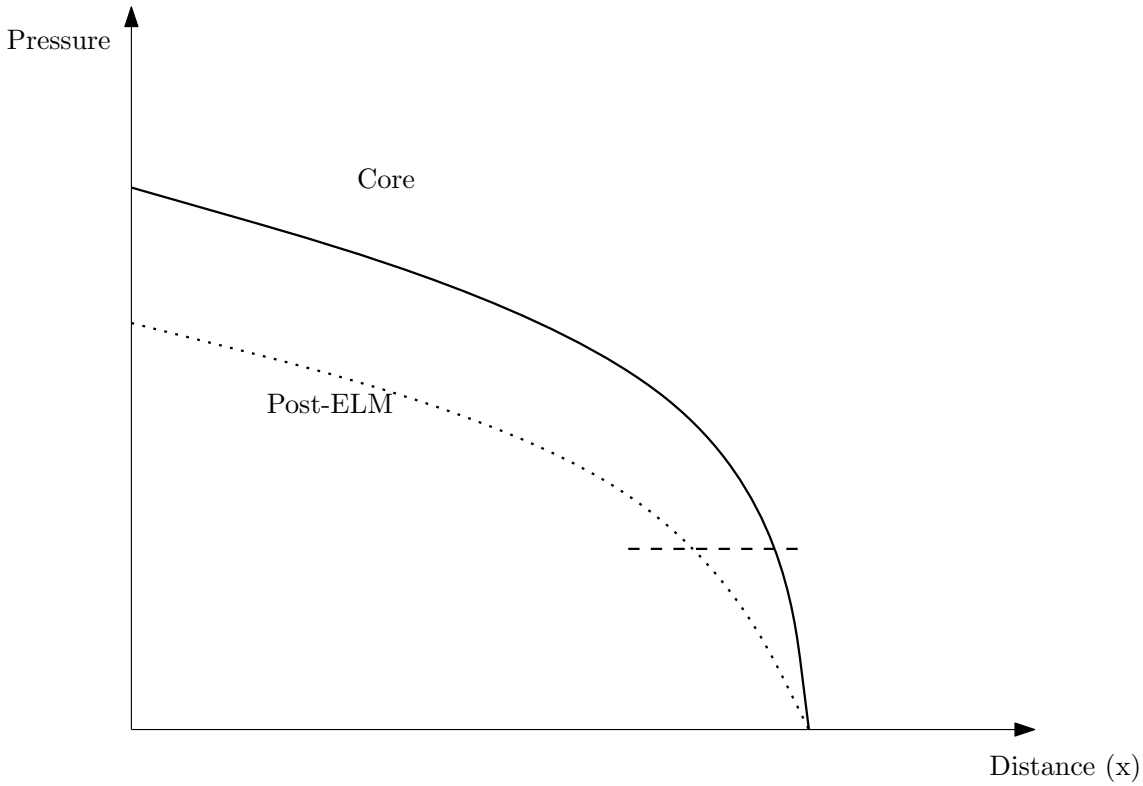

Figure 9.1: Plot of plasma pressure against position(Maggi *et al.*, 2014)

The principle can be illustrated through the concept of potential energy. One can form a functional form of the potential energy by stating that:

$$\frac{d}{dt}W = \int F.v.dV, \tag{9.1}$$

which is the power Equationtion where W is the work done, F is the force, v is the velocity and V is the volume phase. Therefore, we can approach this and having an appropriate Equationtion for the force and the work, can obtain a functional form equilibrium situation. Such a Equationtion is provided in Connor *et al.*, 1998. Aside from energy dissipation, ELMs could be useful for dispersion of impurities. However, with such a sudden burst of energy and impurities, these are likely to make a heavy impact on the materials that will eventually be used to construct fusion reactors. The dangers of the instabilities was mentioned in works such as Wirth *et al.* (2011).

A study conducted on the Joint European Torus (JET) (Harder *et al.*, 2016) showed a difference within the inter-ELM and intra-ELM phases of operation. It can be fairly assumed that this effect is likely to be larger since the aim of the fusion community is to build a steady-state fusion reactor. It may be that the effects could be mitigated due to the increased surface area. However, since this would need to be properly assessed, there is sufficient motivation to develop a model that can assess the outcome. We propose a relaxation model that, coupled with material sputtering theory, could provide a simple analytical model to determine the extent of the effect as well as investigate the result of various variables. Furthermore, we propose molecular dynamic simulations of sputtering that would be able to take into account the effect of neutron damage which could be used in conjunction with recent work (Gilbert *et al.*, 2015, Hussain et al.,2017 - in prep) that show the spectrum of primary events. A sample setup is shown in Figure 9.2.

Helicity conserving relaxation was originally developed within the works of Taylor (1974, 1986), which developed the model for Reverse Field Pinch experiments (RFP). Within this work, it was proposed that the energy of a plasma tube approaches a minimum energy state whilst conserving helicity. Thus, the functional to minimised, and the associated contraint are:

$$\delta W = \int_V \boldsymbol{B}^2 dV, \tag{9.2}$$

$$K = \int_V \boldsymbol{A}.\boldsymbol{B} dV, \tag{9.3}$$

Where $\boldsymbol{A}$ is the vector potential of the magnetic field, $\boldsymbol{B}$ and K is the helicity. Within RFP, the final resulting magnetic field is the force free field which is the solution of:

$$\nabla \times \boldsymbol{B} = \mu \boldsymbol{B}, \tag{9.4}$$

where μ is a scalar constant. It should be noted that the derivation has been successfully applied to various scenarios such as Bevir *et al.* (1985); Gimblett *et al.* (2006) which apply the analysis for toroidal devices and Bareford and Browning (2015); Hussain *et al.* (2017) which apply it to coronal loops. This suggests the versatility of the method and the strength of the physical principles involved.

Gimblett *et al.* (2006) derived that the energy released as a result of an ELM event is given by the equation:

$$-\delta W = \Delta_a(\Delta_a \Delta_a' + I_a) + \kappa_a[(\kappa_a - 2\Delta_a)(\Delta_a' + m - 1) + 2\frac{n}{m} - I_a], \tag{9.5}$$

where a is the minor radius of the Tokamak, κ_i is the skin current density at location i (therefore κ_a is the edge skin current density), Δ_i is a characteristic dimensionless distance depicting the distance from i to the the resonant surface, I_i is the toroidal current density, n is the toroidal wave number, and m is the poloidal wave number.

Once an energy output for a given configuration is obtained one can apply this to a given number of particles impacting the surface. An estimate for this could be obtained by fixing a temperature T for the system and then using a kinetic analysis. Subsequently, the number of particles eroded can be considered by using either SRIM or molecular dynamic simulations, which can be setup as depicted in Figure 9.2.

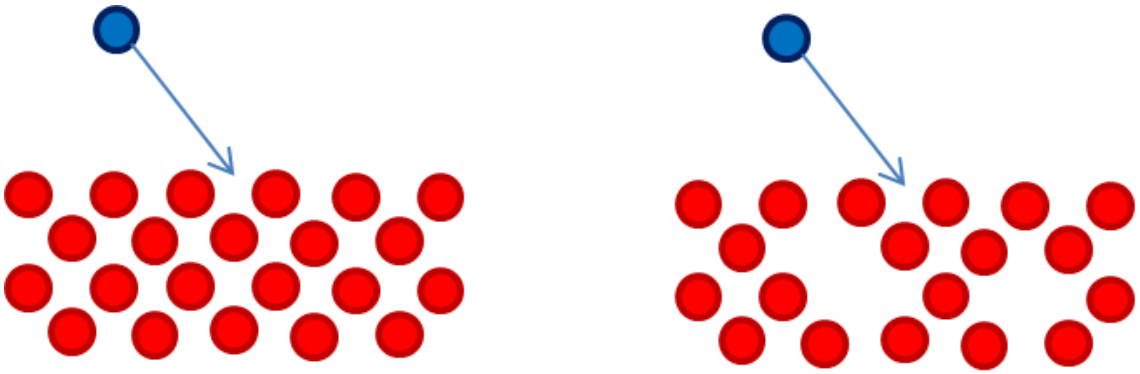

Figure 9.2: Molecular dynamics simulation setup for sputtering of continuous and damaged samples.

Part IV

Concluding Statements

Chapter 10

Summary of Work

Three fundamental pieces of work were done within the first part (synergistic effects of plasma and neutrons on materials in fusion reactors). These were, neutron transport in a slab geometry, neutron transport in a spherical shell geometry, and molecular dyanmics investigations.

Firstly, an investigation into neutron transport behaviour within a slab geometry was carried out. The specific aim of this was to determine how 14 MeV neutrons affected the surface of a material. The surface was defined as 20 micrometres. This length was chosen as the right scale for commenting on the effects of plasma damage synergistically interacting with neutron damage. The surface damage turned out to be negligible due to the high mean free path of 14 MeV neutrons. Furthermore, any damage caused in the surface was due to backscatters.

Given the significance of backscatters, it was deemed that an investigation to this effect must be carried out. To this end, a geometry consisting of a hollow tungsten shell surrounded by a homogenous steel-water mix was employed in a neutron transport simulation. This showed damage within the surface. However, it also

showed that the nature of the damage at the surface was significantly different to the nature of damage further on. This is because of the average primary knock on energy increasing with depth, in contrast to the frequency of these events decreasing. This effectively results in an exponentially decaying damage trend with a constant damage at the surface.

A natural consquence of this was to commence an investigation that characterises neutron damage cascades as individual primary events. This was done using molecular dynamics. The aim here was to provide reasonable descriptions that could be used to generate cascades as well as examine how behaviour varies with change in energy and direction of primary knock-ons. The work used eigenvector analysis to determine principle axis of cascades and provided reasonable statistical descriptions. Fits were done to the skewed normal distribution and results provided However, the work is very much in its infancy.

Within the first part of the thesis, it has been shown that the matter of neutron damage cannot be simply taken as a function of damage. Neutron damage has subtleties; for instance, it is affected by geometry and by the initial setup. Furthermore, the understanding of how primary events result in damage is still unclear. However, within this thesis, we have managed to show methods that could be used to provide good setup for future experiments. Furthermore, it has also been shown that the issue of synergistic effects of plasma and 14 MeV neutrons may not be as worrying since it is the back scatters that are far more important to the issue of surface damage.

The second part (relaxation of merging magnetic flux ropes in fusion and solar plasmas) focussed on developing analytical models for energy released due to various instabilities using relaxation theory.

Firstly, a helicity conserving relaxation model was developed for coronal loops which

found good agreement with simulations of two merging flux ropes as well as an avalanche model. This method was powerful enough to be able to use it for expanding the parameter space (something which cannot be easily done using simulations due to computational expense). It was also found that the relaxation of cylindrical flux tubes resulted in a final state that conserved volume. Reasons for exactly why are unclear and warrant further investigation.

Relaxation theory, being an analytical method, is blind to the physical possibility of a flux rope relaxing. Therefore MHD simulations were conducted which found that the distance between interacting flux ropes and the level of critical current on the edge of a flux rope are key factors in determining whether relaxation is likely to happen. To develop a large scale model, work needs to be done on determining ideal magnetohydrodynamic stability as a function of aspect ratio.

Overall, a model has been developed for calculating the energy release in multiple interacting flux ropes. The accuracy and ease of use has been shown to be satisfactory which makes it a candidate for being able to use on larger scales. We have also managed to narrow down the physics about the conditions under which mergers and relaxation will occur in the avalanche process.

Chapter 11

Future Work

The following is planned as future work:

- Development of damage profiles for shell geometry neutronics analysis,
- Further comparison of D Mason potential to Juslin Wirth potential and investigation of reliability,
- Development of object kinetic monte carlo (OKMC) simulations of neutron damage and then introduce plasma damage within these for slab and shell geometries,
- Create algorithm for determining parameters for using ions as a proxy for neutron damaged surfaces,
- Investigation of stability criterion for kink unstable flux ropes,
- Investigate nature of possible wave in merging flux ropes,
- Development of a Monte Carlo large scale model for multiple interacting flux ropes using relaxation modelling,

- Development of model for ELM erosion of first wall materials in fusion reactors.

References

Abromeit, C., oct 1994. Aspects of simulation of neutron damage by ion irradiation. Journal of Nuclear Materials 216, 78–96.

Arber, T. D., Longbottom, A. W., Gerrard, C. L., Milne, A. M., 2001. A staggered grid, Lagrangian-Eulerian remap code for 3-D MHD simulations. Journal of Computational Physics 171, 151–181.

Asgari-Targhi, M., van Ballegooijen, A. A., Cranmer, S. R., DeLuca, E. E., 2013. The spatial and temporal dependence of coronal heating by Alfven wave turbulence. The Astrophysical Journal 773 (2), 111.

Aymar, R., 2001. Summary of the ITER final design report.

Barabash, V., Federici, G., Linke, J., Wu, C. H., mar 2003. Material/plasma surface interaction issues following neutron damage. Journal of Nuclear Materials 313-316, 42–51.

Bareford, M. R., Browning, P. K., 2015. Energy release in driven twisted coronal loops (June), 1–22.

Bareford, M. R., Browning, P. K., Van der Linden, R. A. M., 2011. The Flare-Energy Distributions Generated by Kink-Unstable Ensembles of Zero-Net-Current Coronal Loops. Solar Physics 273 (1), 93–115.

Bareford, M. R., Hood, a. W., Browning, P. K., 2013. Coronal heating by the partial relaxation of twisted loops. Astronomy and Astrophysics 550.

Baty, H.; Heyvaerts, J., 1996. Electric current concentration and kink instability in line-tied coronal loops. Astronomy & Astrophysics 308.

Becquart, C. S., Domain, C., Sarkar, U., Debacker, A., Hou, M., 2010. Microstructural evolution of irradiated tungsten: Ab initio parameterisation of an OKMC model. Journal of Nuclear Materials 403 (1-3), 75–88.

Belloni, F., Calviani, M., Colonna, N., Mastinu, P., Milazzo, P. M., Abbondanno, U., Aerts, G., Alvarez, H., Alvarez-Velarde, F., Andriamonje, S., Andrzejewski, J., Audouin, L., Badurek, G., Barbagallo, M., Baumann, P., Becvar, F., Berthoumieux, E., Calvino, F., Cano-Ott, D., Capote, R., Carrapico, C., Cennini, P., Chepel, V., Chiaveri, E., Cortes, G., Couture, A., Cox, J., Dahlfors, M., David, S., Dillmann, I., Domingo-Pardo, C., Dridi, W., Duran, I., Eleftheriadis, C., Embid-Segura, M., Ferrari, A., Ferreira-Marques, R., Fujii, K., Furman, W., Goncalves, I., Gonzalez-Romero, E., Goverdovski, A., Gramegna, F., Guerrero, C., Gunsing, F., Haas, B., Haight, R., Heil, M., Herrera-Martinez, A., Igashira, M., Jericha, E., Kappeler, F., Kadi, Y., Karadimos, D., Karamanis, D., Kerveno, M., Koehler, P., Kossionides, E., Krticka, M., Lamboudis, C., Leeb, H., Lindote, A., Lopes, I., Lozano, M., Lukic, S., Marganiec, J., Marrone, S., Martínez, T., Massimi, C., Meaze, M. H., Mengoni, A., Moreau, C., Mosconi, M., Neves, F., Oberhummer, H., O Brien, S., Papachristodoulou, C., Papadopoulos, C., Paradela, C., Patronis, N., Pavlik, A., Pavlopoulos, P., Perrot, L., Pigni, M. T., Plag, R., Plompen, A., Plukis, A., Poch, A., Praena, J., Pretel, C., Quesada, J., Rauscher, T., Reifarth, R., Rosetti, M., Rubbia, C., Rudolf, G., Rullhusen, P., Salgado, J., Santos, C., Sarchiapone, L., Savvidis, I., Stephan, C., Tagliente, G., Tain, J. L., Tarrio, D., Tassan-Got, L., Tavora, L., Terlizzi, R., Vannini, G., Vaz, P., Ventura, A., Vil-

lamarin, D., Vincente, M. C., Vlachoudis, V., Vlastou, R., Voss, F., Walter, S., Wiescher, M., Wisshak, K., jan 2013. Measurement of the neutron-induced fission cross-section of 241Am at the time-of-flight facility n_TOF. The European Physical Journal A 49 (1), 2.

Bevir, M. K., Gimblett, C. G., Miller, G., 1985. Quasi-steady-state toroidal discharges. Physics of Fluids 28 (6), 1826.

Bhattacharjee, A., 2004. Impulsive Magnetic Reconnection in the Earth's Magnetotail and the Solar Corona. Annual Review of Astronomy and Astrophysics 42 (1), 365–384.

Biersack, J. P., Eckstein, W., 1984. Sputtering studies with the Monte Carlo Program TRIM.SP. Applied Physics A Solids and Surfaces 34, 73–94.

Biskamp, D., 1984. Magnetic reconnection across an x-type neutral point slow shocks versus current sheets.

Biskamp, D., 1997. Collisional and collisionless magnetic reconnection. Physics of Plasmas (1994-present) 4 (5), 1964.

Boozer, a. H., 1986. Ohm's law for mean magnetic fields. Journal of Plasma Physics 35 (01), 133.

Borchardt-Ott, W., 2012. Crystallography.

Browning, P. K., 1988. Helicity injection and relaxation in a solar-coronal magnetic loop with a free surface. Journal of Plasma Physics 40, 263 – 80.

Browning, P. K., Cardnell, S., Evans, M., Lucini, F. A., Lukin, V. S., McClements, K. G., Stanier, A., jul 2015. Two-fluid and magnetohydrodynamic modelling of magnetic reconnection in the MAST spherical tokamak and the solar corona. Plasma Physics and Controlled Fusion 014041, 14041.

Browning, P. K., Gerrard, C., Hood, A. W., Kevis, R., Van der Linden, R. A. M., jul 2008. Heating the corona by nanoflares: simulations of energy release triggered by a kink instability. Astronomy and Astrophysics 485 (3), 837–848.

Browning, P. K., Stanier, A., Ashworth, G., McClements, K. G., Lukin, V. S., 2014. Self-organization during spherical torus formation by flux rope merging in the Mega Ampere Spherical Tokamak. Plasma Physics and Controlled Fusion 56 (6), 64009.

Browning, P. K., Van der Linden, R. A. M., 2003. Solar coronal heating by relaxation events. Astronomy {&} Astrophysics 400 (1), 355–367.

Caramana, E. J., Burton, D. E., Shashkov, M. J., Whalen, P. P., 1998. The Construction of Compatible Hydrodynamics Algorithms Utilizing Conservation of Total Energy. Journal of Computational Physics 146 (1), 227–262.

Cengel, Y. A., Boles, M. A., 2013. Thermodynamics An Engineering Approach. Vol. 53.

Charbonneau, P., McIntosh, S. W., Liu, H. L., Bogdan, T. J., Charbonneau, P., McIntosh, S. W., Liu, H.-L., Bogdan, T. J., Charbonneau, P., McIntosh, S. W., Liu, H. L., Bogdan, T. J., 2001. Avalanche models for solar flares (Invited review). Solar Physics 203 (2), 321–353.

Clark, R. E. H., Behrisch, R., Gilbody, H. B., Janev, R., Kingston, A., Martynenko, Y. V., Menapace, E., Miyahara, A., Schultz, D. R., Summers, H. P., Kato, T., Roth, J., Wiese, W., 2001. Atomic and plasma-material interaction data for fusion. Vol. 7. International Atomic Energy Agency.

Connor, J. W., Hastie, R. J., Wilson, H. R., Miller, R. L., 1998. Magnetohydrodynamic stability of tokamak edge plasmas. Physics of Plasmas 5 (7), 2687.

Connor, J. W., Kirk, A., Wilson, H. R., Benkadda, S., 2008. Edge localised modes (ELMs): Experiments and theory. AIP Conference ..., 174–190.

Cottrell, G. A., Pampin, R., Taylor, N. P., 2006. Tungsten armour in fusion power plants. Fusion Science and Technology 50 (July).

Dahlburg, R. B., Dahlburg, J. P., Mariska, J. T., 1988. Helical magnetohydrodynamic turbulence and the coronal heating problem 198, 300–310.

Daw, M. S., Foiles, S. M., Baskes, M. I., Laboratories, S. N., Daw, M. S., Foiles, S. M., Baskes, M. I., 1993. The embedded-atom method: a review of theory and applications. Materials Science Reports 9 (September 1992), 251–310.

De Backer, A., Sand, A., Ortiz, C. J., Domain, C., Olsson, P., Berthod, E., Becquart, C. S., 2016. Primary damage in tungsten using the binary collision approximation, molecular dynamic simulations and the density functional theory. Physica Scripta T167 (T167), 014018.

De Moortel, I., Browning, P., Moortel, I. D., Browning, P., 2015. Recent advances in coronal heating. Philosophical Transactions of the Royal Society A: Mathematical, Physical and Engineering Sciences 373 (2042), 20140269–20140269.

De Temmerman, G., 2000. Plasma-wall coupling (presentation at DIFFER Energy Days).

Delzanno, G. L., Evstatiev, E. G., Finn, J. M., 2007. Line-tied kink modes in cylindrical equilibria with magnetic shear. Physics of Plasmas 14 (7).

Dixon, A. M., Berger, M. A., Browning, P. K., Priest, E. R., 1989. A generalization of the Woltjer minimum-energy principle. Astronomy & Astrophysics 225 (1), 156–166.

Doerner, R. P., Baldwin, M. J., Stangeby, P. C., apr 2011. An equilibrium model for tungsten fuzz in an eroding plasma environment. Nuclear Fusion 51 (4), 043001.

Drazin, P. G., Reid, W. H., 2004. Introduction to Hydrodynamic Stability.

Dudarev, S. L., jul 2013. Density Functional Theory Models for Radiation Damage*. Annual Review of Materials Research 43 (1), 35–61.

Duderstadt, J., Hamilton, L., 1976. Nuclear Reactor Analysis.

Duffy, D. M., Rutherford, a. M., jan 2007. Including the effects of electronic stopping and electron–ion interactions in radiation damage simulations. Journal of Physics: Condensed Matter 19 (1), 016207.

Eckstein, W., 2005. Computer simulation of ion surface collisions with special emphasis to the work by Yamamura. In: Nuclear Instruments and Methods in Physics Research, Section B: Beam Interactions with Materials and Atoms. Vol. 232. pp. 108–116.

Eckstein, W., Biersack, J. P., 1985. Computer simulation of two-component target sputtering. Applied Physics A Solids and Surfaces 37 (2), 95–108.

Eckstein, W., Verbeek, H., Biersack, J. P., 1980. Computer simulation of the backscattering and implantation of hydrogen and helium. Journal of Applied Physics 51 (2), 1194–1200.

Ercolessi, F., Adams, J. B., 1994. Interatomic Potentials from First-Principles Calculations :. Europhysics Letters 26 (8), 583–588.

Evstatiev, E. G., Delzanno, G. L., Finn, J. M., 2006. A new method for analyzing line-tied kink modes in cylindrical geometry. Physics of Plasmas 13 (7).

Federici, G., Andrew, P., Barabaschi, P., 2003. Key ITER plasma edge and plasma–material interaction issues. ... of nuclear materials 316, 11–22.

Feynman, R. P., Leighton, R. B., Sands, M. L., 1963. The Feynman Lectures on Physics. Vol. 1.

Finn, J., Antonsen Jr., T., 1985. Magnetic helicity: What is it and what is it good for? Comments Plasma Phys. Control. Fusion 9, 111.

Fortuna-Zaleśna, E., Grzonka, J., Rubel, M., Garcia-Carrasco, A., Widdowson, A., Baron-Wiechec, A., Ciupiński, L., JET Contributors, 2017. Studies of dust from JET with the ITER-Like Wall: Composition and internal structure. Nuclear Materials and Energy 12, 582–587.

Gilbert, M. R., Dudarev, S. L., Nguyen-Manh, D., Zheng, S., Packer, L. W., Sublet, J.-C., nov 2013. Neutron-induced dpa, transmutations, gas production, and helium embrittlement of fusion materials. Journal of Nuclear Materials 442 (1-3), S755–S760.

Gilbert, M. R., Dudarev, S. L., Zheng, S., Packer, L. W., Sublet, J.-C., aug 2012. An integrated model for materials in a fusion power plant: transmutation, gas production, and helium embrittlement under neutron irradiation. Nuclear Fusion 52 (8), 083019.

Gilbert, M. R., Marian, J., Sublet, J. C., 2015. Energy spectra of primary knock-on atoms under neutron irradiation. Journal of Nuclear Materials 467, 121–134.
URL http://dx.doi.org/10.1016/j.jnucmat.2015.09.023

Gilbert, M. R., Sublet, J. C., 2016. PKA distributions: Contributions from transmutation products and from radioactive decay. Nuclear Materials and Energy 9, 576–580.

Gimblett, C. G., Hastie, R. J., Helander, P., 2006. The role of edge current-driven modes in ELM activity. Plasma Physics and Controlled Fusion 48 (10), 1531–1550.

Gold, T., Hoyle, F., feb 1960. On the Origin of Solar Flares. Monthly Notices of the Royal Astronomical Society 120 (2), 89–105.

Goorley, T., James, M., Booth, T., Brown, F., Bull, J., Cox, L. J., Durkee, J., Elson, J., Fensin, M., Forster, R. A., Hendricks, J., Hughes, H. G., Johns, R., Kiedrowski, B., Martz, R., Mashnik, S., McKinney, G., Pelowitz, D., Prael, R., Sweezy, J., Waters, L., Wilcox, T., Zukaitis, T., dec 2012. Initial MCNP6 Release Overview. Nuclear Technology 180 (3), 298–315.
URL https://www.tandfonline.com/doi/full/10.13182/NT11-135

Hammond, C., 2002. The Basics of Crystallography and Diffraction (2nd edn). Measurement Science and Technology 13 (2), 232–232.

Harder, N. D., Brezinsek, S., Pütterich, T., Fedorczak, N., Matthews, G. F., Meigs, A., Stamp, M. F., Sanden, M. C. M. V. D., Rooij, G. J. V., Contributors, J. E. T., 2016. ELM-resolved divertor erosion in the JET ITER-Like Wall. Nuclear Fusion 56 (2), 26014.

Harling, O. K., Thomas, M. T., Brodzinski, R. L., Rancitelli, L. A., 1975. Sputtering of Nb and Au by (d, t) Neutrons. Physical Review Letters 34 (21), 1–4.

Harling, O. K., Thomas, M. T., Brodzinski, R. L., Rancitelli, L. A., dec 1976. Recent neutron sputtering results and the status of neutron sputtering. Journal of Nuclear Materials 63, 422–428.

Hazeltine, R. D., Waelbroeck, F. L., 1998. The Framework of Plasma Physics. Perseus Books.

Hirth, J. P., Lothe, J., 1949. Theory of dislocations. Wiley-Interscience.

Hodgson, P. E., 1971. The nuclear optical model. Rep. Prog. Phys. 34, 765–819.

Hood, A. W., Browning, P. K., Linden, R. A. M. V. D., 2009. Coronal heating by magnetic reconnection in loops with zero net current. Astronomy & Astrophysics 506 (2), 913–925.

Hood, A. W., Cargill, P. J., Browning, P. K., Tam, K. V., 2016. An MHD avalanche in a multi-threaded coronal loop. The Astrophysical Journal 817 (1), 5.

Hood, A. W., Priest, E. R., 1979. Kink instability of solar coronal loops as the cause of solar flares. Solar Physics 64 (2), 303–321.

Hussain, A. S., Browning, P. K., Hood, A. W., jan 2017. A relaxation model of coronal heating in multiple interacting flux ropes. Astronomy & Astrophysics (29589), 1–13.

Inomoto, M., Watanabe, T. G., Gi, K., Yamasaki, K., Kamio, S., Imazawa, R., Yamada, T., Guo, X., Ushiki, T., Ishikawa, H., Nakamata, H., Kawakami, N., Sugawara, T., Matsuyama, K., Noma, K., Kuwahata, A., Tanabe, H., 2015. Centre-solenoid-free merging start-up of spherical tokamak plasmas in UTST. Nuclear Fusion 55 (3), 033013.

Inoue, S., Ono, Y., Horiuchi, R., Cheng, C., 2014. Numerical study of energy conversion mechanism of Magnetic Reconnection in the presence of High Guide field. Nuclear Fusion.

Jordan, D. W., Smith, P., 1999. Nonlinear ordinary differential equations : an introduction to dynamical systems.

Juslin, N., Wirth, B. D., jan 2013. Interatomic potentials for simulation of He bubble formation in W. Journal of Nuclear Materials 432 (1-3), 61–66.

Kajita, S., Sakaguchi, W., Ohno, N., Yoshida, N., Saeki, T., sep 2009. Formation

process of tungsten nanostructure by the exposure to helium plasma under fusion relevant plasma conditions. Nuclear Fusion 49 (9), 095005.

Keller, K., 1966. Recoil Gold Atoms from Fast-Neutron Bombardment. Journal of Applied Physics 37 (4), 1890.

Keller, K., jan 1968. Search for sputtered atoms by H 3 (d,n)He 4 neutrons that may contaminate a thermonuclear plasma. Plasma Physics 10 (2), 195–199.

Kelly, A., Knowles, K. M., 2012. Crystallography and Crystal Defects: Second Edition.

Khakshouri, S., Duffy, D., jul 2009. Influence of electronic effects on the surface erosion of tungsten. Physical Review B 80 (3), 035415.

Khorsandi, B., Blue, T., Windl, W., Kulisek, J., Dean, S., 2006. TRIM Modeling of Displacement Damage in SiC for Monoenergetic Neutrons. Journal of ASTM International 3 (8), 100358.

Kikuchi, M., 2010. A Review of Fusion and Tokamak Research Towards Steady-State Operation: A JAEA Contribution.

Kikuchi, M., 2011. Frontiers in fusion research.

Kinchin, G. H., Pease, R. S., 1955. Displacement of Atoms in Solid by Radiation. Rep. Prog. Physics 18.

Kittel, C., 2010. Introduction to Solid State Physics.

Klimchuk, J. A., apr 2015. Key aspects of coronal heating. Philosophical Transactions of the Royal Society A: Mathematical, Physical and Engineering Sciences 373 (2042), 20140256.

Kondrashov, D., Feynman, J., Liewer, P. C., Ruzmaikin, A., jul 1999. Three-dimensional magnetohydrodynamic simulations of the interaction of magnetic flux tubes. The Astrophysical Journal 10 (1997), 884–898.

Kotomin, E., Kuzovkov, V., dec 1992. Phenomenological kinetics of Frenkel defect recombination and accumulation in ionic solids. Reports on Progress in Physics 55 (12), 2079–2188.

Kotomin, E., Zaiser, M., aug 1993. A mesoscopic approach to point-defect clustering in solids during irradiation. Applied Physics A Solids and Surfaces 57 (2), 117–121.

Kotomin, E., Zaiser, M., Soppe, W., aug 1994. A mesoscopic approach to radiation-induced defect aggregation in alkali halides stimulated by the elastic interaction of mobile Frenkel defects. Philosophical Magazine A 70 (2), 313–327.

Kwast, H., Werle, H., Wu, C. H., 1996. Tritium retention in neutron-irradiated carbon-based materials and beryllium. Physica Scripta 41.

Lewis, E., Miller Jr., W., 1993. Computational Methods of Neutron Transport.

Lewis, E. E., 2010. Second-order neutron transport methods. In: Nuclear Computational Science: A Century in Review. pp. 85–115.

Liu, J.-Y., Liu, B.-F. F., sep 2009. Investigating the disk-corona relation in a blue AGN sample. Research in Astronomy and Astrophysics 9 (9), 966–978.

Liu, Y., Kurokawa, H., Liu, C., Brooks, D. H., Dun, J., Ishii, T. T., Zhang, H., 2007. The X10 flare on 29 October 2003: Was it triggered by magnetic reconnection between counter-helical fluxes? Solar Physics 240 (2), 253–262.

Longcope, D. W., Tarr, L. A., apr 2015. Relating magnetic reconnection to coronal heating. Philosophical Transactions of the Royal Society A: Mathematical, Physical and Engineering Sciences 373 (2042), 20140263–20140263.

Lu, T. E., Hamilton, J. R., 1991. Avalanches and the Distribution of Solar Flares. Astrophysical Journal 380, L89–L92.

Maggi, C., Delabie, E., Biewer, T., Groth, M., Hawkes, N., Lehnen, M., de la Luna, E., McCormick, K., Reux, C., Rimini, F., Solano, E., Andrew, Y., Bourdelle, C., Bobkov, V., Brix, M., Calabro, G., Czarnecka, A., Flanagan, J., Lerche, E., Marsen, S., Nunes, I., Van Eester, D., Stamp, M., 2014. L–H power threshold studies in JET with Be/W and C wall. Nuclear Fusion 54 (2), 023007.

Maisonnier, D., Cook, I., Sardain, P., Andreani, R., Di Pace, L., Forrest, R., Giancarli, L., Hermsmeyer, S., Norajitra, P., Taylor, N., Ward, D., 2005. A conceptual study of commercial fusion power plants 1 (05).

Markelj, S., Ogorodnikova, O. V., Pelicon, P., Schwarz-Selinger, T., Čadež, I., 2013a. Temperature dependence of D atom adsorption on polycrystalline tungsten. Vol. 282.

Markelj, S., Ogorodnikova, O. V., Pelicon, P., Schwarz-Selinger, T., Sugiyama, K., Cadez, I., 2013b. Study of thermal hydrogen atom interaction with undamaged and self-damaged tungsten. Journal of Nuclear Materials 438 (SUPPL), 1027–1031.

Markelj, S., Ogorodnikova, O. V., Pelicon, P., Schwarz Selinger, T., Vavpetič, P., Čadež, I., 2014. In situ nuclear reaction analysis of D retention in undamaged and self-damaged tungsten under atomic D exposure. Physica Scripta T159, 014047.

Matsuura, H., Nakao, Y., 2009. Modification of alpha-particle emission spectrum in beam-injected deuterium-tritium plasmas. Physics of Plasmas 16 (4), 042507.

Melrose, D. B., nov 1991. Neutralized and unneutralized current patterns in the solar corona. The Astrophysical Journal 381, 306.

Melrose, D. B., sep 1997. A Solar Flare Model Based on Magnetic Reconnection between Current Carrying Loops. The Astrophysical Journal 486 (1), 521–533.

Nordlund, K., Runeberg, N., Sundholm, D., oct 1997. Repulsive interatomic potentials calculated using Hartree-Fock and density-functional theory methods. Nuclear Instruments and Methods in Physics Research Section B: Beam Interactions with Materials and Atoms 132 (1), 45–54.

Ono, Y., Tanabe, H., Hayashi, Y., Ii, T., Narushima, Y., Yamada, T., Inomoto, M., Cheng, C. Z., 2011. Ion and electron heating characteristics of magnetic reconnection in a two flux loop merging experiment. Physical Review Letters 107 (18).

Owen, J. M., Shashkov, M., 2014. Arbitrary Lagrangian Eulerian remap treatments consistent with staggered compatible total energy conserving Lagrangian methods. Journal of Computational Physics 273, 520–547.

Parker, E. N., 1957. Sweet's mechanism for merging magnetic fields in conducting fluids. Journal of Geophysical Research 62 (4), 509.

Parnell, C. E., De Moortel, I., Haugh, N., Parnell, C. E., De Moortel, I., jul 2012. A contemporary view of coronal heating. Philosophical Transactions of the Royal Society A: Mathematical, Physical and Engineering Sciences 370 (1970), 3217–3240.

Plimpton, S., 1995. Fast Parallel Algorithms for Short – Range Molecular Dynamics. Journal of Computational Physics 117 (June 1994), 1–19.

Pontin, D., Wilmot-Smith, A., Hornig, G., Galsgaard, K., 2010. Dynamics of braided coronal loops II: cascade to multiple small-scale reconnection events 57, 1–6.

Post, D., Abdallah, J., Clark, R. E. H., Putvinskaya, N., 2004. Calculations of energy losses due to atomic processes in tokamaks with applications to the International

Thermonuclear Experimental Reactor divertor Calculations of energy losses due to atomic processes in tokamaks with applications to the International T 2328 (1995).

Priest, E., 2014. Magnetohydrodynamics of the Sun.

Priest, E., Forbes, T., 2000. Magnetic Reconnection.

Priest, E. R., Cowley, S. W. H., 1975. Some comments on magnetic field reconnection. Journal of Plasma Physics 14 (02), 271.

Race, C. P., Mason, D. R., Finnis, M. W., Foulkes, W. M. C., Horsfield, A. P., Sutton, A. P., nov 2010a. The treatment of electronic excitations in atomistic models of radiation damage in metals. Reports on Progress in Physics 73 (11), 116501.

Race, C. P., Mason, D. R., Foo, M. H. F., Foulkes, W. M. C., Horsfield, A. P., Sutton, A. P., mar 2013. Quantum-classical simulations of the electronic stopping force and charge on slow heavy channelling ions in metals. Journal of physics. Condensed matter : an Institute of Physics journal 25 (12), 125501.

Race, C. P., Mason, D. R., Sutton, A. P., sep 2010b. An improved model of interatomic forces for large simulations of metals containing excited electrons. New Journal of Physics 12 (9), 93049.

Reilly, D., Ensslin, N., Jr, H. S., Kreiner, S., 1991. Passive nondestructive assay of nuclear materials.

Roth, J., Schmid, K., 2011. Hydrogen in tungsten as plasma-facing material. Physica Scripta 2011 (T145), 14031.

Roth, J., Tsitrone, E., Loarte, A., Loarer, T., Counsell, G., Neu, R., Philipps, V., Brezinsek, S., Lehnen, M., Coad, P., Grisolia, C., Schmid, K., Krieger, K., Kallenbach, A., Lipschultz, B., Doerner, R., Causey, R., Alimov, V., Shu, W.,

Ogorodnikova, O., Kirschner, A., Federici, G., Kukushkin, A., jun 2009. Recent analysis of key plasma wall interactions issues for ITER. Journal of Nuclear Materials 390-391, 1–9.

Schnack, D., 2009. Lectures in Magnetohydrodynamics: With an Appendix on Extended MHD.

Schneider, R., Bonnin, X., Borrass, K., Coster, D. P., Kastelewicz, H., Reiter, D., Rozhansky, V. a., Braams, B. J., feb 2006. Plasma Edge Physics with B2-Eirene. Contributions to Plasma Physics 46 (1-2), 3–191.

Schwabl, F., 1992. Quantum Mechanics.

Setyawan, W., Nandipati, G., Roche, K. J., Heinisch, H. L., Wirth, B. D., Kurtz, R. J., 2015. Displacement cascades and defects annealing in tungsten, Part I: Defect database from molecular dynamics simulations. Journal of Nuclear Materials 462, 329–337.

Sigmund, P., 1987. Mechanisms and theory of physical sputtering by particle impact. Nuclear Instruments and Methods in Physics Research ... (5).

Sigmund, P., Schinner, A., oct 2002. Binary theory of electronic stopping. Nuclear Instruments and Methods in Physics Research Section B: Beam Interactions with Materials and Atoms 195 (1-2), 64–90.

Srivastava, A. K., Dwivedi, B. N., may 2010. Observations from Hinode/EIS of intensity oscillations above a bright point: signature of the leakage of acoustic oscillations in the inner corona. Monthly Notices of the Royal Astronomical Society 405 (4), 2317–2326.

Srivastava, M. S., 2010. Methods of Multivariate Statistics.

Stangeby, P. C., 2000. The Plasma Boundary of Magnetic Fusion Devices. IOP.

Stanier, A., Browning, P., Gordovskyy, M., 2012. Two-fluid simulations of merging-compression start-up in the Mega-Ampere Spherical Tokamak (June).

Stanier, A., Browning, P., Gordovskyy, M., McClements, K. G., Gryaznevich, M. P., Lukin, V. S., 2013. Two-fluid simulations of driven reconnection in the mega-ampere spherical tokamak. Physics of Plasmas 20 (12), 122302.

Stanier, A., Simakov, A. N., Chacón, L., Daughton, W., 2015. Fast magnetic reconnection with large guide fields Fast magnetic reconnection with large guide fields 010701.

Stoller, R., Greenwood, L., 2001. A comparison of the NRT displacement model and primary damage formation observed in molecular dynamics cascade simulations. ASTM Special Technical Publication (1398).

Stoller, R. E., Toloczko, M. B., Was, G. S., Certain, A. G., Dwaraknath, S., Garner, F. A., 2013. On the use of SRIM for computing radiation damage exposure. Nuclear Instruments and Methods in Physics Research, Section B: Beam Interactions with Materials and Atoms 310, 75–80.

Stukowski, A., 2012. Structure identification methods for atomistic simulations of crystalline materials. ... Simulation in Materials Science and Engineering 20 (2012).

Stukowski, A., Bulatov, V. V., Arsenlis, A., dec 2012. Automated identification and indexing of dislocations in crystal interfaces. Modelling and Simulation in Materials Science and Engineering 20 (8), 85007.

Sublet, J. C., Eastwood, J. W., Morgan, J. G., Gilbert, M. R., Fleming, M., Arter, W., 2017. FISPACT-II: An Advanced Simulation System for Activation, Transmutation and Material Modelling. Nuclear Data Sheets 139, 77–137.

Tam, K. V., Hood, A. W., Browning, P. K., Cargill, P. J., aug 2015. Coronal heating in multiple magnetic threads. Astronomy & Astrophysics 580, A122.

Taylor, J. B., 1974. Relaxation of toroidal plasma and generation of reverse magnetic fields. Physical Review Letters 33 (19), 1139–1141.

Taylor, J. B., 1986. Relaxation and magnetic reconnection in plasmas. Reviews of Modern Physics 58 (3), 741–763.

Tyburska, B., Alimov, V., Ogorodnikova, O. V., Schmid, K., Ertl, K., dec 2009. Deuterium retention in self-damaged tungsten. Journal of Nuclear Materials 395 (1-3), 150–155.

Wang, H., Cao, W., Liu, C., Xu, Y., Liu, R., Zeng, Z., Chae, J., Ji, H., 2015. Witnessing magnetic twist with high-resolution observation from the 1.6-m New Solar Telescope. Nature Communications 6, 7008.

Was, G. S., 2007. Fundamentals of radiation materials science.

Watanabe, H., Yoshida, N., Kurishita, H., Muroga, T., 2011. Synergistic Effects of Neutron (ion) and Plasma on Material in QUEST 1, 2011.

Wesson, J., 1987. Tokamaks. Clarendon Press, Oxford.

Wirth, B. D., Nordlund, K., Whyte, D. G., Xu, D., mar 2011. Fusion materials modeling: Challenges and opportunities. MRS Bulletin 36 (03), 216–222.

Yamada, M., Kulsrud, R., Ji, H., 2010. Magnetic reconnection. Reviews of Modern Physics 82 (1), 603–664.

Ye, B., Kasugai, Y., Ikeda, Y., Fan, Y., Zhou, X., Du, J., Han, R., 2000. The sputtering of radioactive recoil nuclides induced by fast neutron. Journal of Applied Physics 87 (5), 2581.

Yushmanov, P. N., Takizuka, T., 1990. Scalings for tokamak energy confinement. Nuclear ... 1999.

Zarkadoula, E., Daraszewicz, S. L., Duffy, D. M., Seaton, M. A., Todorov, I. T., Nordlund, K., Dove, M. T., Trachenko, K., feb 2014a. Electronic effects in high-energy radiation damage in iron. Journal of physics. Condensed matter : an Institute of Physics journal 26 (8), 85401.

Zarkadoula, E., Duffy, D. M., Nordlund, K., Seaton, M. a., Todorov, I. T., Weber, W. J., Trachenko, K., nov 2014b. Electronic effects in high-energy radiation damage in tungsten, 7.

Ziegler, J. F., 1999. Stopping of energetic light ions in elemental matter. Journal of applied physics 1272, 1249–1272.

Ziegler, J. F., Ziegler, M. D., Biersack, J. P., 2010. SRIM - The stopping and range of ions in matter (2010). Nuclear Instruments and Methods in Physics Research, Section B: Beam Interactions with Materials and Atoms 268, 1818–1823.

Zweibel, E. G., Yamada, M., 2009. Magnetic Reconnection in Astrophysical and Laboratory Plasmas. Annual Review of Astronomy and Astrophysics 47 (1), 291–332.

Appendix A: All Cascade Visualisations of Primary Neutron Events Using Molecular Dynamics

The following are all the skewed normal curves used to visualise the cascades formed. The overlays (the vectors that are presented with each graph) are the eigenvectors of the covariance analysis. Details can be seen in Table 5.3.

3 keV	10 keV	100 keV
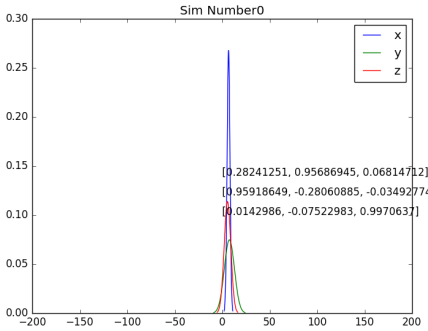	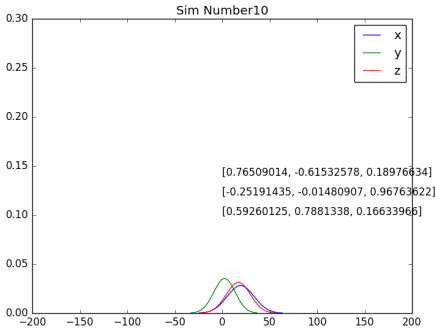	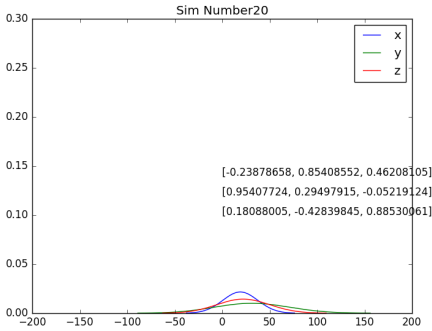
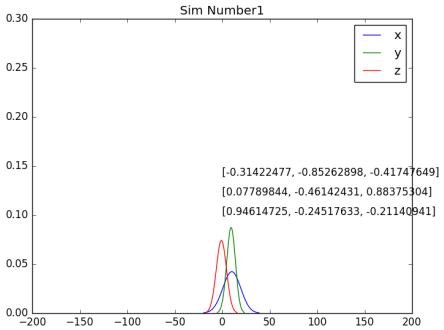	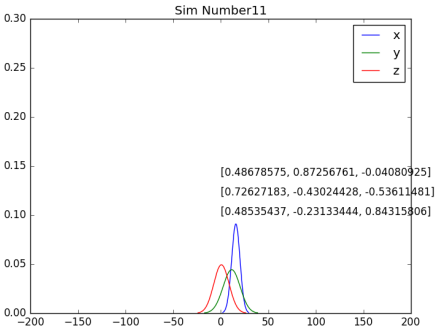	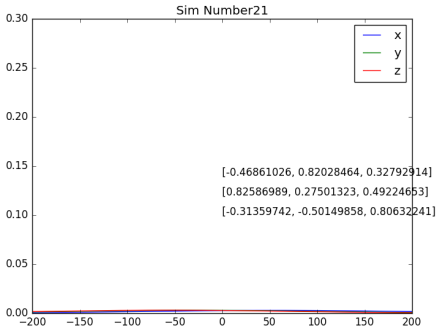

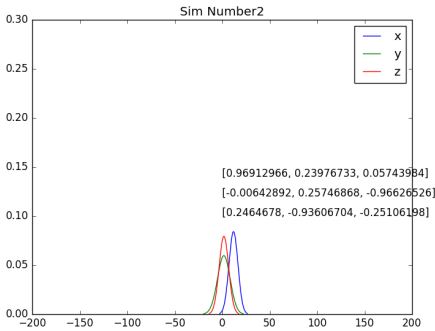
Sim Number2
x
y
z
[0.96912966, 0.23976733, 0.05743984]
[-0.00642892, 0.25746868, -0.96626526]
[0.2464678, -0.93606704, -0.25106198]

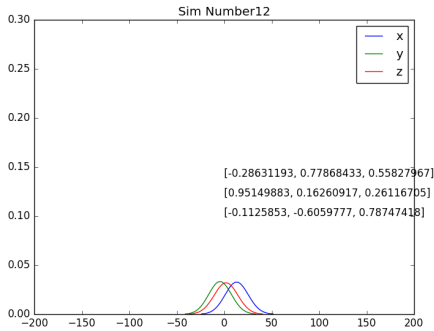
Sim Number12
x
y
z
[-0.28631193, 0.77868433, 0.55827967]
[0.95149883, 0.16260917, 0.26116705]
[-0.1125853, -0.6059777, 0.78747418]

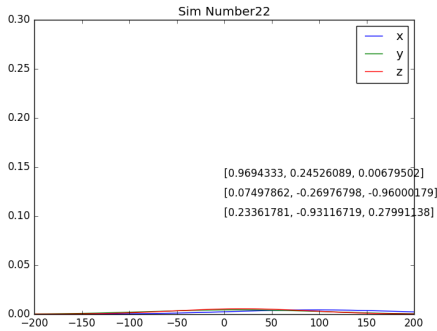
Sim Number22
x
y
z
[0.9694333, 0.24526089, 0.00679502]
[0.07497862, -0.26976798, -0.96000179]
[0.23361781, -0.93116719, 0.27991138]

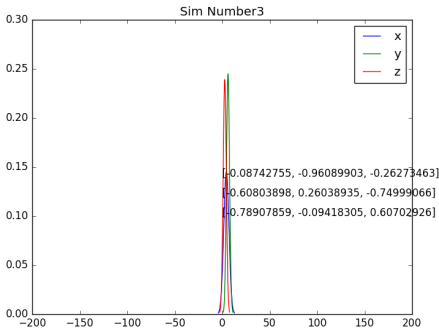
Sim Number3
x
y
z
[-0.08742755, -0.96089903, -0.26273463]
[0.60803898, 0.26038935, -0.74999066]
[0.78907859, -0.09418305, 0.60702926]

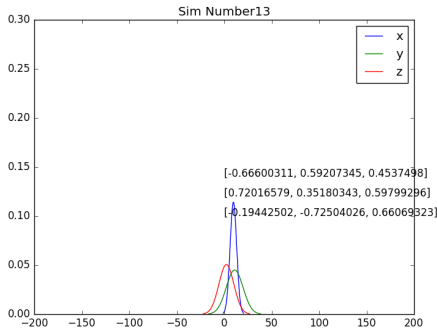
Sim Number13
x
y
z
[-0.66600311, 0.59207345, 0.4537498]
[0.72016579, 0.35180343, 0.59799296]
[-0.19442502, -0.72504026, 0.66069323]

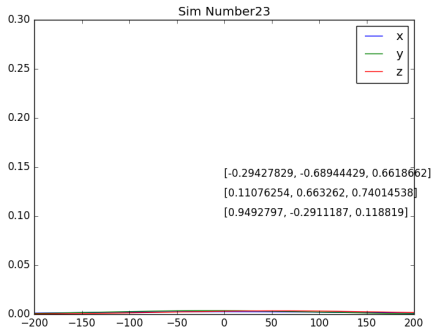
Sim Number23
x
y
z
[-0.29427829, -0.68944429, 0.6618662]
[0.11076254, 0.663262, 0.74014538]
[0.9492797, -0.2911187, 0.118819]

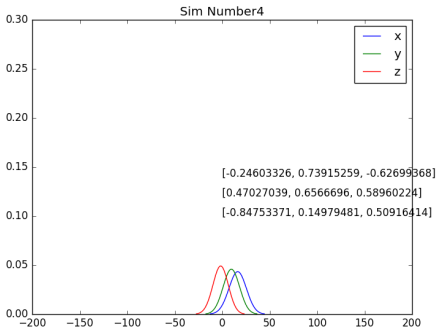
Sim Number4
x
y
z
[-0.24603326, 0.73915259, -0.62699368]
[0.47027039, 0.6566696, 0.58960224]
[-0.84753371, 0.14979481, 0.50916414]

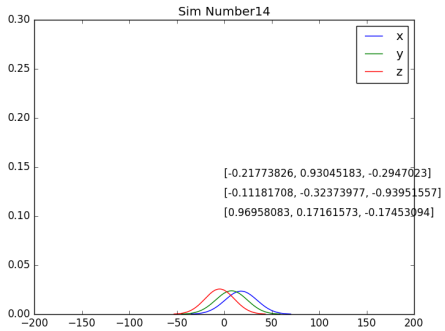
Sim Number14
x
y
z
[-0.21773826, 0.93045183, -0.2947023]
[-0.11181708, -0.32373977, -0.93951557]
[0.96958083, 0.17161573, -0.17453094]

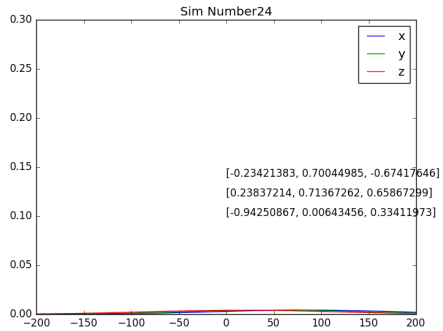
Sim Number24
x
y
z
[-0.23421383, 0.70044985, -0.67417646]
[0.23837214, 0.71367262, 0.65867299]
[-0.94250867, 0.00643456, 0.33411973]

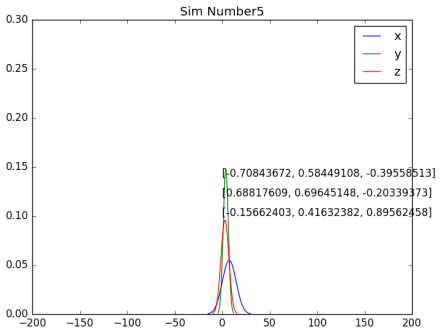
Sim Number5
x
y
z
[-0.70843672, 0.58449108, -0.39558513]
[0.68817609, 0.69645148, -0.20339373]
[-0.15662403, 0.41632382, 0.89562458]

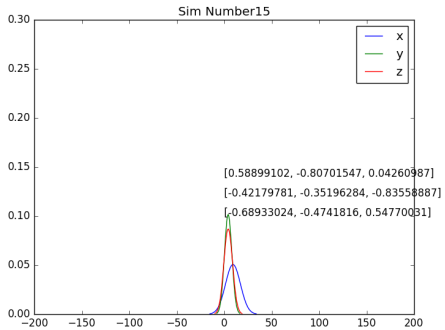
Sim Number15
x
y
z
[0.58899102, -0.80701547, 0.04260987]
[-0.42179781, -0.35196284, -0.83558887]
[-0.68933024, -0.4741816, 0.54770031]

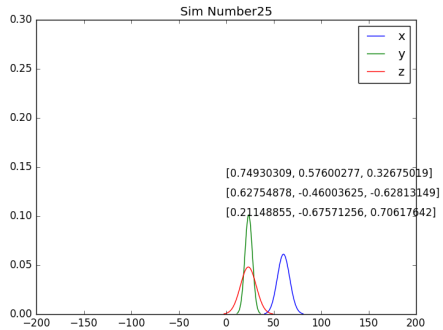
Sim Number25
x
y
z
[0.74930309, 0.57600277, 0.32675019]
[0.62754878, -0.46003625, -0.62813149]
[0.21148855, -0.67571256, 0.70617642]

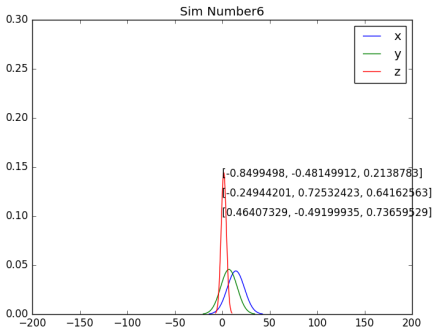
Sim Number6
x
y
z
[-0.8499498, -0.48149912, 0.2138783]
[-0.24944201, 0.72532423, 0.64162563]
[0.46407329, -0.49199935, 0.73659529]

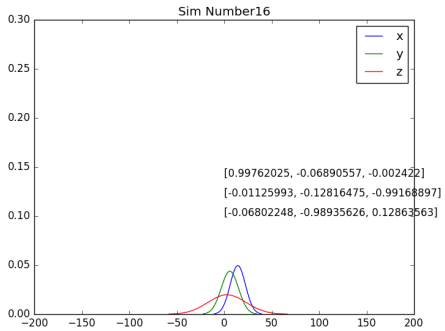
Sim Number16
x
y
z
[0.99762025, -0.06890557, -0.002422]
[-0.01125993, -0.12816475, -0.99168897]
[-0.06802248, -0.98935626, 0.12863563]

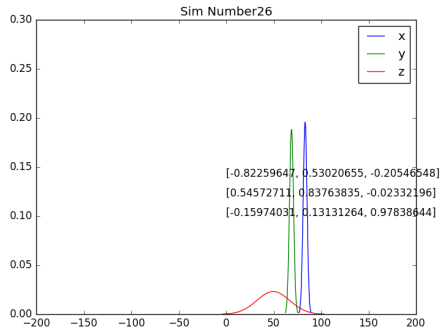
Sim Number26
x
y
z
[-0.82259647, 0.53020655, -0.20546548]
[0.54572711, 0.83763835, -0.02332196]
[-0.15974031, 0.13131264, 0.97838644]

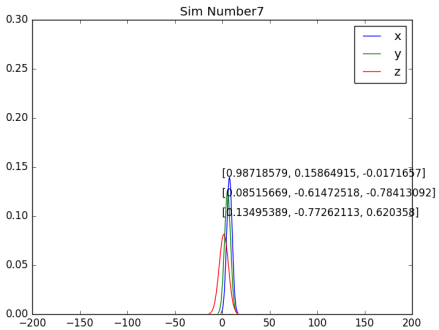
Sim Number7
x
y
z
[0.98718579, 0.15864915, -0.0171657]
[0.08515669, -0.61472518, -0.78413092]
[0.13495389, -0.77262113, 0.620358]

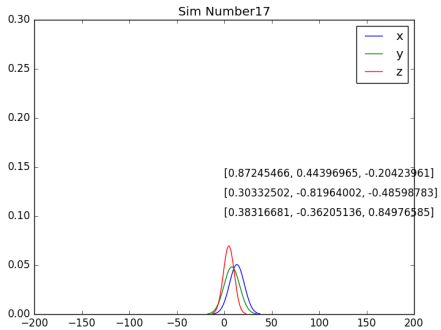
Sim Number17
x
y
z
[0.87245466, 0.44396965, -0.20423961]
[0.30332502, -0.81964002, -0.48598783]
[0.38316681, -0.36205136, 0.84976585]

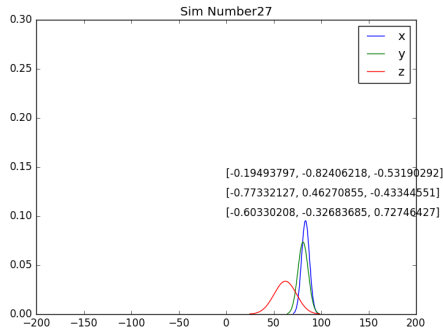
Sim Number27
x
y
z
[-0.19493797, -0.82406218, -0.53190292]
[-0.77332127, 0.46270855, -0.43344551]
[-0.60330208, -0.32683685, 0.72746427]

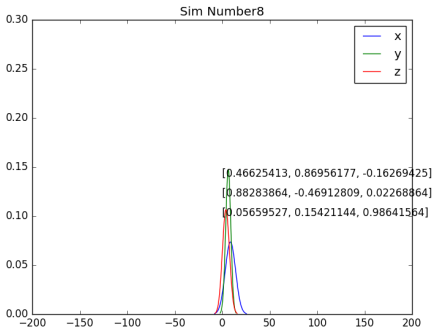
Sim Number8
x
y
z
[0.46625413, 0.86956177, -0.16269425]
[0.88283864, -0.46912809, 0.02268864]
[0.05659527, 0.15421144, 0.98641554]

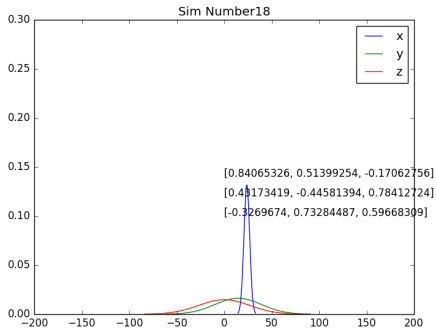
Sim Number18
x
y
z
[0.84065326, 0.51399254, -0.17062756]
[0.43173419, -0.44581394, 0.78412724]
[-0.3269674, 0.73284487, 0.59668309]

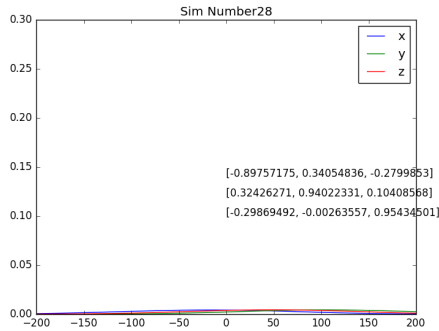
Sim Number28
x
y
z
[-0.89757175, 0.34054836, -0.2799853]
[0.32426271, 0.94022331, 0.10408568]
[-0.29869492, -0.00263557, 0.95434501]

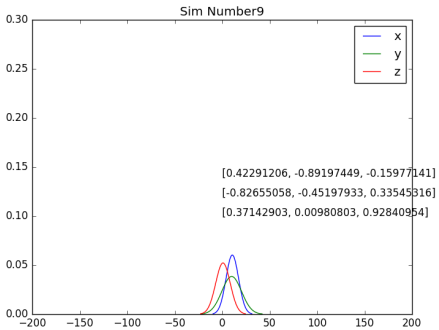
Sim Number9
x
y
z
[0.42291206, -0.89197449, -0.15977141]
[-0.82655058, -0.45197933, 0.33545316]
[0.37142903, 0.00980803, 0.92840954]

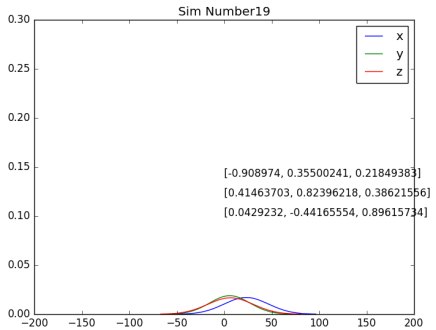
Sim Number19
x
y
z
[-0.908974, 0.35500241, 0.21849383]
[0.41463703, 0.82396218, 0.38621556]
[0.0429232, -0.44165554, 0.89615734]

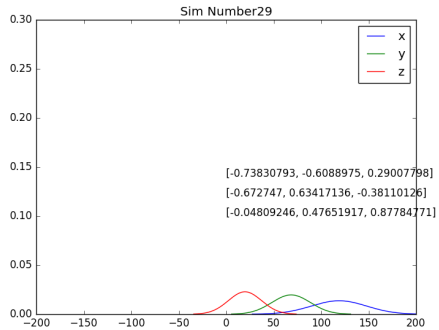
Sim Number29
x
y
z
[-0.73830793, -0.6088975, 0.29007798]
[-0.672747, 0.63417136, -0.38110126]
[-0.04809246, 0.47651917, 0.87784771]